



UNIVERSITÀ DEGLI STUDI DI MILANO

FACOLTÀ DI SCIENZE E TECNOLOGIE

Corso di Laurea Triennale in Fisica

TESI DI LAUREA TRIENNALE

**Background from electrons faking photons searching
for Dark Matter in the mono-photon channel with the
ATLAS detector.**

Codice PACS: 14.80.-j

Relatore interno:

Prof. Leonardo Carminati

Correlatori:

Dott. Stefano Manzoni

Dott.ssa Silvia Resconi

Tesi di Laurea di:

Elena Mazzeo

Matricola: 868231

Anno Accademico: 2017/2018

Contents

Introduction	i
1 The quest for Dark Matter	1
1.1 Evidences of the existence of Dark Matter	2
1.1.1 The rotation curves of galaxies	2
1.1.2 Gravitational lensing	3
1.1.3 The Cosmic Microwave Background	3
1.2 Dark Matter candidates	4
1.3 Detection strategies	7
1.3.1 Direct searches	7
1.3.2 Indirect searches	8
1.3.3 Search at colliders	8
2 The Large Hadron Collider and the ATLAS experiment	11
2.1 The LHC	11
2.1.1 Proton-proton interactions and the LHC structure	11
2.1.2 The accelerator complex	13
2.2 The ATLAS experiment	14
2.2.1 The Inner Detector	15
2.2.2 The calorimeters	17
2.2.3 The Muon Spectrometer	19
2.2.4 The trigger system	20
3 Reconstruction of electrons and photons with the ATLAS detector	21
3.1 Electrons	22
3.1.1 Reconstruction	22
3.1.2 Identification	24
3.1.3 Isolation	24
3.2 Photons	25
3.2.1 Reconstruction	25
3.2.2 Identification	29
3.2.3 Isolation	29
4 The Mono-Photon analysis	31
4.1 Event selection	31
4.1.1 Pre-selection of events	31
4.1.2 Selection of physics objects	32
4.1.3 Event selection in the Signal Region	32
4.2 Background estimation	33
4.2.1 Definition of Control Regions	34
4.2.2 The simultaneous fit technique	34
4.2.3 Fake- γ background estimation	36
4.3 Results	37
4.4 Search for new physics	38

5	Background from electron faking photons for the Mono-Photon analysis	41
5.1	The electron-to-photon fake rate	41
5.1.1	Event selection	42
5.1.2	Fake-rate estimation	42
5.1.3	Background subtraction	45
5.1.4	Systematic uncertainties	46
5.1.5	Results	47
5.2	Background from electrons faking photons	57
6	Conclusions	61

Introduction

The existence of Dark Matter is strongly supported by countless astrophysical and cosmological observations, agreeing on the fact that ordinary matter (i.e. *Standard Model* particles) cannot account for the total mass and energy in our Universe.

Despite the existence of Dark Matter seems well established, the nature of Dark Matter is still unknown. A long-held hypothesis is that Dark Matter is made up of WIMPs (*Weakly Interacting Massive Particles*): neutral stable particles with masses lying between 10 GeV and 1 TeV and weakly interacting with Standard Model particles belong to the WIMP family. The WIMP paradigm has been, for decades, the most credited hypothesis on the nature of Dark Matter. The main reason for this is that a weakly interacting stable particle whose mass belongs to the range 10 GeV - 1 TeV would account exactly for the amount of relic density of Dark Matter in the Universe measured by cosmological experiments. This argument is known as the *WIMP miracle*.

A tremendous effort has been placed in the hunt for Dark Matter, especially WIMPs: searches at colliders have a crucial role in the quest for Dark Matter candidates, because a WIMP can, in principle, be produced from a pp collision. Dedicated searches for Dark Matter are performed with the ATLAS experiment at the Large Hadron Collider. Being a WIMP electrically neutral and weakly interacting with Standard Model particles, it would not leave any detectable trace in the ATLAS detectors. However, a WIMP's presence can be inferred from a momentum imbalance in the transverse plane: the total transverse momentum is expected to be zero, therefore, if an undetectable particle (e.g. a WIMP) is produced in a pp collision, a missing transverse momentum E_T^{miss} would be measured by the ATLAS detector.

A possible approach to Dark Matter searches with the ATLAS detector is to look for a particular experimental signature, i.e. a large E_T^{miss} recoiling against a detectable Standard Model particle. The latter gives the name to such searches, called *mono-X searches*, where X is the Standard Model particle used to tag the event. The Mono-Photon analysis fits in the mono-X framework, searching for events where the final state carries a mono-photon signature. The $E_T^{miss} + \gamma$ final state is relatively clean: only a few Standard Model processes mimick such signature in their final state. The evaluation of the background yields for the Mono-Photon analysis follows two different paths, whether the considered background source belongs to real- γ backgrounds or fake- γ backgrounds. As their name hints, events forming real- γ backgrounds have true photons in their final state, while fake- γ background sources are characterized by another physics object being mistakenly reconstructed as a photon. The estimation of real- γ background yield is based on the definition of Control Regions (CRs), orthogonal to the Signal Region (SR) of the analysis (where a real $DM + \gamma$ signature is expected), built in a way that they are dominated by a single background process. Background yields from real- γ sources predicted by Monte-Carlo (MC) simulations are rescaled with a data-to-simulation ratio determined primarily in CRs. The two fake- γ background sources affecting the Mono-Photon analysis are from electrons faking photons and jets faking photons: the former is the second major source of systematic uncertainty on the total background of the SR, with a relative contribution of 1.5%. The work presented in this thesis was aimed at providing a new estimation of the background from electrons faking photons. The estimation of fake- γ background yields cannot rely on MC predictions: the number of other physics objects faking photons is primarily due to detector imperfections or malfunctions that can't be accurately reproduced by MC simulations. Therefore, a purely in-situ technique is to be employed.

Although the reconstruction algorithm for electrons and photons is specifically designed to minimize ambiguities and to avoid misreconstruction of electrons as photons (and vice-versa), a small fraction of electrons mistakenly reconstructed (and identified) as photons contaminates the

sample of mono-photon events probed by the Mono-Photon analysis. To estimate the number of such electron fakes, a two-step approach is employed. The first step is to measure the probability of electrons to be mistakenly reconstructed (and identified) as photons, known as the *electron-to-photon fake rate*. The electron-to-photon fake rate is determined from a pure sample of $Z \rightarrow ee$ events, where the di-electron in the final state can be reconstructed either as ee or as $e\gamma$. In the latter case, the photon is of course a fake photon. The ratio of reconstructed $e\gamma$ yields to reconstructed ee yields provides an estimation of the electron-to-photon fake rate. The number of true ee and $e\gamma$ events is estimated performing a background subtraction on the Z boson mass spectra. The fake rate is both as a function of the pseudorapidity η and as a function of $|\eta|$ and p_T .

As the second step, the electron-to-photon fake rate was used to compute the number of electron fakes for every region of the Mono-Photon analysis. For each region of the analysis an additional CR, the probe-electron CR, is defined: the probe- e CR is defined the same way as the corresponding CR of the analysis, except that the requirements on the photon are replaced with a request to have an electron. The yield of electron fakes in each region of the analysis is the event yield in the corresponding probe- e CR rescaled with the electron-to-photon fake rate.

This thesis is organized as follows. The first Chapter provides an overview of the decades-long quest for Dark Matter, including an introduction on the possible searches at colliders. In the second Chapter, the Large Hadron Collider and the ATLAS experiment are described. The reconstruction algorithm responsible for the parallel reconstruction of electrons and photons with the ATLAS detector is the focus of the third Chapter; a brief introduction on identification and isolation of electrons and photons is also present. The fourth Chapter presents the Mono-Photon analysis. The fifth Chapter includes a description of the methodology employed to measure the electron-to-photon fake rate and presents the electrons faking photons background yield for the Mono-Photon analysis obtained with the above-mentioned measurement. The conclusions are summarized in the sixth and final Chapter.

CHAPTER 1

The quest for Dark Matter

The current understanding of our Universe is based on the Standard Model (SM) of particle physics. The SM, summarized in Fig. 1.1, describes three of the four known fundamental forces (the electromagnetic, weak, and strong interactions, while it does not include the gravitational force) as well as classifies all known elementary particles.

According to the SM, the fundamental constituents of matter are *fermions*, i.e. $\frac{1}{2}$ -spin particles, among which one can distinguish *leptons* and *quarks*. The left-handed components of both leptons and quarks are grouped in three $SU(2)^1$ doublets, while the right handed components are singlets. Every fermion has its own antiparticle, i.e. a particle with the same mass but opposite quantum numbers². The interactions between these elementary particles are mediated by integer-spin particles called *gauge bosons*: strong interactions are mediated by *gluons* (g), while *photons* (γ) are the carriers of the electromagnetic force; weak interactions are mediated by the bosons W^+ , W^- , Z . The last particle described by the SM is the *Higgs boson* H , which was introduced to explain the mass of the massive gauge bosons and other elementary particles.

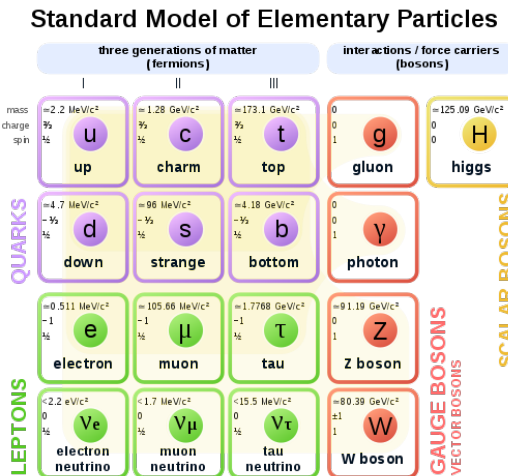


Figure 1.1: Particles included in the Standard Model of particle physics.

The SM of particle physics is able to interpret and explain decades of experimental findings, and the observation of the Higgs boson in 2012 at LHC provided the last building brick of the SM framework.

Despite no discrepancies between the experimental results and the SM predictions have been observed so far, the SM is not able to explain the complete picture. The theory incorporates only three out of the four fundamental forces, omitting gravity, and, on top of this, some experimental findings in particle physics have come to challenge the SM theory, e.g. neutrino oscillations. However, the most prominent downside of the SM is that an explanation and a description of Dark Matter is not incorporated in the theory. It can be inferred from cosmological observations that ordinary (fermionic) matter only makes up less than 5% of the total energy of the Universe, while 27% and 68% are attributed respectively to Dark Matter and Dark Energy (see Section 1.1.3).

¹The $SU(2)$ symmetry group forms, together with $SU(3)$ and $U(1)$, the internal symmetry group of the SM.

²It's useful to point out that a particle can be its own antiparticle.

It is thus natural to wonder if the SM can be considered as the low-energy counterpart of a more fundamental theory, extending the SM to hopefully include a description of gravity and of the nature of Dark Matter.

Dark Matter searches are of crucial importance to test the extensions of the SM contemplating particles which could constitute viable Dark Matter candidates, and to understand the nature of Dark Matter itself.

This chapter will begin with an overview of some compelling evidences for the existence of Dark Matter, which will be followed by a presentation of viable Dark Matter candidates which are relevant to this thesis, i.e. WIMPs (*Weakly Interacting Massive Particles*). The end of the chapter will be dedicated to discussing the possible direct and indirect searches of Dark Matter, plus the possible searches at experiments at colliders.

1.1 Evidences of the existence of Dark Matter

Most of the evidences of the existence of Dark Matter come from astrophysical observations at galactic and cosmic scales. Three of the most widely known evidences are here presented and discussed.

1.1.1 The rotation curves of galaxies

The *rotation curves* of galaxies - i.e. the circular velocity profile of the stars and gas in a galaxy, as a function of their distance from the galactic center, $v(R)$ - provided the first and most convincing evidence of the existence of Dark Matter. It is possible in fact to infer the mass distribution of galaxies from their rotation curves.

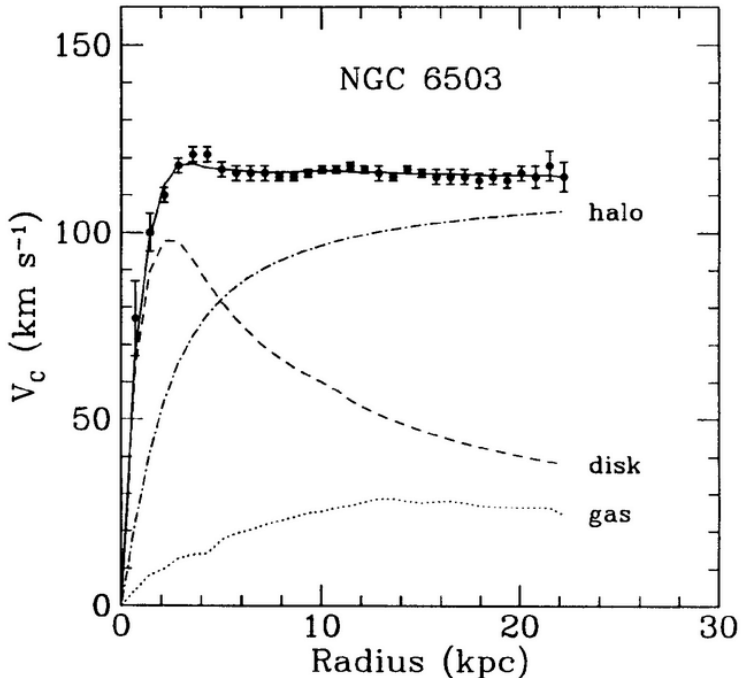


Figure 1.2: Rotation curve of galaxy NGC 6503. One can notice the discrepancy between the experimental curve and the expected curve from the visible disk (dashed line). The contribution of the hidden halo is also highlighted here.

The Newtonian dynamics predicts a decrease of circular velocity with the increase of the distance R from the center of galaxies following the power law $v \sim 1/\sqrt{R}$, known as *Keplerian decrease*.

The observation of a "flat" behaviour of the velocity up to distances comparable with three times the galaxies' optical radius is in disagreement with the above-mentioned theoretical expectation provided by Newtonian dynamics. This discrepancy between theory and observations was explained by assuming that a hidden halo (the Dark Matter halo) was present in the outer region of galaxies; the presence of a hidden mass - the mass of the halo - can explain the observed flat rotation curves, as it is clearly visible from Fig. 1.2. Historically, it was the flat rotation curves of galaxies which did the most in convincing the scientific community of the existence of Dark Matter.

1.1.2 Gravitational lensing

Einstein's theory of General Relativity states that light does not propagate in straight lines, but travels following geodesic paths whose direction depends from the geometry of space-time. If an intense gravitational field (i.e. a large mass distribution) is present between a source of light and the observer, the geodesic path deviates from a straight line, giving rise to the effect of gravitational lensing. A spectacular effect of gravitational lensing, where the light is deformed to show a ring, can be seen in Fig. 1.3. The curvature of light can be used to infer the mass of the object interposed between the source of light and the observer. This method allowed to measure discrepancies between the value of the mass computed taking into account the effect of gravitational lensing and the mass derived from the visible matter of the object. This once again leads to the hypothesis of the presence of Dark Matter.

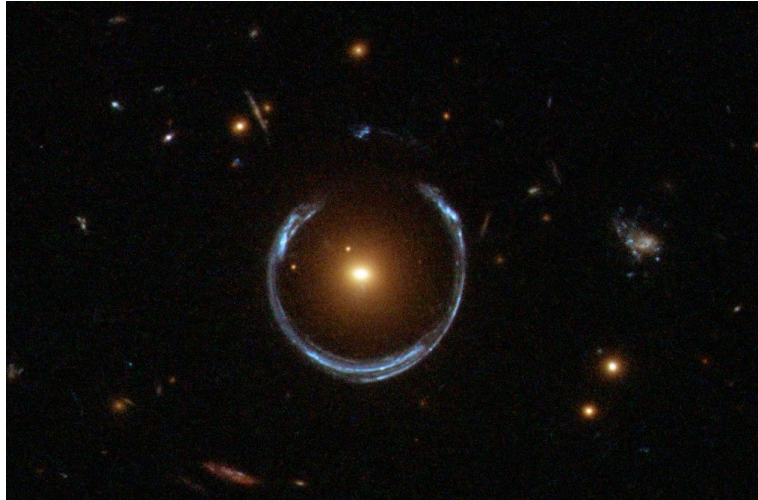


Figure 1.3: Example of gravitational lensing. The source of light is the blue star in the background, while the object deviating the light is the yellow star at the front. The effect of gravitational lensing is the blue ring around the yellow star.

1.1.3 The Cosmic Microwave Background

The two evidences discussed above manifest themselves at distances of the scale of the size of galaxies and of clusters of galaxies; at cosmological scale, an analysis of the *Cosmic Microwave Background* (CMB) can provide a third evidence of the existence of Dark Matter and even determine the total amount of Dark Matter present in today's Universe.

The CMB is an electromagnetic radiation with a black-body spectrum at a temperature of $T_{CMB} = 2.73$ K, filling every angle of the observable Universe. Its origin dates back to the *epoch of recombination*, i.e. 379000 years after the Big Bang, when the Universe became transparent to photons (before this, matter and light were strongly coupled and photons were not free to propagate). The CMB is known to be isotropic up to relative fluctuations of 10^{-5} : from an accurate

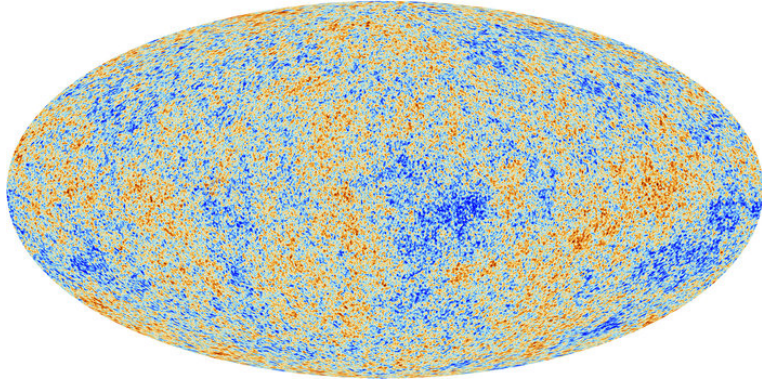


Figure 1.4: Anisotropies of the CMB measured by the PLANCK experiment.

analysis of the CMB anisotropies the composition of today's Universe can be inferred. The latest and most precise measurement of the CMB was carried out by the PLANCK experiment (ESA) (Fig. 1.4): PLANCK's measurements allowed to determine that today's Universe is made up by 5% of ordinary matter, 27% of Dark Matter and 68% of Dark Energy [19].

During this overview of evidences of the existence of Dark Matter, it was tacitly assumed that Dark Matter is made up by particles, exactly like ordinary matter. However, the astrophysical phenomena mentioned above could be explained without calling into question the existence of hidden mass, but simply modifying Newtonian dynamics and the laws of General Relativity. The attempt of providing a new law of gravitation which could explain the observed behaviour of galaxies without assuming the existence of hidden mass lead to the MoND theory (Modified Newtonian Dynamics) [18] and its relativistic generalization, TeVeS. Given that almost 40 years after the first observational evidence of the existence of Dark Matter (the observation of flat rotation curves of galaxies) there is still a lack of direct observation of Dark Matter particles [3], one could be inclined to give MoND theory a possibility. However, MoND theory has outstanding problems: one for all, the observation in 2006 of the Bullet Cluster [4] - a pair of colliding galaxy clusters - which showed an offset of the "hidden mass" with respect to the visible mass³. The offset is clearly visible in Fig. 1.5, where the hidden mass (blue) from the two clusters is leaving behind the visible mass (pink). This is indeed the effect to be expected if one assumes that Dark Matter is present in the galaxy clusters: being Dark Matter essentially collisionless⁴, the halos would pass through each other, while the cluster gas would interact and its center of mass would be at the collision point. On the other hand, MoND would expect the the apparent "hidden mass" feature to be centered on the visible mass. Nevertheless the strongest evidence against MoND came from the observation of NGC1052-DF2, a galaxy lacking dark matter [12]. Paradoxically, if MoND theory were true, a "dark matter" signature should always be present in every galaxy, because it is an unavoidable consequence of the presence of ordinary matter, which follows in this case a modified gravity law.

1.2 Dark Matter candidates

Despite having collected compelling evidence of the existence of Dark Matter, its nature is yet to be understood. A long-held paradigm is that Dark Matter is made up by particles belonging to the family of WIMPs (*Weakly Interacting Massive Particles*), i.e. neutral stable (or at least extremely

³The visible mass in the clusters was inferred from X-ray and optical observations, while the hidden mass was recovered exploiting the effect of gravitational lensing

⁴It can be safe to assume that at the scale of the size of galaxy clusters, Dark Matter interacts only through gravitational force.

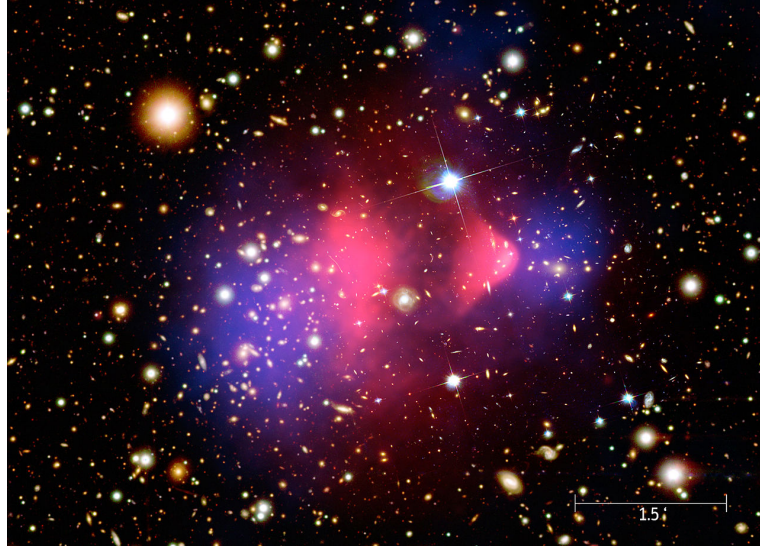


Figure 1.5: Picture of the Bullet Cluster observed with X-rays (pink) superimposed on a reconstruction of the hidden mass distribution calculated with gravitational lensing (blue).

long lived)⁵ particles with a mass lying between 10 GeV and 1 TeV⁶. Alternative proposals circulated in the past years (e.g. WISPs (*Weakly Interacting Sub-eV Particles*), as summarized in [3], [20]. The WIMPs hypothesis has been for decades the most credited explanation of the nature of Dark Matter for two main reasons:

- WIMPs are predicted by a number of well-motivated and consistent theories extending the SM, such as *Supersymmetry* and *Extra Dimensions*.
- The relic abundance of Dark Matter is consistent with a Dark Matter particle of mass in the WIMP mass range. This is known as the *WIMP miracle*. This argument is based on the assumption that Dark Matter was created thermally in the early stages of the Universe.

The WIMP miracle

Let's assume that Dark Matter was created thermally shortly after the Big Bang.

Let's consider a Dark Matter particle χ and a SM particle X . In the early hot Universe SM species and Dark Matter were in thermal equilibrium: the reaction



happened in both directions at equal rates, so that the annihilation and the creation of DM and SM species were balanced. As the Universe cooled down, assuming that the mass of the DM particle is much larger than the mass of the SM particle, the thermal energy available in the Universe became insufficient to allow the reaction



and the only reaction which could occur was the annihilation of DM particles:



causing their density to drop. The continuous expansion of the Universe makes it increasingly harder for a Dark Matter particle to find a partner to annihilate with and the forward reaction

⁵It is assumed that a Dark Matter species must be stable or at least have a lifetime comparable with the age of the Universe because Dark Matter is known to influence the formation of the structure of the Universe.

⁶It is useful to stress that Dark Matter is not necessarily made up by a single particle species, but there could be an entire zoo of Dark Matter particles.

shuts off. At this point, the Dark Matter density remains frozen in time. This process follows the Boltzmann equation

$$\frac{dn}{dt} + 3Hn = -\langle\sigma v\rangle(n^2 - n_{eq}^2), \quad (1.4)$$

where n is the DM particles numeric density at time t , H is the Hubble expansion rate, $\langle\sigma v\rangle$ is the thermally averaged annihilation cross section of χ multiplied to their velocity, and n_{eq} is the numeric density of DM particles at thermal equilibrium with the Universe. Being a quantity defined at thermal equilibrium, n_{eq} follows the Boltzmann distribution:

$$n_{eq}(T) = g \left(\frac{mT}{2\pi} \right)^{3/2} e^{-m/T}, \quad (1.5)$$

where m is the mass of the particle χ and T is the temperature. From Boltzmann's equation one can compute today's relic density of the Dark Matter particle χ as

$$\Omega_\chi h^2 \approx \frac{3 \times 10^{-27} \text{cm}^3 \text{s}^{-1}}{\langle\sigma v\rangle} \simeq 0.1 \left(\frac{0.01}{\alpha} \right)^2 \left(\frac{m}{100 \text{ GeV}} \right), \quad (1.6)$$

where $h = H_0/100 \text{ kms}^{-1} \text{Mpc}^{-1}$ and H_0 is today's Hubble constant, α is the coupling strength and m is the mass of the Dark Matter particle χ . For the details of this calculation see [16]. Assuming a weakly interacting Dark Matter particle with $\alpha \sim 0.01$ and mass $m \sim 100 \text{ GeV}$, i.e. assuming that χ is a WIMP, Eq.(1.6) gives the correct Dark Matter relic density today as measured by the PLANCK experiment [19]:

$$\Omega_{DM} h^2 = 0.1186 \pm 0.0020. \quad (1.7)$$

Currently there are three theoretical frameworks incorporating WIMP-like particles which are viable Dark Matter candidates:

1. **Supersymmetry.** The supersymmetric extension of the SM expects a complete symmetry between fermions and bosons: each $1/2$ -spin particle of the SM has a supersymmetric integer-spin particle, called superpartner, and vice-versa, i.e. every SM boson has a fermionic superpartner. In supersymmetric models with R-parity conservation, the lightest supersymmetric particle, the *neutralino* χ^0 , is stable, and thus becomes a perfect DM candidate.
2. **Extra dimensions.** Following the idea of a theory of everything which could include all four fundamental interactions, theories where the spatial dimensions are increased from three to four were developed. The theories with unified extra dimensions expect particles which can be regarded as Dark Matter candidates.
3. **Simplified Dark Matter models.** Simplified Dark Matter models are crucial for Dark Matter searches at colliders. They are able to describe the full DM kinematics with a reduced number of free parameters. Provided that they are simple enough to form a credible unit with a more complicated model, that they manage to describe the kinematic behaviour of DM particles at colliders, and, finally, they satisfy the low-energy constraints on DM searches, Simplified DM models can be used in practice to probe the production of DM particles at colliders. The large number of parameters (~ 20) of complete BSM (Beyond the Standard Model) models - like the ones described above - makes their structure so rich that it is extremely complicated to use them as a guideline for DM searches at colliders. On the other hand, Simplified DM models involve only a few parameters, describing the DM particle characteristics and its coupling to SM particles. For an in-depth review on Simplified DM models for Dark Matter searches at LHC, see [1].

For a thorough description of DM candidates, especially WIMP-like candidates, see [3].

1.3 Detection strategies

Three different detection strategies are explored below. Each of them exploits a different coupling of DM particles with SM particles, as Fig. 1.6 summarizes. While experiments following the direct approach seek to detect DM particles coming from the outer space and passing through Earth, the indirect approach is based on detecting SM decay products of those DM particles. Finally, searches at colliders aim to detect DM particles produced in a pp collision, i.e. through interaction of SM particles.

1.3.1 Direct searches

Direct searches of Dark Matter WIMPs are based on the assumption that, if the Milky Way is filled with WIMPs, a flux of them may pass through the Earth and weakly interact with ordinary matter. The experiments adopting the direct approach search for the interaction of such particles with the detecting material, e.g. by measuring the recoil energy of nuclei as WIMPs scatter off them.

The WIMP interaction with the detector's nuclei can have different features: it could be either

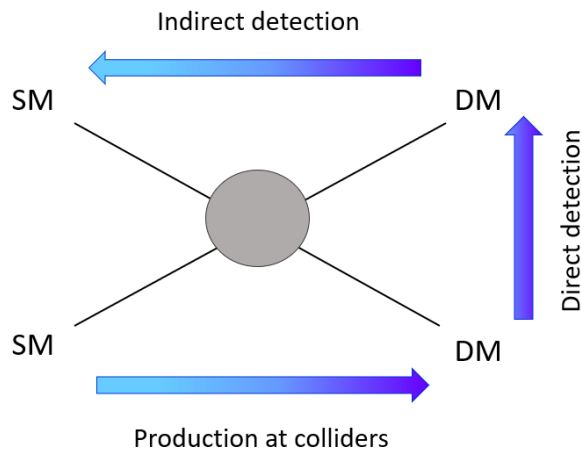


Figure 1.6: This diagram sums up a few examples of interaction between Dark Matter particles and SM particles exploited by various approaches of detection. In direct detection a WIMP scattering off a nucleus is directly revealed by measuring the nuclear recoil energy; the indirect detection approach consists in looking for the SM decay products of Dark Matter particles; at colliders Dark Matter particles are expected to be produced in pp collisions, i.e. from SM particles.

elastic or inelastic, and on top of this, it could be both spin-dependent and spin-independent. The elastic scattering of a WIMP off a nucleus is the interaction of the WIMP with the nucleus as a whole, causing it to recoil. The aim would be then to measure the recoil energy of the nucleus, to infer the energy of the WIMP. On the contrary, inelastic interactions do not cause a recoil of the nuclear target: instead, WIMPs either interact with electrons surrounding the nucleus ionizing the atom or interact directly with the nucleus, leaving it in an excited state. In the first case, the signature of a WIMP passing through the detector would be a path of ionized atoms; in the second case, the excited nuclei would fall back into the ground state emitting a photon, whose energy could be measured. Furthermore, if the interaction is spin-independent, the WIMP is expected to scatter coherently across the nucleus, and have equal coupling strengths with neutrons and protons. On the other hand, if the interaction is spin-dependent, the coupling strength with nucleons is expected to be different between protons and nucleons and to depend on whether the net nuclear spin is carried by a residual neutron or proton.

The main challenge faced by experiments based on direct detection is discriminating between

WIMP signatures and background. Sources of background are cosmic rays and natural radioactivity of the environment and of the detector itself. To shield the detector from cosmic rays, the experiments are often located underground, while radioactivity from the environment is kept outside the detector providing it with a shielding shell. The radioactivity of the detector itself is tackled by employing extremely radio-pure materials. Another method to deal with backgrounds is to exploit the fact that the Earth is moving through the DM halo which surrounds our galaxy, yielding a “WIMP wind”. This should, in principle, create a small “annual modulation” in the detected WIMP rates: one could in this way discriminate WIMPs from backgrounds, provided that the latter does not present an annual modulation too. The DAMA experiment, located under Gran Sasso mountain and made up by extremely radio-pure NaI(Tl) crystals, observed an annual modulation of their event rate consistent with the detection of a WIMP species with a mass of approximately 40 GeV and a scattering cross section of $\sim 10^{-41} \text{ cm}^{-2}$ [2]. However, the results achieved by DAMA could not be replicated by other experiments, such as EIDELWEISS III and CDMS: studies on DAMA’s results are on-going.

1.3.2 Indirect searches

Another method for searching for Dark Matter is based on the indirect detection strategy. Indirect detection of Dark Matter is the technique of observing the radiation produced in DM particles’ annihilations. The flux of the decay products is proportional to the annihilation rate of the Dark Matter particles, which is in turn proportional to the square of the Dark Matter density. Therefore significant fluxes of DM particles’ decay products could come from locations with high densities of Dark Matter, e.g. galactic centers. These decay products are SM particles, therefore they can be detected with conventional techniques. DM particles’ annihilation products can be cosmic rays, neutrinos, positrons or anti-protons. The main background sources for experiments employing the indirect approach is certainly the detection of the same particles (e.g. cosmic rays, neutrinos, etc.) expected from annihilation of Dark Matter, except that they originate from “ordinary” astrophysical phenomena. For this reason, the indirect strategy focuses on finding an excess in the flux of the annihilation products with respect to theoretical expectations; furthermore, identifying the possible source of the flux and observe whether it could be a region containing a large density of Dark Matter could help to discriminate between background and DM decay products.

1.3.3 Search at colliders

Exactly like a WIMP can scatter off a nucleus, Dark Matter particles can, in principle, be produced at hadron colliders from pp collisions, therefore it is possible to probe them at experiments at colliders.

Assuming that a WIMP is produced from a pp collision, it would not decay inside the detector (WIMPs are, as already mentioned, stable), therefore it would escape without being detected. However, the presence of a WIMP would leave a particular signature inside the detector. The total momentum in the transverse plane, i.e. the vectorial sum of the transverse momenta p_T of the particles produced in a pp collision is expected to amount to zero. Therefore, if the detector is not able to see one particle, e.g. a WIMP, its presence can be inferred from a transverse momentum imbalance, i.e. a missing transverse momentum. Missing transverse momentum is thus a primary signature of the presence of a Dark Matter candidate.

There are two possible approaches which can be followed when searching for Dark Matter at colliders:

- The first approach consists in looking for all decay channels expected in a determined theoretical framework, e.g. Supersymmetry, which incorporates Dark Matter candidates.
- The second approach is consists in searching for a particular Dark Matter signature. Let’s consider a Dark Matter particle, manifesting itself as a missing transverse momentum, pro-

duced in pair with a detectable SM object: the two decay product would recoil against each other, leaving in the detector an event with a large missing transverse momentum and a SM particle. The presence of a SM particle is necessary to tag the event: otherwise the event would not be even observed, as Fig. 1.7 shows. The SM object, which could be a jet, a photon, a vector boson (W^\pm or Z) or a Higgs boson, gives the name to these signatures, called *mono-X signatures*, where X is the SM object used to tag the event. Mono- X signatures at colliders are interpreted in the light of Simplified DM models. These searches look for an excess of events with the mono- X signature with respect to SM processes expecting the same signature.

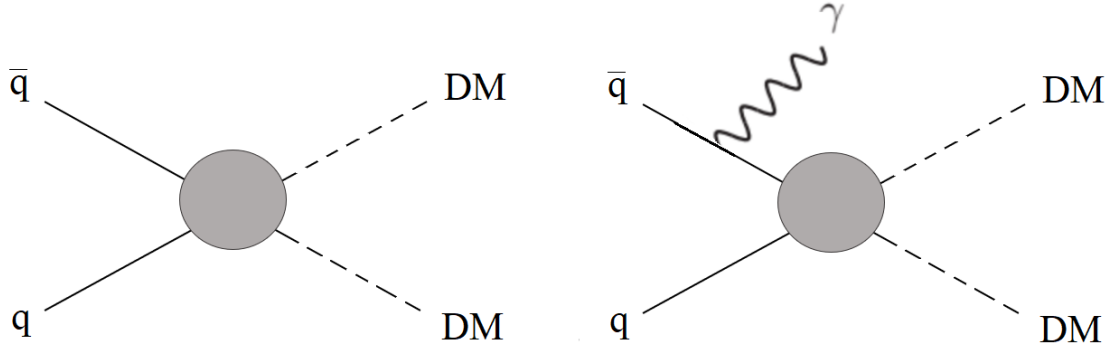


Figure 1.7: The event on the left cannot be triggered by ATLAS detector: an E_T^{miss} value cannot be measured if there is no other detectable particle produced in the event. On the contrary, the presence of the photon (playing the role of the detectable SM physics object X), makes it possible to measure a E_T^{miss} value.

CHAPTER 2

The Large Hadron Collider and the ATLAS experiment

This chapter will present the main features of the Large Hadron Collider and provide a summary of the detectors of the ATLAS experiment.

2.1 The LHC

The LHC [13] was built at CERN, near Geneva, and is located in a circular tunnel 27 km long beneath the border between Switzerland and France. Since it started and up to this day, LHC is the largest and most powerful particle accelerator in the world. The LHC was designed to achieve a center-of-mass energy of $\sqrt{s} = 14$ TeV with an instantaneous luminosity of $10^{34} \text{ cm}^{-2}\text{s}^{-2}$ (for proton-proton collisions). The data used for the work presented in this thesis were collected by the ATLAS detectors between 2015 and 2016, when the LHC operated at a center-of-mass energy of $\sqrt{s} = 13$ TeV and amounted to an integrated luminosity of $L = 36 \text{ fb}^{-1}$. LHC is mainly employed as a proton-proton collider, but is also used to make head-on collisions between heavy ions.

2.1.1 Proton-proton interactions and the LHC structure

Proton-proton collisions at high energies are studied at the LHC experiments to validate the Standard Model's predictions and to explore physics beyond the Standard Model (BSM).

One can identify two different kinds of proton-proton interactions taking place in the four collision points of LHC:

Soft collisions: Soft collisions are long-distance interactions between protons with low momentum transfer: the particles produced as a result of a soft collision have low transverse momentum and scatter at small angles. In soft interactions, the protons' internal structure does not come to light.

Hard collisions: Hard collisions involve a short-distance interaction between protons, and can be considered as collisions between the partons carried by the protons. Hard interactions involve parton-parton interactions with large momentum transfer, which can result in production of high transverse momentum and high mass particles at large angles. These events are rare, compared to soft collisions.

The latter are the most interesting from an experimental point of view. However, the interesting rare processes originating from hard collisions are often exceeded in number either by events from soft collisions or by QCD processes. This gives rise to a challenge for the detectors at the LHC: interesting hard collisions happen simultaneously to a much higher number of soft collisions, therefore signals from hard processes can be overshadowed by background signal. A signal as neat as possible needs to be obtained by the detectors at the LHC, in order to distinguish interesting processes from background events. Events from soft collisions do not always constitute background events: they are recorded and studied to grasp a better understanding of the physics of the Standard Model.

The pp collisions take place in four collision points along the tunnel, corresponding to the position of the four main experiments at LHC: ATLAS, CMS, LHCb and ALICE. LHCb and ALICE have specific purposes: LHCb is a b-physics experiment, i.e. concentrates on studying the

parameters of CP-violation in B-hadron decays, while ALICE is optimized to observe heavy-ion collisions and study interactions in the quark-gluon plasma produced during the collisions. On the contrary, ATLAS and CMS are general purpose experiments: they are designed to measure the broadest possible variety of signals, whether they originate from SM processes or from new physics.

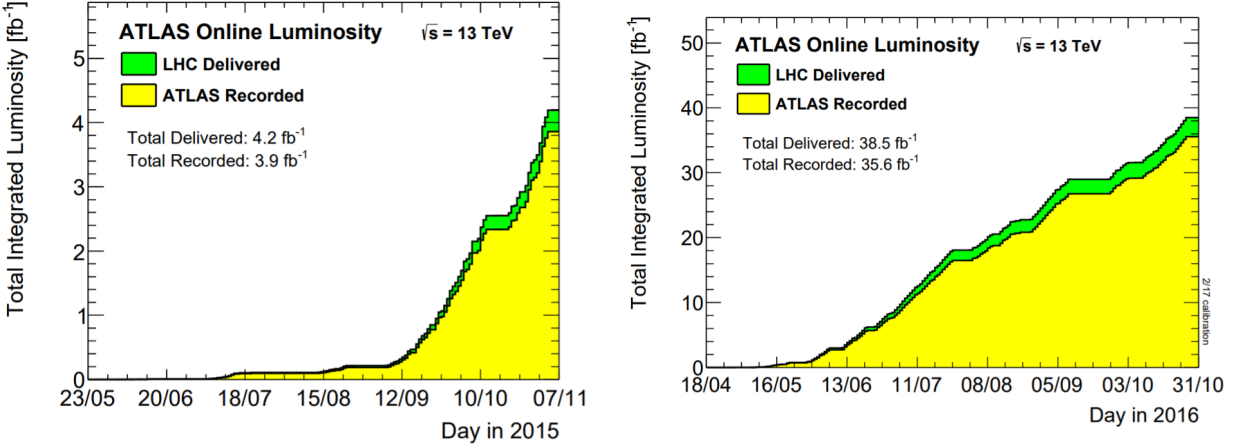


Figure 2.1: Integrated luminosity delivered by the LHC’s stable beams (green) and measured by ATLAS (yellow) as a function of time in 2015 (left) and 2016 (right). From [21].

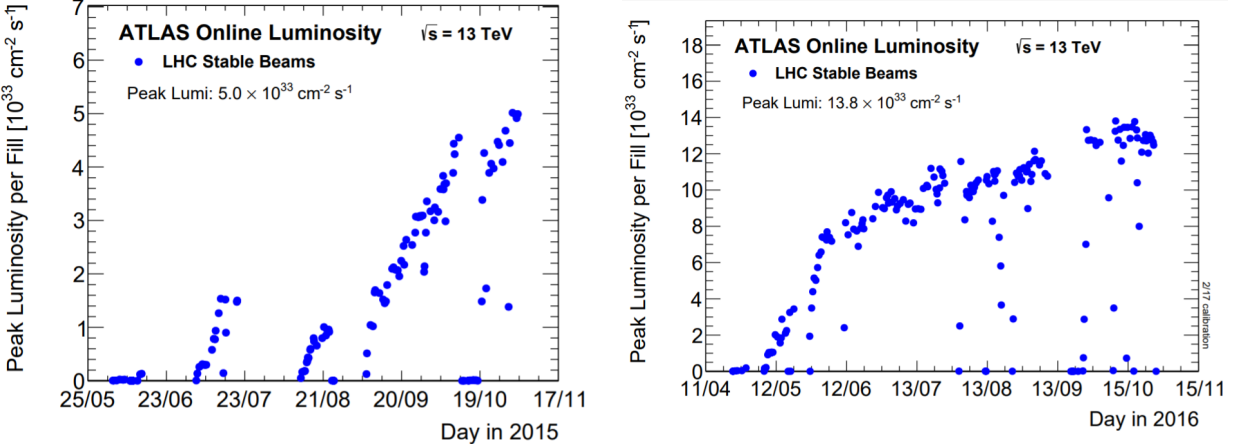


Figure 2.2: Peak instantaneous luminosity delivered to ATLAS by the LHC’s stable beams as a function of time in 2015 (left) and 2016 (right), during pp collisions at a center-of-mass energy of $\sqrt{s} = 13$ TeV. From [21].

The protons travel inside two separate adjacent beamlines in opposite directions along the LHC ring. Each proton beam contains 2808 bunches, and each bunch is made up by 1.5×10^{11} protons. Being the protons bunched together, the collisions take place at discrete time intervals: interaction are, starting from Run2¹, 25 ns apart. The instantaneous luminosity at LHC² can be computed as

$$\mathcal{L} = \frac{n_{beam} N_{bunch}^2 f_{rev} \gamma}{4\pi \epsilon_n \beta^*}, \quad (2.1)$$

¹Run2 is the second operational run of LHC. It started in April 2015 and is scheduled to stop in December 2018.

²The instantaneous luminosity is the ratio of the number of events detected at a certain time to the cross section of the interaction involved in the events. The number of events N detected during selected time interval is thus proportional to the integrated luminosity through the processes’ cross section.

where n_{beam} is the number of bunches per beam, N_{bunch} is the number of protons per bunch, f_{rev} is the revolution frequency of a bunch around the ring, γ is the relativistic factor, ϵ_n is related to the r.m.s. of the protons' position and momentum distributions along the ring, and β^* reflects the transverse size of the particle beam, which is $\sim 16 \mu\text{m}$ at the interaction point. As Fig. 2.2 shows, the instantaneous luminosity delivered by the LHC during stable beams reached a peak value of $5 \times 10^{33} \text{ cm}^{-2}\text{s}^{-1}$ in 2015, which was topped by the peak value of $13.8 \times 10^{33} \text{ cm}^{-2}\text{s}^{-1}$ achieved in 2016. From Fig. 2.1 one can notice that the total integrated luminosity delivered by the LHC in 2015 and 2016 was 4.2 fb^{-1} and 38.5 fb^{-1} respectively.

The acceleration of the protons is delivered by eight Radio-Frequency (RF) cavities per beam: each cavity can achieve a maximum accelerating voltage of 2 MV, tuned to oscillate with a frequency of 400 MHz. The timing of the protons is crucial: an ideally timed proton at the nominal energy of $\sqrt{s}/2$ will see no accelerating field while passing through the cavities, while later or earlier protons with a slightly different energy will be accelerated or decelerated such that their energy will approach the nominal value. This is the mechanism separating the proton beams in bunches. Superconducting dipole magnets (Fig. 2.3, left) are needed to keep the two proton beams on a circular path along the ring, while superconducting quadrupole magnets (Fig. 2.3, right) focus the beams. Superconducting magnets of higher multipole order are employed to correct small imperfections in the trajectory of the beams. The superconducting magnets delivering the electromagnetic fields of the RF cavities need a temperature of 4.5 K to operate, while the deflecting dipole magnets work at 1.9 K.

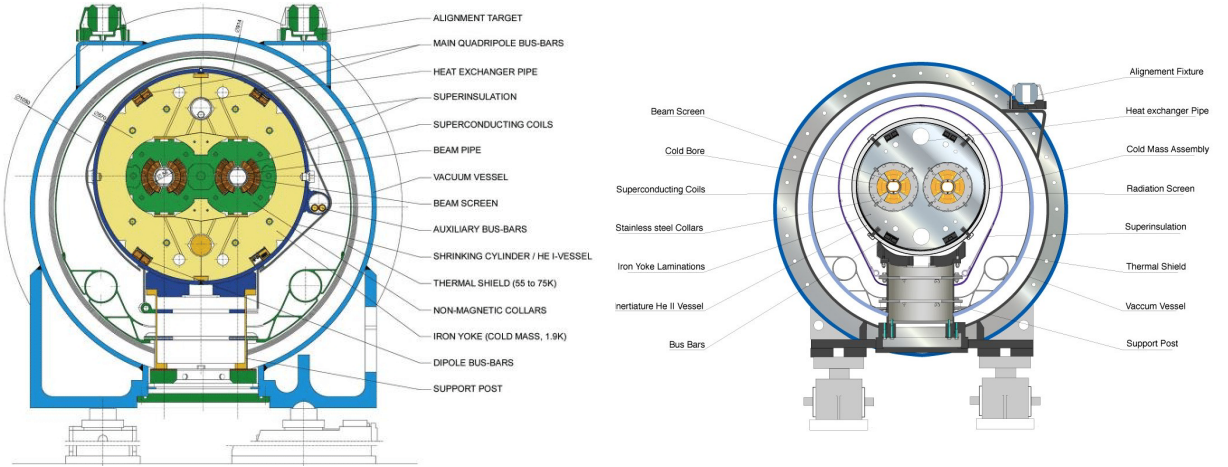


Figure 2.3: Cross sections of the LHC ring with a dipole magnet (left) and a quadrupole magnet (right). One can also notice the two adjacent beam pipes where the two proton beams travel in opposite directions. From [17].

2.1.2 The accelerator complex

When protons are injected into the LHC ring, their energy is 450 GeV: the RF cavities then accelerate each proton beam to a maximum energy of 6.5 TeV. Protons at 450 GeV are delivered to LHC by a chain of pre-accelerators. The protons source is a simple bottle of hydrogen: applying an electric field one is able to separate the electron of the hydrogen atom from its nucleus. The free protons are then collected by the linear accelerator LINAC2 and accelerated to an energy of 50 MeV: the second step of the accelerator chain is the Synchrotron Booster, where the proton energy reaches 1.4 GeV. The Proton Synchrotron (PS) accelerates the protons to an energy of 25 GeV and the protons finally achieve an energy of 450 GeV in the Super Proton Synchrotron (SPS), before being injected into LHC. CERN's complete accelerator facility is shown in Fig. 2.4.

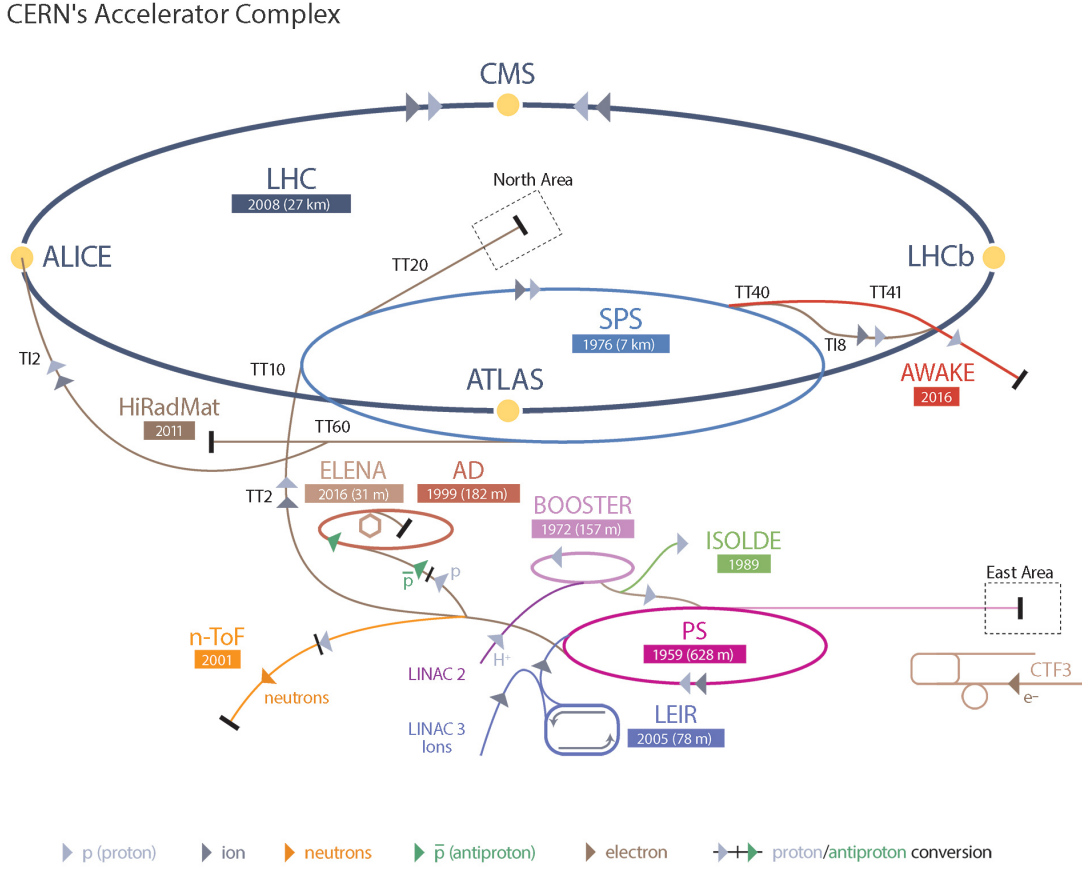


Figure 2.4: This picture shows CERN’s accelerator complex. One can follow the proton path starting from LINAC2 to the LHC, passing through the whole accelerator chain (Synchrotron Booster, PS, SPS).

2.2 The ATLAS experiment

ATLAS (A Toroidal LHC ApparatuS) [9] is a general-purpose experiment; ATLAS is designed to take advantage of the full discovery potential provided by the huge energies available at LHC. Data-taking started at the end of 2009, when ATLAS observed its first proton-proton collision. After a shut-down between 2013 and 2014, in 2015 (Run2) ATLAS started recording collisions of proton beams at 6.5 TeV.

ATLAS is the largest particle detector ever built for a collider: its cylindrical structure, located in a cavern around Point 1³, has a length of 46 m, a diameter of 25 m and weighs about 7000 tonnes. ATLAS’ cylindrical geometry is mainly driven by three superconducting toroid magnets (one barrel and two end-caps). The detector shows a forward/backward symmetry around the interaction point, surrounding it completely. The ATLAS detector can be divided into three major parts: the **Inner Detector**, the **calorimeter**, and the **Muon Spectrometer**. The three sub-detectors are complementary: the Inner Detector tracks charged particles, the calorimeters measure the energy of photons and electrons or hadrons, and the muon system provides tracking measurements of highly penetrating muons. A 2 T **solenoid magnet** surrounds the Inner Detector, allowing measurements of the momentum of charged particles, and the **toroid magnet** plays the same role for the Muon Spectrometer. The ATLAS sub-detectors and their role in detecting different physics objects is summarized in Fig. 2.5.

³One of the collision points at the LHC ring.

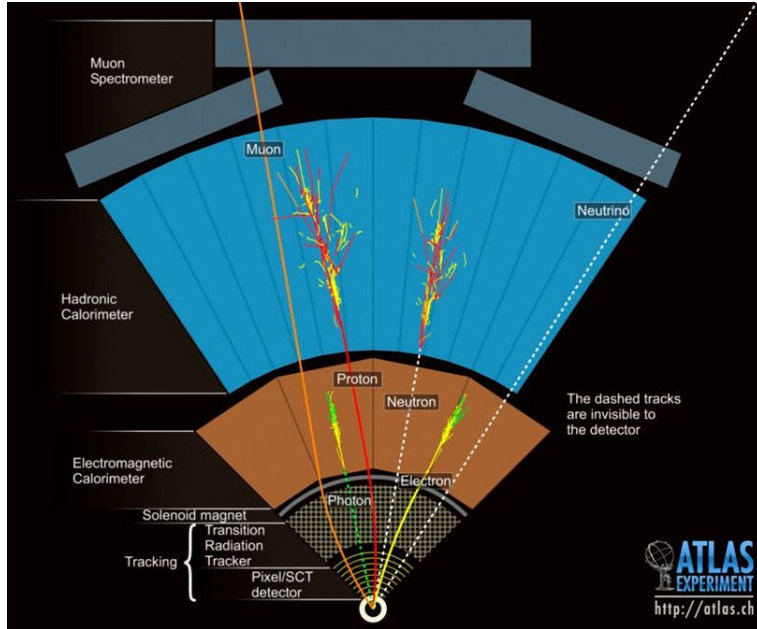


Figure 2.5: A slice of the ATLAS detectors is shown here. One can see how neutral particles escape the Inner Detector undetected, the electromagnetic showers (see section 1.2.2) generated by electrons and photons interacting with the Electromagnetic Calorimeter, the hadronic showers generated by neutral and charged hadrons interacting with the Hadronic Calorimeter, and finally muons, whose trajectory is bent by the Muon Spectrometer in order to obtain momentum measurements. Neutrinos are the only particles able to escape the ATLAS detector without interacting with any sub-detector, but their presence can be inferred by a measure of E_T^{miss} of the calorimeters.

A particle's position inside the ATLAS detector can be described through the coordinate system (x, y, z) , whose origin coincides with the interaction point. The z -axis' direction is along the beam, while the xy plane is transverse to the beam. The x -axis points to the center of the LHC ring, while the y -axis points upward. The transverse plane xy is described by the set of coordinates (η, ϕ) :

- η is defined by the relation

$$\eta = -2 \ln \left(\frac{\theta}{2} \right), \quad (2.2)$$

where θ is the polar angle, measured as usual with respect to the z -axis. The variable η is known as *pseudorapidity*.

- ϕ is the azimuthal angle, measured with respect to the x -axis around the beam direction.

The angular distance between two points can be computed as

$$\Delta R = \sqrt{(\Delta\eta)^2 + (\Delta\phi)^2}. \quad (2.3)$$

The so-called transverse quantities, e.g. p_T , E_T , and E_T^{miss} are defined in the transverse plane xy .

2.2.1 The Inner Detector

The Inner Detector (ID), shown in Fig. 2.6, constitutes the inner-most layer in the ATLAS experiment. The ID is enclosed in a cylindrical envelope whose length and diameter are 6.2 m and 2.1 m; it spans from a radius of 31 mm to a radius of 1082 mm from the beam pipe and it is composed by a barrel and two end-caps, to cover a pseudorapidity region of $|\eta| < 2.5$. The ID provides tracking and momentum measurements for charged particles, as well as recognizes both the primary and secondary vertex.

Given the high number of tracks left by particles passing through the detector at a certain time (approximately 1000 particles emerge from the collision point every 25 s), high-granularity detectors are needed to provide high-precision measurements of tracking parameters. The role of the Inner Detector is crucial for the reconstruction of electrons and photons: as it will be explained in Chapter 4, the traces left in the ATLAS detector by electrons and photons differ only in the ID.

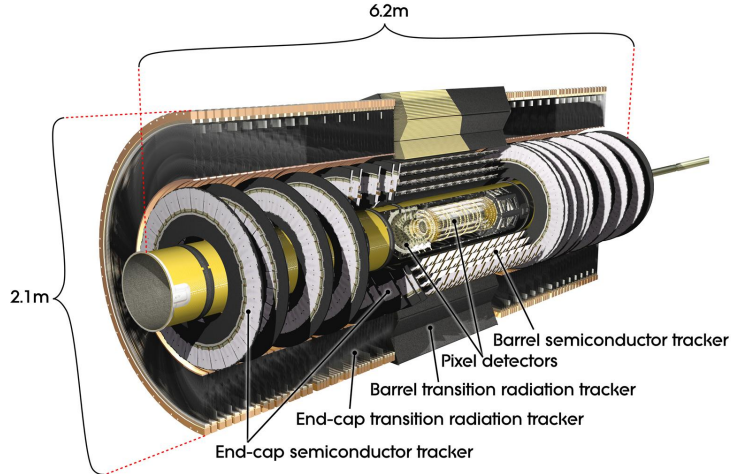


Figure 2.6: A computer-generated illustration of the Inner Detector.

The Inner Detector is composed by three independent but complementary sub-detectors:

- The **Pixel Detector** is the first detector crossed by the particles produced in the pp interactions. The system consists of three barrels at radii of 50.5 mm, 88.5 mm, and 122.5 mm from the beam line, and three disks on each side. A fourth layer in the barrel, called Insertable B-Layer, was placed at a distance of 31 mm from the beam line between Run1 and Run2. The Pixel Detector contains 1744 modules (1456 modules in the barrels and 288 modules in the end-caps): each of them is a wafer of silicon 62.4 mm long and 21.4 mm wide, with 46080 pixel elements. Each pixel has a size of $R - \phi \times z$ of $50 \times 400 \mu\text{m}^2$: this is to provide high-granularity, high-precision sets of tracking measurements as close to the interaction points as possible. Typically, three pixel layers are crossed by each track.
- The **Semi-Conductor Tracker (SCT)** is a silicon microstrip tracker, made up of 4088 modules and over 6 million implanted readout silicon strips. Each module has an area of $63.6 \times 64.0 \text{ mm}^2$ and is equipped with 780 readout strips. In the barrel region, the modules are arranged in four cylinders made of two layers of sensors placed with a $10 \mu\text{rad}$ stereo angle, to provide also a z -coordinate measurement, in addition to R and ϕ measurements. The SCT is placed at medium radii: $299 \text{ mm} < R < 514 \text{ mm}$.
- The **Transition Radiation Tracker (TRT)** is the outer layer of the Inner Detector. The inner and the outer radii of the TRT cylindrical structure are 554 mm and 1082 mm. The detector works both as a straw tracker and a transition radiation detector. The detecting elements are drift tubes (straws), filled with gas which becomes ionized when a charged particle hits the straw. A fixed voltage drives the oppositely charged ions to the opposite ends of the straw: the collected charge generates a hit signal, allowing the reconstruction of the particle's track. The TRT has a poorer spatial resolution than the Pixel Detector and the SCT; on the other hand, it can provide a very large number of hits per track (approximately 36). The 50000 straws in the barrel region are 144 cm long and parallel to the beam axis, while the end-caps contain 250000 39 cm long straws distributed radially. Between the straws, materials with different refraction index cause ultra-relativistic charged particles to produce

transition radiation; this causes extremely strong hit signals to be recorded by the straws crossed by particles with a high γ factor. This feature allows to discriminate electrons from pions.

The global relative momentum resolution achieved by the ID [10] was measured to be

$$\frac{\sigma_p}{p} = (4.83 \pm 0.16) \times 10^{-4} \text{ GeV} \times p_T, \quad (2.4)$$

where p_T is the transverse momentum.

2.2.2 The calorimeters

The purpose of the ATLAS calorimeters is to measure the energy of all charged and neutral particles, except for the highly penetrating muons. To measure the energy carried by an incident particle, the material making up the calorimeters fully absorbs it and transforms its energy into a measurable quantity (e.g. scintillation light or electric charge). Interacting with the calorimeter (through electromagnetic or strong force), an incident particle produces a *shower* of secondary particles with progressively degraded energy. The energy deposited in the active material of the calorimeter by the secondary particles is then collected and measured. The ATLAS calorimeters are examples of *sampling calorimeters*: sampling calorimeters are made up of alternating layers of *absorbing material* and *active material*. The absorbing material degrades the energy of the incident particles creating secondary showers, while the active material collects the deposited energy providing a measurable signal. For an in-depth review of calorimetry for particle physics see [14].

To successfully measure the energy of an incident particle, the calorimeter needs to absorb its energy completely, i.e. needs to contain the whole shower: the thickness of the calorimeter is required to satisfy this condition, also to avoid secondary shower leaks into the Muon Spectrometer.

ATLAS calorimetric system is composed by the **Electromagnetic Calorimeter (EM)**, the **Hadronic Calorimeter (Had)**, and the **Forward Calorimeter (FCal)**: the first is optimized to measure the energy of electrons and photons, the second specialises in jet reconstruction and E_T^{miss} measurements, while the third provides energy measurements for both electromagnetic and hadronic showers in the forward region. An overview of ATLAS calorimeters is shown in Fig. 2.7.

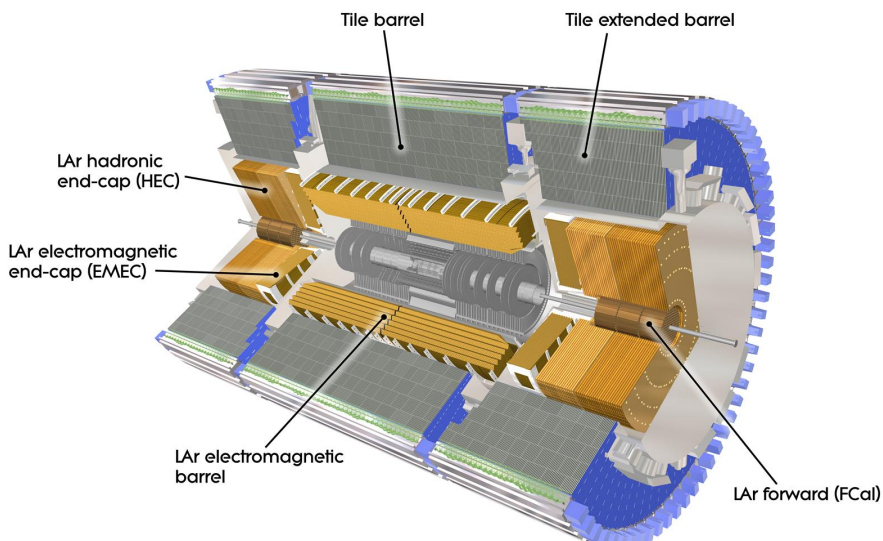


Figure 2.7: A computer-generated illustration of ATLAS calorimetric system.

The Electromagnetic Calorimeter

The Electromagnetic Calorimeter is a cylinder 6.65 m long and with an outer radius of 2.25 m; it is divided into a barrel part (covering a pseudorapidity region of $|\eta| < 1.4$) and two end-caps, where the coverage is $1.4 < |\eta| < 3.2$. The regions where the barrel meets the end-caps $-1.37 < |\eta| < 1.52$ are called *crack regions*. The EM is a sampling calorimeter where the active medium is liquid Argon, alternated with lead plates as absorbing materials. The liquid Argon layers are interleaved in copper electrodes, which collect the ionization charge generated by the electromagnetic showers. The copper electrodes and the lead plates are arranged into an accordion geometry, to achieve a full coverage with respect to ϕ . The liquid Argon works at a temperature of -183°C: each of the EM components is thus housed into its own cryostat.

As Fig. 2.8 shows, the EM is segmented in 190000 cells along η and ϕ and it is composed of four longitudinal layers to record the longitudinal development of the electromagnetic shower: the PreSampler (PS), Layer 1 (L1), Layer 2 (L2), and Layer 3 (L3). L1 has the finest granularity in η with $\Delta\eta$ up to 0.003: this fine segmentation is used to discriminate between prompt photons⁴ and two almost collinear photons as decay products of π^0 pions. The nominal relative energy resolution

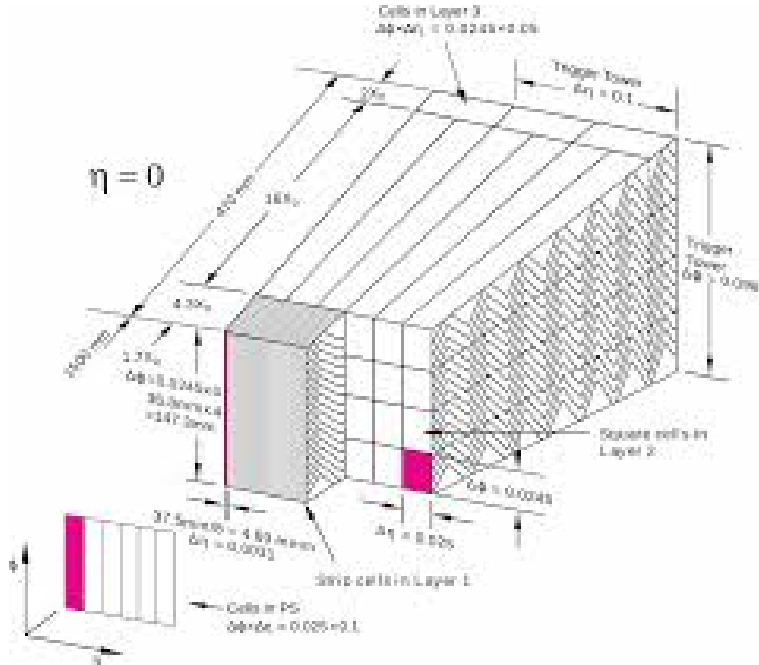


Figure 2.8: This picture shows the segmentation in the η and ϕ coordinates of the liquid-Argon calorimeter.

in the EM calorimeter is

$$\frac{\sigma_E}{E} \approx \frac{0.1 - 0.17}{\sqrt{E} \text{ (GeV)}} \oplus 0.007, \quad (2.5)$$

which is within the typical energy resolution of sampling electromagnetic calorimeters [14] ($\frac{\sigma_E}{E} = \frac{0.05 - 0.2}{\sqrt{E} \text{ (GeV)}}$).

The Hadronic Calorimeter

The Hadronic Calorimeter is 6.10 m long, has an outer radius of 4.25 m and its pseudorapidity coverage extends to $|\eta| < 3.2$. The Hadronic Calorimeter is divided in two sections: in the barrel region there is a sampling calorimeter using steel as an absorber and scintillating tiles as an active material, while the end-caps are liquid-Argon calorimeters using copper or tungsten as passive

⁴A prompt photon is a photon produced promptly at the pp collision.

materials, located behind the end-caps of the liquid-Argon of the EM. The former calorimeter is called Tile Calorimeter, while the latter is known as Hadronic End-cap Calorimeter. The nominal energy resolution for measuring the energy of hadronic jets is

$$\frac{\sigma_E}{E} \approx \frac{0.5}{\sqrt{E \text{ (GeV)}}} \oplus 0.03. \quad (2.6)$$

achieved by the combination of the Hadronic Calorimeter and the EM calorimeter.

The Forward Calorimeter

The Forward Calorimeter brings the pseudorapidity coverage of the ATLAS calorimetric system to $|\eta| < 4.9$. The FCal is made up of three modules in each end-cap: all modules use liquid Argon as active material; the first module uses copper as absorbing material while tungsten plays this role for the second and the third module. The first module delivers measurements of the energy of electromagnetic showers, while the last two modules mainly record the energy of hadronic showers. The typical energy resolution of the FCal is

$$\frac{\sigma_E}{E} \approx \frac{1}{\sqrt{E \text{ (GeV)}}} \oplus 0.1. \quad (2.7)$$

2.2.3 The Muon Spectrometer

Muons are, along with neutrinos, the only particles with the ability to escape the calorimeters without being absorbed: this is why their momentum is measured by a specifically designed detector, the Muon Spectrometer.

The Muon Spectrometer forms the outer layer of the ATLAS detector. The Muon Spectrometer geometry is mainly driven by the toroids' structure, visible in Fig. 2.9: it shows symmetry with respect to the ϕ coordinate and it is divided by the toroids into octants.

The magnetic field delivered by the toroid magnets bends the muon trajectories, allowing high precision measurements of the muons' momentum. The momentum measurement is carried out by muon chambers of two different types: Monitored Drift Tubes (MDTs) in the barrel and Cathode Strip Chambers (CSCs) in the end-cap region.

Two more types of muon chambers are present in the Muon Spectrometer: the Resistive Plate

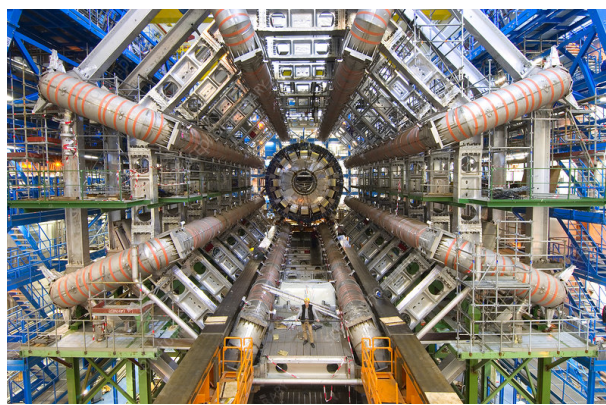


Figure 2.9: The toroids' structure is visible in this picture of the ATLAS detector, taken during its construction.

Chambers (RPCs) and the Thin Gap Chambers (TGCs) provide fast triggering on muon tracks respectively in the barrel region and in the end-caps.

The ATLAS muon system, in particular the MDTs, provides a momentum resolution between 2-3% and $\sim 10\%$ in a p_T range between 10 GeV and 1 TeV.

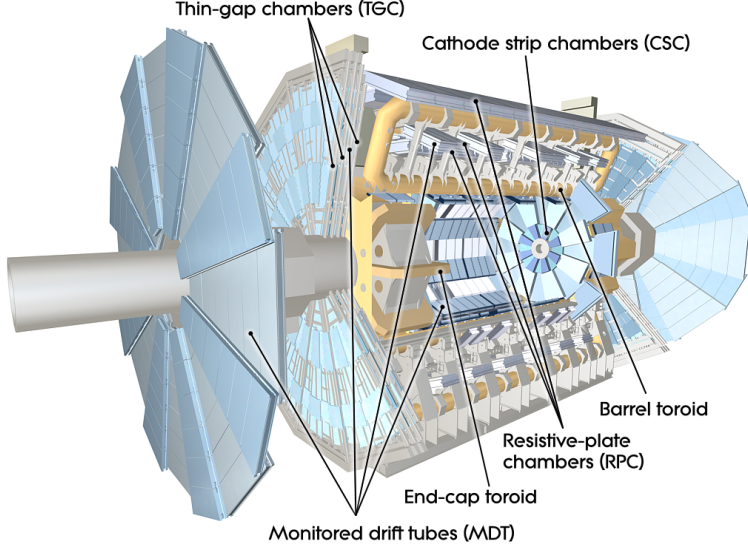


Figure 2.10: A computer-generated illustration of the Muon Spectrometer.

2.2.4 The trigger system

The ATLAS detector observes an unmanageable amount of data⁵: the trigger system identifies the most interesting events to retain for detailed analysis. The trigger system has two distinct levels: *L1* and the High Level Trigger (HLT). Each trigger level refines the decisions made at the previous level and, where necessary, applies additional selection. The first selection, made by *L1*, happens online: the *L1* trigger, basing its decisions on information retrieved immediately from the ATLAS detectors, searches for high transverse-momentum muons, electrons, photons, jets, τ -leptons decaying into hadrons, and large missing and total transverse energy. For each event, the *L1* trigger also defines one or more Regions-Of-Interest (ROIs) i.e. the spatial coordinates in η and ϕ of those regions within the detector where its selection has identified interesting features. The information held within the ROIs is then analyzed by the Event Filter. The offline selection carried out by the higher levels of the trigger system reduces the rate to 1 KHz: only then data can be stored and processed. Typical trigger rates for *L1* and HLT are shown in Fig. 2.11.

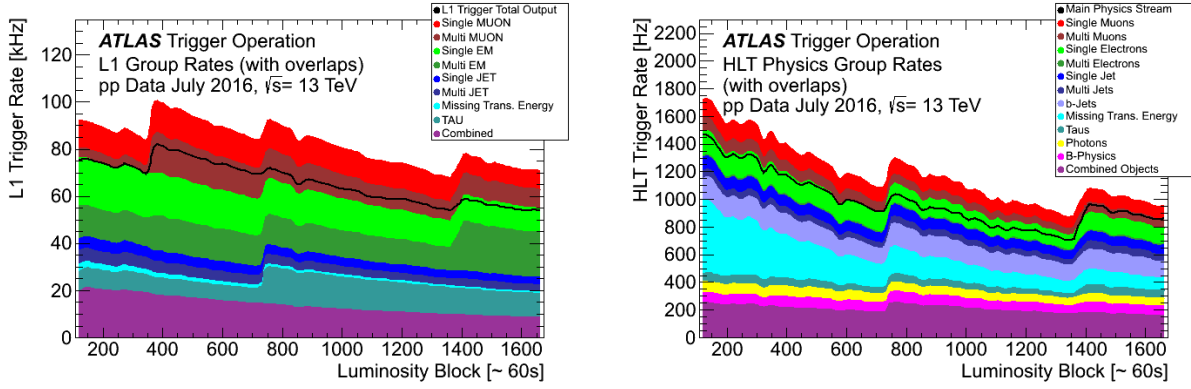


Figure 2.11: *L1* (left) and HLT trigger rates grouped by trigger as a function of the number of luminosity blocks (a luminosity block is a time interval during which the delivered instantaneous luminosity is constant) recorded in July 2016. Black lines show the *L1* total rate (left) and HLT main physics stream rate (right). From [22].

⁵It is useful to keep in mind that bunch crossing happens every 25 ns: this corresponds to a bunch crossing rate of 40 MHz.

CHAPTER 3

Reconstruction of electrons and photons with the ATLAS detector

The reconstruction of electrons and photons ([5], [7], [17]) is based on the reconstruction of *tracks* in the Inner Detector and on the *clusters* of energy deposit in the EM calorimeter. The electromagnetic showers originating from the interaction of electrons or photons with the EM calorimeter are essentially indistinguishable: therefore, the reconstruction of electrons and photons with the ATLAS detector proceeds parallelly, in order to distinguish between *electrons*, *unconverted photons*, and *converted photons*¹. This chapter is devoted to showing how electrons and photons are reconstructed with the ATLAS detector.

Energy clusters in the EM calorimeter

The reconstruction of both electrons and photons in the ATLAS detector begins with searching *seed clusters* of EM calorimeter cells.

The initial step is the creation of a preliminary set of seed clusters: this operation is performed by a *sliding-window algorithm* ([15], [17]) in three steps:

- **Tower building.** The EM calorimeter is segmented in $\eta - \phi$ directions into a grid of $N_\eta \times N_\phi$ *towers* of size $\Delta\eta^{tower} \times \Delta\phi^{tower} = 0.025 \times 0.025$, i.e. the same size of the cells in the second layer of the EM calorimeter. Each tower incorporates several cells from the three layers of the EM calorimeter. The *tower energy* is the sum of the energy deposits in all the cells falling within a tower. If a cell spans different towers (or, to put it in another way, only part of a cell falls within a tower) the energy is distributed between the towers according to the fractional areas of the cell incorporated by the towers.
- **Seed cluster finding.** A window of fixed size $N_\eta^{window} \times N_\phi^{window} = 3 \times 5$ in units of $\Delta\eta^{tower} \times \Delta\phi^{tower}$ is moved across each element of the tower grid in steps of $\Delta\eta^{tower}$ and $\Delta\phi^{tower}$. The energy of the window, defined as the sum of the transverse energies of the 15 towers contained in the window, is measured: the 3×5 areas where the energy of the window reaches a local maximum are identified as the seed clusters, provided that the maxima are above a threshold of 2.5 GeV. The (η, ϕ) position of the seed cluster is computed as the energy-weighted η and ϕ barycenters of all cells within a 3×3 window around the tower at the center of the sliding window.
- **Cluster filling.** A cluster is then built around the seed position in every layer, incorporating cells within a rectangle of size $N_\eta^{cluster} \times N_\phi^{cluster} = 3 \times 7$ (5×5) in the barrel (end-caps). The order in which the layers are processed is the following. At first, a cluster in the L2 layer is built around the seed cluster position $(\eta_{seed}, \phi_{seed})$. A new barycenter using only the energy deposits in L2 is then computed: this position (η_{L2}, ϕ_{L2}) is used as seed position for creating the cluster in L1 and L3. The cluster in the PreSampler is created around the barycenter (η_{L1}, ϕ_{L1}) of energy deposits in the layer L1.

¹The difference between unconverted and converted photons is that converted photons decay into electron-positron pair before reaching the EM calorimeter, e.g. in the Inner Detector.

Track reconstruction and matching

After building an energy cluster in the EM calorimeter, the reconstructions of electrons and photons (either converted and unconverted) proceeds to the second step: searching for a track in the Inner Detector to match the energy clusters. Of course unconverted photons do not leave tracks in the detector: therefore, if the candidate particle is an unconverted photon, and if the object is reconstructed correctly, the search will yield no findings.

Once a track is reconstructed, a region of interest around the position of seed clusters is defined: every point in this region has an angular distance from the seed cluster position in L2 of 0.05 in the η direction, and of either 0.2 (0.1 for tracks reconstructed from hits only in the TRT) along ϕ in the direction of the bending of the track or 0.05 in the opposite direction. The considered track is then extrapolated to find its intersection point with the L2 layer: the track is *loosely matched* to an energy cluster in the EM calorimeter if its intersection point with L2 falls within the region of interest built around that seed cluster. If a track has a significant number of hits (≥ 4) and it is loosely matched to an energy cluster, it is refitted using the Gaussian Sum Filter (GSF) algorithm, which allows an optimized track reconstruction, especially for low- p_T electrons, which may have suffered from significant energy losses from bremsstrahlung. A second matching process is then applied to the re-fitted tracks: the criteria are similar, except for a stricter condition on the distance of the track from the seed cluster along ϕ , which is required to be smaller than 0.1 in the direction of the bending of the track.

If more than one track meets the matching criteria, the track with the smallest angular distance between the extrapolated intersection point on L2 and the seed cluster is selected, unless the angular distances associated with the candidate tracks differ of less than 0.01. In this case, an algorithm chooses the best track, preferring those with more hits and those with hits in the first silicon layer of the Inner Detector.

3.1 Electrons

3.1.1 Reconstruction

Energy clusters in the EM calorimeter with a matching track are considered to be electron candidates. After finding an electron candidate, its energy cluster is rebuilt using cells with areas of 3×7 (5×5) in units of $\Delta\eta^{tower} \times \Delta\phi^{tower}$ in the barrel (end-caps) of the EM calorimeter, as explained before. Finally, the four-momentum of the electron candidate is computed. The energy of the electron candidate is the energy in the final cluster; if the track has hits in the inner layers of the Inner Detector, η and ϕ of the electron candidate are inferred from the corresponding parameters of the track, while if the track is reconstructed only from hits in the TRT η and ϕ coincide with the position of the barycenter of the final cluster.

A further step is necessary to discriminate electrons from converted photons and other particles originating from secondary vertices. The track of the candidate electron is required to be compatible with the primary interaction vertex. The track parameters involved in these requirements are d_0 and z_0 : d_0 is the *transverse impact parameter*, and it is defined as the distance of closest approach of the track to the z-axis (i.e. the beamline); z_0 , the *longitudinal impact parameter*, is the z coordinate of the closest point of approach of the track to the z-axis. To be reconstructed as an electron, the candidate particle needs to pass the requirements $d_0/\sigma_{d_0} < 5$, where σ_{d_0} is the uncertainty on d_0 and $\Delta z_0 \sin \theta < 0.5$ mm, where Δz_0 is the absolute difference of z_0 for the track and z_0 for the primary vertex and θ is the polar angle.

Table 3.1: List and description of the variables used by the likelihood-based identification algorithm to assign the identification working point to candidate electrons. From [5].

Type	Description	Name
Hadronic leakage	Ratio of E_T in the first layer of the hadronic calorimeter to the E_T of the energy cluster in the EM calorimeter (used for a pseudorapidity range of $ \eta < 0.8 \wedge \eta > 1.37$).	R_{had1}
	Ratio of E_T in the hadronic calorimeter to the E_T of the energy cluster in the EM calorimeter (used for a pseudorapidity range of $0.8 < \eta < 1.37$).	R_{had}
L3 of the EM calorimeter	Ratio of the energy in the back layer to the total energy in the EM calorimeter. This variable is only used below 100 GeV because it is known to be inefficient at high energies.	f_3
L2 of the EM calorimeter	Shower width, $\sqrt{(\sum E_i \eta_i^2) / (\sum E_i)} - ((\sum E_i \eta_i) / (\sum E_i))^2$, where E_i is the energy and η_i is the pseudorapidity of cell i and the sum is calculated within a window of 3×5 cells.	w_{η^2}
	Ratio of the energy in 3×3 cells to the energy in 3×7	R_ϕ
	Ratio of the energy in 3×7 cells to the energy in 7×7	R_η
L1 of the EM calorimeter	Shower width, $\sqrt{(\sum E_i (i - i_{max})^2) / (\sum E_i)}$ where i runs over all strips in a window $\Delta\eta \times \Delta\phi \approx 0.0625 \times 0.2$, corresponding typically to 20 strips in η , and i_{max} is the index of the highest-energy strip.	w_{stot}
	Ratio of the energy difference between the largest and second largest energy deposits in the cluster over the sum of these energies.	E_{ratio}
	Ratio of the energy in the strip layer to the total energy in the EM accordion calorimeter.	f_1
Track condition	Number of hits in the innermost pixel layer; discriminates against photon conversion.	n_{Blayer}
	Number of hits in the pixel detector.	n_{Pixel}
	Number of total hits in the pixel and SCT detectors.	n_{Si}
	Transverse impact parameter with respect to the beamline.	d_0
	Significance of transverse impact parameter defined as the ratio of d_0 and its uncertainty.	$\frac{d_0}{\sigma_{d_0}}$
	Momentum lost by the track between the perigee and the last measurement point divided by the original momentum.	$\frac{\Delta p}{p}$
TRT	Likelihood probability based on transition radiation in the TRT.	eProbabilityHT
Track-cluster matching	$\Delta\eta$ between the cluster position in L1 and the extrapolated track.	$\Delta\eta_1$
	$\Delta\phi$ between the cluster position in L2 and the track extrapolated from the perigee.	$\Delta\phi_2$
	Defined as $\Delta\phi_2$, but the track momentum is rescaled to the cluster energy before extrapolating the track from the perigee to the L2 of the calorimeter.	$\Delta\phi_{res}$
	Ratio of the cluster energy to the track momentum.	E/p

3.1.2 Identification

In order to distinguish electrons originated from the hard interaction (*prompt electrons*) and the background electrons reconstructed from hadron decays, an algorithm for electron identification is applied. For Run2 a likelihood-based identification algorithm is used, with three different operating points provided: *Loose*, *Medium*, and *Tight*. These working points are defined in such a way that a sample of electrons of tight quality is a subset of a sample of medium electron, which, in turn, is a subset of a sample of loose electrons. These three identification working points - from *Loose* to *Tight* - have an increasing power of rejecting the background (electrons originated from hadron decays or wrongly reconstructed converted photons) from signal objects (prompt electrons from the primary vertex). The discriminating variables used to define the working points, listed in Table 3.1, are the same for *Loose*, *Medium*, and *Tight*, but the requirements on these variables are different. To define a working point, information on both the reconstructed electron energy cluster and the matching track are employed.

3.1.3 Isolation

To further discriminate between signal and background electrons, the reconstructed electrons are required to satisfy isolation criteria. To quantify the isolation of reconstructed electrons two variables are employed:

- $E_T^{\text{cone}0.2}$ measures the **calorimetric isolation energy**. The idea is to consider the energy deposits in the EM calorimeter which are close to the energy cluster of the candidate electron; if the measured energy is below a certain threshold whose value depends from the electron's transverse momentum, the electron is considered calorimetrically isolated. $E_T^{\text{cone}0.2}$ is defined as the sum of the positive transverse energies of topological clusters² within a cone of radius $\Delta R = \sqrt{(\Delta\eta)^2 + (\Delta\phi)^2} = 0.2$ around the energy cluster of the candidate electron. The transverse energy of a rectangular cell of size 5×7 (in units of $\Delta\eta^{\text{tower}} \times \Delta\phi^{\text{tower}}$) is then subtracted from the previously computed value to exclude from $E_T^{\text{cone}0.2}$ the energy of the electron itself; a correction depending from E_T and η of the candidate electron is applied, to account for electron energy leakage outside the considered rectangle. The isolation energy value is also corrected to remove contributions from pile-up and underlying events³. A visualization of $E_T^{\text{cone}0.2}$ is provided in Fig. 3.1. Variables $E_T^{\text{cone}0.3}$ and $E_T^{\text{cone}0.4}$ are defined similarly.
- $p_T^{\text{varcone}0.2}$ quantifies the **track isolation**. $p_T^{\text{varcone}0.2}$ is the sum of the transverse momenta of all tracks falling within a cone of radius ΔR around the primary electron track and originating from the primary vertex. The radius of the cone is 0.2 if the transverse energy of the candidate electron is smaller than 50 GeV, while $\Delta R = 10 \text{ GeV} / E_T$ if $E_T > 50 \text{ GeV}$. The tracks associated with the electron are excluded from the sum. Finally, the tracks included in the sum need to meet some "quality" criteria (see [5]).

A variety of standardized isolation working points are defined by selection requirements on the variables presented above. The selection requirements depend on the transverse momentum of the electron, i.e. the established cuts are to be applied on $p_T^{\text{varcone}0.2}/p_T$ and $E_T^{\text{cone}0.2}/p_T$. The cut values vary with η and p_T of the electron if the isolation working point is defined to meet a determined efficiency on isolated electrons. Working points requiring fixed upper threshold are also defined.

²A topological cluster (*topo-cluster*) is a set of cells with energy deposits $E_{\text{cell}}^{\text{EM}}$ larger than the expected noise $\sigma_{\text{noise}}^{\text{EM}}$. Building a topo-cluster follows the idea described below. The seed cluster is a cell with $\zeta_{\text{cell}}^{\text{EM}} = \frac{E_{\text{cell}}^{\text{EM}}}{\sigma_{\text{noise}}^{\text{EM}}} \geq 4$. After finding a seed cluster, the topological cluster is built around the seed cluster by collecting all the neighbour cells with $\zeta_{\text{cell}}^{\text{EM}} \geq 2$. For the third and final step, the neighbouring cells with $\zeta_{\text{cell}}^{\text{EM}} \geq 0$ are added to the topo-cluster.

³An underlying event is an event originating from hadrons interactions not involved in the hard process

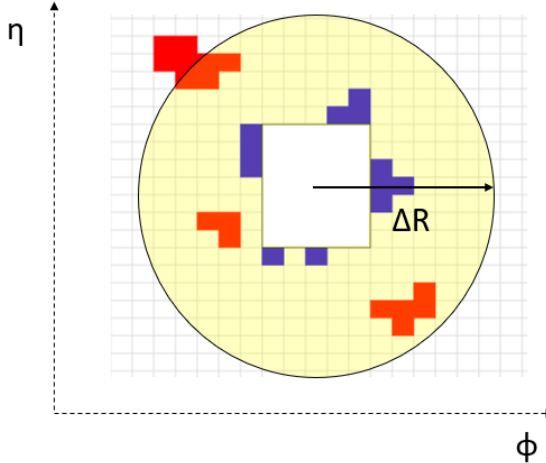


Figure 3.1: Section of the cone of radius ΔR (yellow) around the energy cluster associated to the electron. The white rectangle represents the electron's cluster energy, excluded from the calculation of the variable E_T^{cone} , while the blue cells represent the corrections for energy leakage. The red cells highlight the topo-clusters found in the cone, whose energy adds up to yield E_T^{cone} .

3.2 Photons

3.2.1 Reconstruction

The reconstruction of photon candidates is similar to the procedure followed for the reconstruction of electrons, with some additional steps required to successfully discriminate between electrons and photons. To be precise, the discrimination between electrons and photons happens at the end of the reconstruction procedure: an energy cluster in the EM calorimeter can be reconstructed either as an electron or as a photon or as both, depending on a set of requirements on track reconstruction, track matching and identification of vertices.

Once seed clusters are reconstructed, the following step consists in finding tracks consistent with originating from a candidate conversion vertex (if there is one), i.e. a secondary vertex where the candidate (converted) photon decayed into an electron-positron pair. The reconstructed secondary vertex can be a **double-track vertex** or a **single-track vertex**. Double-track vertex candidates are reconstructed from pairs of oppositely charged tracks in the Inner Detector that are likely to be electrons. The requirement on the likelihood to be an electron is based on the variable eProbabilityHT used for electron identification, and changes whether the considered track has hits on the silicon detector⁴. The tracks originating from a photon conversion are parallel at the place of conversion: therefore, track pairs need to fulfill a series of geometric requirements in order to be retained. The established geometric requirements are based on the angles between the two tracks at the point of the tracks' closest approach to the candidate double-track vertex, on the closest distance between the tracks, and finally on parameters of the helices constructed from the two tracks. The geometric criteria change whether both tracks (Si-Si), none (TRT-TRT), or only one track (Si-TRT) have hits in the silicon detector. After the selection described above, the retained tracks are fitted in order to retrieve the final double-track vertex candidate: only fitted vertices satisfying "quality" criteria are retained. The efficiency of reconstruction of double-track vertex candidates drops for conversions taking place in the outer layers of the Inner Detector: the TRT has a poorer resolution compared to the silicon detector, therefore softer tracks are more easily missed and a pair can be reconstructed as a single track if the two tracks are very close to each other. These two issues are relevant for asymmetric photon conversions, where one of the

⁴If a track has hits in the silicon detector (i.e. the inner layers of the Inner Detector, see Chapter 2) the requirements on the likelihood are looser, because the hits close to the interaction points hint that the candidate particle is indeed a signal electron.

electrons carries away most of the energy, and for high-energy photons respectively. To face this efficiency drop, it was proven necessary to include the possibility of reconstructing a single-track conversion vertex. The tracks of candidate electrons with no hits on the pixel detector and with either a strong likelihood to be electrons or no hits in the TRT are considered tracks of converted photons, where the second track was missed or unresolved. The single-track vertices associated with these tracks can't be reconstructed from a fit, therefore their position is made to coincide with the first measurements of their track.

The final step consists in matching a conversion vertex, if found, to energy clusters in the EM calorimeter. The conversion vertex candidate is extrapolated to the second layer of the EM calorimeter, and its extrapolated angular position ($\eta_{vertex}, \phi_{vertex}$) is compared with the barycenter ($\eta_{cluster}, \phi_{cluster}$) of the energy cluster.

- If the conversion vertex is built from track(s) with hits on the silicon detector, it is considered to be matched to an energy cluster if their distance in both the η and ϕ directions is smaller than 0.05. If the conversion vertex is a single-track vertex, the accepted distance in the ϕ coordinate increases to 0.1 in the direction of the bending of the track.
- If the conversion vertex is built from track(s) without hits in the silicon detector (but with hits only in the TRT), the matching requirements are $\Delta\phi < 0.02$ (0.03) in the direction of (opposite to) the bending of the track(s) and $\Delta\eta < 0.35$ (0.2) in the barrel (end-caps) of the TRT. $\Delta\phi$ and $\Delta\eta$ are the angular distances between the extrapolated position of the reconstructed track(s) on L2 and the position of the energy cluster.

After matching conversion vertices to energy cluster in the EM calorimeter, the final arbitration (summarized in Fig. 3.2) between reconstructing a candidate particle as an electron or as a photon is performed [17]:

- **Unconverted photon.** An energy cluster with no matching tracks nor conversion vertex is reconstructed as an unconverted photon.
- **Converted photon.** A cluster with a matching track with less than four hits in the silicon detector is classified as a photon. If a track associated with an energy cluster has no hits in the pixel detector and is part of a double-track vertex located in the silicon detector, the candidate particle is reconstructed as a photon.
- **Electron.** A cluster with a matching track with at least two hits in the pixel detector and four hits in the silicon detector and no matching conversion vertices is reconstructed as an electron. If the track is part of a conversion vertex, the particle is reconstructed as an electron either if the vertex is not a double-track vertex located in the silicon detector or, if this is the case, if only one of the tracks associated with the vertex has hits in the innermost layer of the pixel detector.
- A candidate particle is reconstructed **both as an electron and as a photon** if it does not fulfill any of the requirements listed above, or if the ratio of the energy of the cluster to the momentum of the matching track is above 10 or if p_T from the track is smaller than 2 GeV.

Electrons reconstructed as photons

As already mentioned before, electromagnetic showers left in the EM calorimeter by electrons and photons are identical. Furthermore, while electrons are identified by a single track originating from the primary vertex of interaction pointing to a energy cluster, the same signature can be left by photons converting early in the detector with a single-track conversion vertex. Although the reconstruction algorithm for electrons and photon is designed to minimize the misreconstruction (and subsequent misidentification) of electrons as photons (and vice-versa), a small fraction of electrons faking photons can result from the reconstruction procedure. This is primarily due to

detector mistakes or imperfections, e.g. broken modules in the Inner Detector, which can result in bad track reconstruction or bad matching of tracks with their energy clusters. Bad reconstruction of energy cluster in the EM calorimeter is rarer: the efficiency of reconstruction of energy clusters approaches 100% (see Table 6 in [15]). As an example, let's consider an electron whose path in the Inner Detector passes through a dead module in the pixel detector: this would result in a candidate electron track with no hits in the pixel detector. This would result in a reconstruction of a candidate single-track vertex from the first measurements of the electron track. The vertex may then be matched with the energy cluster left by the electron in the EM calorimeter, resulting in a mis-reconstruction of a converted photon with a single-track vertex.

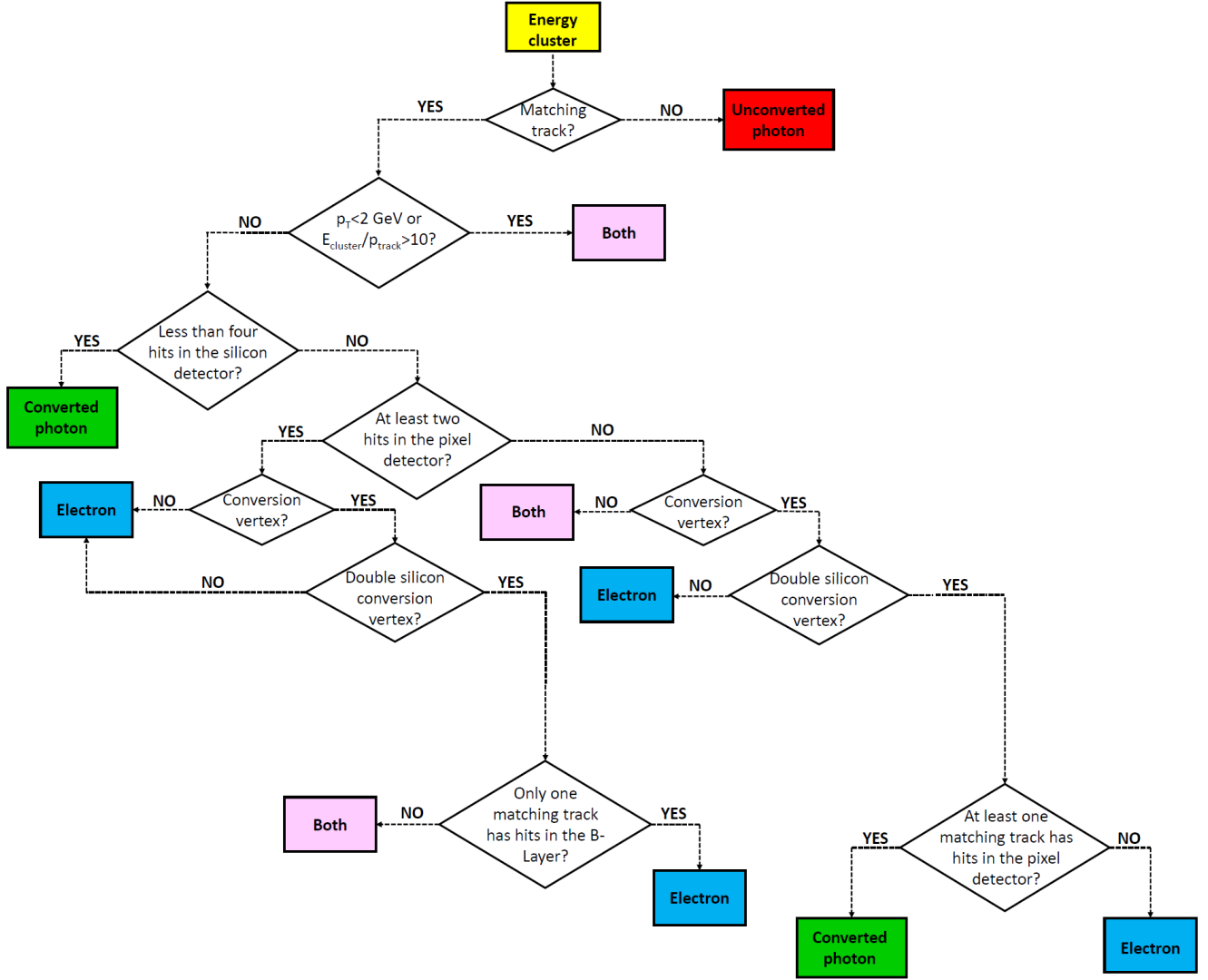


Figure 3.2: Graphical representation of the final arbitration on reconstructing a candidate particle as an electron or as a photon.

Table 3.2: List and description of the variables used by the cut-based identification algorithm to assign the identification working point to candidate photons. Variables employed to define the Loose and Tight identification working points are highlighted. From [7].

Type	Description	Name	Loose	Tight
Acceptance	$ \eta < 2.37$, with $1.37 < \eta < 1.52$ excluded.	-	•	•
Hadronic leakage	Ratio of E_T in the first layer of the hadronic calorimeter to the E_T of the energy cluster in the EM calorimeter (used for a pseudorapidity range of $ \eta < 0.8 \wedge \eta > 1.37$).	R_{had1}	•	•
	Ratio of E_T in the hadronic calorimeter to the E_T of the energy cluster in the EM calorimeter (used for a pseudorapidity range of $0.8 < \eta < 1.37$).	R_{had}	•	•
L2 of the EM calorimeter	Ratio of the energy in 3×7 cells to the energy in 7×7 .	R_η	•	•
	Lateral shower width, $\sqrt{(\sum E_i \eta_i^2) / (\sum E_i)} - ((\sum E_i \eta_i) / (\sum E_i))^2$, where E_i is the energy and η_i is the pseudorapidity of cell i and the sum is calculated within a window of 3×5 cells.	w_{η^2}	•	•
	Ratio of the energy in 3×3 cells to the energy in 3×7 .	R_ϕ		•
L1 of the EM calorimeter	Lateral shower width, $\sqrt{(\sum E_i (i - i_{max})^2) / (\sum E_i)}$, where i runs over all strips in a window of 3×2 strips and i_{max} is the index of the highest-energy strip calculated from three strips around the strip with maximum energy deposit.	w_{ss3}		•
	Total lateral shower width, $\sqrt{(\sum E_i (i - i_{max})^2) / (\sum E_i)}$, where i runs over all strips in a window of 20×2 strips and i_{max} is the index of the highest-energy strip measured in L1.	w_{stot}		•
	Energy outside the core of the three central strips but within seven strips divided by energy within the three central strips.	f_{side}		•
	Difference between the energy associated with the second maximum in L1 and the energy reconstructed in the strip with the minimum value found between the first and second maxima.	ΔE_s		•
	Ratio of the energy difference between the maximum energy deposit and the energy deposit in the secondary maximum in the cluster to the sum of these energies.	E_{ratio}		•
	Ratio of the energy in L1 to the total energy of the EM cluster.	f_1		•

3.2.2 Identification

Photon identification allows to discriminate between *prompt photons*, i.e. photons not originating from the decays of hadrons, and *background photons*: this process is important because prompt photons show up in many interesting physics processes, one for all the signature $DM + \gamma$ covered by the Mono-Photon Analysis (see Chapter 4). Distinctive features of prompt photons are a narrower energy deposit in the EM calorimeter and a smaller leakage to the hadronic calorimeter, compared with background photons originating from hadronic jets. In addition, isolated $\pi^0 \rightarrow \gamma\gamma$ decays result into two separate local energy maxima in the first layer calorimeter, whose fine segmentation is useful to distinguish between these photon pairs originating from π^0 decays and prompt photons. The set of variables, listed in Table 3.2, defined for the photon identification is designed to take into account the features mentioned above: it includes variables describing the development of the showers in the EM calorimeter and the shower leakage in the hadronic calorimeter.

Two identification working points are established for photons:

- The *Loose* identification working point is designed to maximize the prompt photon efficiency with respect to photon reconstruction. The selection for identifying a loose photon relies only to variables describing shower shapes in L2 and energy deposits in the hadronic calorimeter.
- The *Tight* identification working points, in addition to the variables already considered in defining the Loose identification working point, requires a selection on variables describing shower shapes on the L1 layer of the EM calorimeter. The criteria for a Tight photon depend on whether the photon is converted or unconverted.

3.2.3 Isolation

Requiring isolation criteria for the prompt photon candidates allows a further rejection of background photons from high-energy π^0 ($\rightarrow \gamma\gamma$) decays. Photon isolation criteria are based on the two variables E_T^{iso} and p_T^{iso} referring to **calorimeter isolation** and **track isolation** respectively. These variables are defined similarly to the isolation variables for electrons.

E_T^{iso} is the sum of transverse energies in topological clusters in the EM calorimeter and in the hadronic calorimeter within a cone of radius $\Delta R = 0.4$ (or 0.2 or 0.3) around the photon candidate. The contribution of the energy of the photon itself is excluded from the sum (subtracting a rectangle of 5×7 cells from the center of the cone) and corrections for photon energy leakage outside the rectangle and for pile-up are applied. p_T^{iso} is computed as the sum of transverse momenta larger than 1 GeV associated with tracks within a cone of radius $\Delta R = 0.2$ (or 0.3 or 0.4) centered on the photon direction. The transverse momenta of the tracks associated with the photon conversion are excluded from the sum, while those included are required to have a point-of-closest-approach distance with the primary vertex $\Delta z_0 \sin \theta < 3$ mm to minimize pile-up.

Isolation working points for photons are defined by fixed cuts on variables E_T^{iso}/p_T and p_T^{iso}/p_T : there are no efficiency-based operating points.

CHAPTER 4

The Mono-Photon analysis

The work presented in this thesis consisted in providing a new evaluation of the background from electrons faking photons for the Mono-Photon analysis. The Mono-Photon analysis is part of the mono-X searches described in Section 1.3.3: the SM physics object used to tag the event with a large value of missing transverse momentum E_T^{miss} is a photon.

The Mono-Photon analysis is characterized by a relatively clean final state, containing a photon with a high transverse momentum and a large E_T^{miss} , which can be mimicked by only a few SM processes. An excess in the selected events with respect to SM predictions carrying the same signature in their final state would be a striking evidence of physics beyond the SM. The observation of a significant discrepancy with the background due to SM processes could mean that the signature $E_T^{miss} + \gamma$ in the ATLAS detector is the result of production of $DM + \gamma$ events in a pp collision at LHC.

The Mono-Photon signature $E_T^{miss} + \gamma$ is predicted by multiple theories of physics beyond the SM (BSM): the Mono-Photon analysis focuses on a Simplified DM model (see Section 1.2) with five free parameters, i.e. the mass of the DM particle m_χ , the mass of the mediator through which χ interacts with quarks m_{med} , the width of the mediator Γ_{med} , and the couplings of the mediator to quarks (g_q) and to the DM particle (g_χ).

The main challenge faced by the Mono-Photon analysis is the discrimination between signal, i.e new physics resulting in a Mono-Photon final state, and SM background. The dominant background source is the production of $Z + \gamma$ events, where Z decays to a neutrino and an anti-neutrino. $Z \rightarrow \nu\nu + \gamma$ events constitute approximately 60% of the total background and provide the only irreducible background for the Mono-Photon final state: their signature in the detector is indistinguishable from the signal's.

The Mono-Photon analysis described in this chapter was performed in 2016 with Run2 events, collected in 2015 and 2016 at a center-of-mass energy $\sqrt{s} = 13$ TeV.

4.1 Event selection

The event selection is driven by the effort of achieving a high significance of the expected signal over the predicted SM background.

4.1.1 Pre-selection of events

The pre-selection of events is applied before the final selection and it is common to all the regions defined in the analysis. The pre-selection criteria are common to many ATLAS physics analysis: they are designed to discriminate interesting events from all sorts of instrumental and experimental noise. The pre-selection requirements are listed below:

- The events must be in the *Good Run List* (GDR)¹
- The events must pass a requirement at the HLT level, called `HLT g140 loose`².
- The reconstructed primary vertex must be associated to at least two good quality tracks.

¹Events are listed in the GRL if they were collected when LHC and every ATLAS sub-detector worked at their best functionality. Being in the GRL is an indicator of the quality of the event.

²This trigger selects events with at least one photon candidate with $p_T > 140$ GeV and satisfying the loose identification criteria.

- Events containing jets either with $p_T > 20$ GeV, or overlapping with photons or electrons, or flagged as *LooseBad*, are rejected. A jet is flagged *LooseBad* if it is likely to be a fake jet, e.g. reconstructed from a noise burst in the detector or from a deposit of energy by cosmic rays.

4.1.2 Selection of physics objects

The event selection employs a discrimination of the physics objects (photons, electrons, muons, jets, and missing transverse momentum) into *preselected* and *selected* objects.

Photons

All the reconstructed photons of loose quality (see Section 3.2.2) with $E_T > 10$ GeV and $|\eta| < 2.37$ are considered preselected photons. A selected photon, in addition to the requirements for a preselected photon, needs to be isolated (see Section 3.2.3): the required isolation working point is "FixedCutTight".

Electrons

A preselected electron is a reconstructed electron with medium quality (see Section 3.1.2), $E_T > 7$ GeV and $|\eta| < 2.47$. Furthermore, a preselected electron needs to satisfy two conditions on the longitudinal and transverse impact parameters - z_0 and d_0 - of tracks with respect to the primary vertex: these cuts allow to choose electrons whose track is compatible with the primary vertex. In particular, $|d_0|/\sigma_{d_0} < 5$ and $|z_0|\sin\theta < 0.5$ mm. On the other hand, a selected electron is a preselected electron with the additional request to be selected by the "loose" isolation working point (see Section 3.1.3 and 5.1.1).

Muons

The criteria for pre-selected muons are similar to the ones for pre-selected electrons. Pre-selected muons have medium quality, are required to have $p_T > 6$ GeV, $|\eta| < 2.7$, $|d_0|/\sigma_{d_0} < 3$, and $|z_0|\sin\theta < 0.5$ mm. A selected muon needs to satisfy the additional requirement to be isolated.

Jets

Preselected jets are reconstructed jets with $p_T > 20$ GeV. Selected jets must have $p_T > 30$ GeV, $|\eta| < 4.5$, and finally $JVT > 0.59$ for jets with $30 \text{ GeV} < p_T < 60 \text{ GeV}$ and $|\eta| < 2.4$. The cut on the Jet Vertex Tagger variable JVT is to remove jets originating from pile-up.

As already mentioned, the reconstruction of objects in the ATLAS detector is not always a smooth process: a single candidate particle can be reconstructed as two different objects. To partially resolve these ambiguities, an algorithm of overlap removal is applied to the preselected objects.

4.1.3 Event selection in the Signal Region

After passing the pre-selection criteria, an event needs to meet further requirements to be in the **Signal Region (SR)**, where events with final states with a real $DM + \gamma$ signature are expected. The Mono-Photon analysis employs three different SRs, for three different thresholds for the quantity E_T^{miss} . E_T^{miss} is a discriminant variable for the Mono-Photon analysis and it is calculated as the vectorial negative sum of the energies of the calibrated reconstructed physics objects, plus the terms coming from energy deposits and tracks not matched to reconstructed physics objects. The considered E_T^{miss} bins are:

1. $E_T^{miss} > 150$ GeV;

2. $E_T^{miss} > 225$ GeV;
3. $E_T^{miss} > 300$ GeV.

The events in the SR are selected to meet the following requirements:

- E_T^{miss} needs to meet its threshold requirements, depending on the chosen E_T^{miss} bin.
- The event must contain at least one preselected photon with $p_T > 150$ GeV and $|\eta| < 1.37 \vee |\eta| > 1.52$, to exclude the crack region of the EM calorimeter.
- The significance of the E_T^{miss} quantity must be above $8.5 \text{ GeV}^{1/2}$. The significance is defined as the ratio of E_T^{miss} to its resolution $\sigma(E_T^{miss})$; this requirement significantly reduces the $\gamma + \text{jet}$ background (see Section 2). The E_T^{miss} significance is defined as the ratio of E_T^{miss} to the quantity $\sum E_T$, defined as the sum of the transverse momenta of all objects contributing to the reconstruction of E_T^{miss} .
- The leading photon must be tight and satisfy the "FixedCutTight" isolation criteria (see Sections 3.2.2 and 3.2.3). In addition, the leading photon must not overlap with E_T^{miss} : $\Delta\phi(\gamma, E_T^{miss}) > 0.4$.
- The z coordinate pointed by the leading photon must be lower than 250 mm with respect to the primary vertex (*photon pointing*).
- Events with at most one selected jet are retained; if there is a jet, it must not overlap with E_T^{miss} : $\Delta\phi(E_T^{miss}, \text{jet}) > 0.4$. This requirement is called *jet veto*.
- A *lepton veto* requirement is established: events with any preselected electrons or muons are discarded.

4.2 Background estimation

The main background sources for the Mono-Photon analysis are listed below:

- $Z(\rightarrow \nu\nu) + \gamma$ is the major background source and it provides the only irreducible background, as anticipated at the beginning of this Chapter.
- $W(\rightarrow l\nu) + \gamma$ where the lepton is either not reconstructed (or reconstructed as a photon if it is an electron) or, if it is a τ lepton, decays leptonically and it is missed or it is reconstructed as a jet.
- $Z(\rightarrow ll) + \gamma$ where both the leptons are missed.
- $Z(\rightarrow \nu\nu) + \text{jet}$ and $Z(\rightarrow ll) + \text{jet}$, where the leptons from Z behave as described in the previous point and the jet is reconstructed as a photon.
- $W(\rightarrow l\nu) + \text{jet}$ where the lepton behaves as described in the first point and the jet is reconstructed as a photon.
- $t\bar{t}$, single t or diboson: these background sources are similar to the $W + \text{jet}$ backgrounds.
- $\text{jet} + \gamma$, where the jet mimics a large E_T^{miss} as a result of miscalibration or misreconstruction.

The use of Monte-Carlo (MC) simulations is crucial to calculate the background estimation for the Mono-Photon analysis. The prediction on the number of background events provided by MC simulations is then normalized with a data-to-simulation ratio determined primarily in **Control Regions (CR)**, i.e. regions where no signal is expected. This process involves fitting the MC

simulations to the CRs (and the Signal Region SR) data: the fit allows to obtain the nominal value of the MC predictions (*normalization*), together with systematic uncertainties on these predictions (*nuisance parameters*). This method is only applicable, however, for real- γ background sources (events forming real- γ backgrounds have a true photon in their final state). As for fake- γ background sources, characterized by another physics object being mistakenly reconstructed as a photon, a purely in-situ technique is to be employed to estimate the background yields. The fake- γ background sources for the Mono-Photon analysis are from electrons faking photons in $W(\rightarrow e\nu) + \gamma$ and $W(\rightarrow e\nu) + \text{jet}$ events and jets faking photons.

4.2.1 Definition of Control Regions

To evaluate the main background contributions, four Control Regions (CRs) are established. The idea behind such CRs is to build data regions kinematically close to the SR, but orthogonal to it: ideally, the control regions are signal-free. The CRs are defined by reverting one or more selection criteria of the SR, such that they are dominated by a single background process, as shown in Fig. 4.1. The four CRs are listed below:

One-Muon Control Region (1 μ CR). This CR is enriched in $W(\rightarrow \mu\nu) + \gamma$ events. The E_T^{miss} value is artificially varied, adding to it the muonic contribution to the transverse momentum. The same selection of the SR is applied except for the lepton veto: a single selected muon must be present in each selected event. The normalization factor k_W for $W + \gamma$ backgrounds is primarily retrieved from this CR.

Two-Muon (Electron) Control Region (2 μ (2e) CR). In this case, the CRs are enriched in $Z(\rightarrow \mu\mu) + \gamma$ and $Z(\rightarrow ee) + \gamma$ events respectively. The muonic (electronic) term is subtracted from the real E_T^{miss} , i.e. muons (electrons) are treated as invisible particles. This allows the kinematics of $Z \rightarrow ll$ processes to mimic those of $Z \rightarrow \nu\nu$: this strategy is used by the Mono-Photon analysis to correctly estimate the irreducible $Z \rightarrow \nu\nu + \gamma$ background contribution. To define the 2 μ CR (2e CR) the same cuts of the SR are applied, except that two selected muons (electrons) are present in the events and no preselected electron (muon). In addition, the invariant mass of the muon couple (electron couple) must be larger than 10 GeV. These two CRs are used for finding the scale factor k_Z for $Z + \gamma$ backgrounds.

Photon-Jet Control Region (PhJet CR). The SM background process jet+ γ is dominant in this region. The PhJet CR is defined by the same selection of the SR, except for a lower threshold for E_T^{miss} and a definition for an upper value of the same quantity: 85 GeV $< E_T^{\text{miss}} <$ 110 GeV. To avoid a possible contamination of signal events, i.e. carrying a true $\gamma + \text{DM}$ signature, the additional request $\Delta\phi(\gamma, E_T^{\text{miss}}) < 3.0$ is applied. The normalization factor k_{jet} for jet + γ backgrounds is primarily retrieved from fitting in this CR.

4.2.2 The simultaneous fit technique

MC simulations of events constituting real- γ background for the Mono-Photon analysis are carried out; the simulations are then fitted simultaneously to the SR and to the CRs. The fitted background yields in each region are given by the expected (from MC) number of background events in the considered region multiplied by a normalization factor k , depending exclusively from the considered background process (e.g. $Z + \gamma$). The normalization factors for each background source are the same in every region of the analysis, while the background yields are, of course, not. The normalization factors are free parameters of the fit, while the expected number of background events in every region is a fixed parameter, i.e. its value is only allowed to fluctuate from the nominal MC prediction within the constraints of the nuisance parameters. The normalization factors - rescaling the number of events from various background sources expected from MC simulations - are not extracted from fitting exclusively to the region where the considered background source

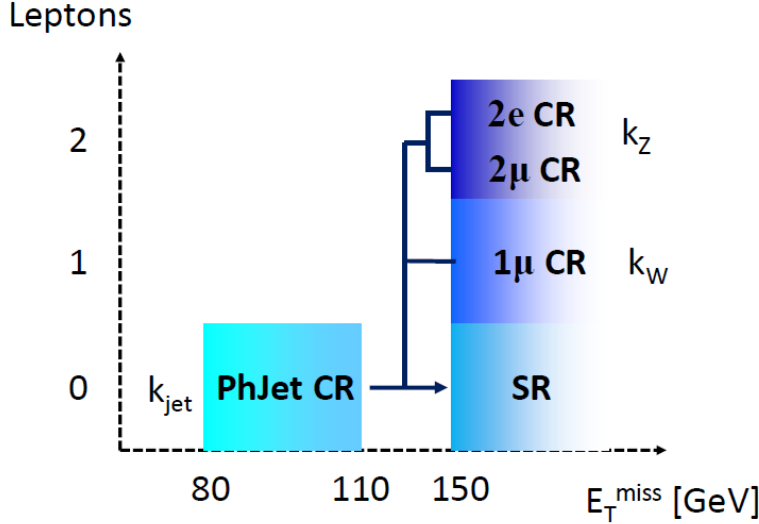


Figure 4.1: Visual representation of the cuts on E_T^{miss} and number of leptons required for the SR with the lower threshold on E_T^{miss} and its CRs. The normalization factors extracted from the CRs and applied to the SR are also shown.

is dominant. The advantage of a simultaneous fit is that data from all the regions of the analysis contribute to constrain the fit parameters at the same time. Furthermore, the simultaneous fitting technique allows to take into account the correlations between the systematic uncertainties across the regions.

The fit is based on the profile likelihood approach: the likelihood is built as the product of the Poisson distributions of the event yields in every region R of the analysis, multiplied with the product of the Gaussian constraints applied to the nuisance parameters. The event yield N_R^{obs} in every region is assumed to be described by the following Poisson distribution:

$$\begin{aligned}
 N_R^{\text{obs}} &\propto \text{Pois} \left(N_R^{\text{obs}} \mid \mu N_R^{\text{sig}} + N_R^{\text{bkg}} \right) \\
 &= \text{Pois} \left(N_R^{\text{obs}} \mid \mu N_R^{\text{sig}} \right. \\
 &\quad + k_Z \times N_R^{Z(\nu\nu)+\gamma} \\
 &\quad + k_W \times N_R^{W(l\nu)+\gamma} \\
 &\quad + k_Z \times N_R^{Z(l\bar{l})+\gamma} \\
 &\quad + k_{\text{jet}} \times N_R^{\text{jet}+\gamma} \\
 &\quad \left. + N_R^{\text{e-to-}\gamma} + N_R^{\text{jet-to-}\gamma} \right),
 \end{aligned}$$

where:

- μN_R^{sig} is the signal yield in the region R : μ is the *signal strength* and N_R^{sig} is the number of signal events.
- $N_R^{Z(\nu\nu)+\gamma}$, $N_R^{W(l\nu)+\gamma}$, $N_R^{Z(l\bar{l})+\gamma}$, and $N_R^{\text{jet}+\gamma}$ are the expected real- γ background yields in the region R , provided by MC simulations. Each yield is multiplied by their scale factor k .
- $N_R^{\text{e-to-}\gamma}$ and $N_R^{\text{jet-to-}\gamma}$ are the two additional background sources from electrons faking photons and from jets faking photons.

The MC event yields depend from the nuisance parameters θ^i , corresponding in this case to systematic uncertainties on MC predictions on each background yield in every region: N_R^X is then

a function of $\vec{\theta}$, i.e. the vector of the nuisance parameters. As already mentioned before, the presence of the nuisance parameters allows the expected background yields to fluctuate from the nominal MC prediction. The Gaussian constraints applied to the nuisance parameters disfavour the simultaneous fit to assign to θ^i a value far from the best expected value. The free parameters of the simultaneous fit are then μ , k_Z , k_W , and k_{jet} , while the systematic uncertainties θ^i are constrained parameters.

The model of the likelihood built for the Mono-Photon analysis is then

$$\mathcal{L}(\mu, \vec{k}, \vec{\theta}) = \prod_R \text{Pois}\left(N_R^{\text{obs}} \mid \mu N_R^{\text{sig}}(\vec{\theta}) + N_R^{\text{bkg}}(\vec{k}, \vec{\theta})\right) f_{\text{constraints}}(\vec{\theta}), \quad (4.1)$$

where \vec{k} is the vector of the normalization factors k_Z , k_W , k_{jet} and $f_{\text{constraints}}(\vec{\theta})$ is the product of the Gaussian constraints on the nuisance parameters. A first background-only fit (i.e. binding the signal strength μ to zero) is then performed on the CRs (without including the SR term in the likelihood) to obtain the normalization factors \vec{k} . A second signal fit on the CRs plus the SR is carried out after unbinding the signal strength μ , using the full likelihood in Eq. (4.1).

4.2.3 Fake- γ background estimation

As already mentioned before, fake- γ background events can't be estimated from MC generated events. The problem of other physics objects mistakenly reconstructed as photons is mainly due to detector imperfections or malfunctions, that MC simulations can't accurately replicate. The event yield from these background sources are to be established with data-driven techniques. In the following, the technique used to estimate the background from electrons faking photons is briefly presented.

Electrons faking photons

The technique used to measure the electron-to-photon fake rate in the Mono-Photon analysis is the *Tag & Probe* method. The fake rate is computed as the ratio of the number of $e\gamma$ couples to the number of ee couples selected from a sample of $Z \rightarrow ee$ events, where the final state can be reconstructed either as ee or as $e\gamma$. The ee couples are made up of a *tag electron*, i.e. a preselected electron with $p_T > 25$ GeV, and a *probe electron*, i.e. a selected electron with $p_T > 150$ GeV. The $e\gamma$ couples are made up of a tag electron and a *probe photon*, defined the same way as signal photons of the Mono-Photon analysis (tight, isolated, $|\eta| < 1.37 \vee 1.52 < |\eta| < 2.37$) with $p_T > 150$ GeV. The fake photons background yield is estimated by defining one probe-electron Control Region for each region of the analysis, defined by the same selection of the corresponding region of the analysis, except that the requirements on the leading photon are replaced with the request to have a probe electron. The measured fake rate is used to scale the event yield of every probe- e CR, and the obtained number is used as the expected number of fake photons in the corresponding region of the analysis. For a further discussion of the background from electron faking photons for the Mono-Photon analysis see the dedicated chapter. Tables 4.2 and 4.3 show the measured electron-to-photon fake rate in four bins in $(|\eta|, p_T)$ and the number of electrons faking photons in the three signal regions and their CRs respectively [8].

Figure 4.2: Electron-to-photon fake rate in % with statistical and systematic uncertainties measured for the Mono-Photon analysis in 2016.

$ \eta $	$p_T[\text{GeV}]$	Fake rate \pm stat \pm syst
<1.37	< 200	$1.07 \pm 0.07 \pm 0.21$
	> 200	$0.59 \pm 0.08 \pm 0.14$
> 1.52	< 200	$2.5 \pm 0.2 \pm 0.3$
	> 200	$2.4 \pm 0.3 \pm 0.5$

Figure 4.3: Electron-to-photon fakes estimated in the SRs and their CRs measured in the Mono-Photon analysis in 2016. The uncertainty is expressed in three terms: The first term is the statistical uncertainty related to the number of events found in the probe- e CR; the second and third terms are the statistical and systematic uncertainties related to the electron fake, respectively. The PhJet CR being defined at low E_T^{miss} , there is no splitting in various E_T^{miss} bins for this region.

E_T^{miss} bins	SR	1 μ CR	2 μ CR	2 e CR	PhJet CR
> 150 GeV	$198.5 \pm 1.8 \pm 18.0 \pm 35.5$	$16.7 \pm 0.5 \pm 1.5 \pm 3.1$	$0.50 \pm 0.09 \pm 0.04 \pm 0.09$	$0.09 \pm 0.04 \pm 0.01 \pm 0.01$	
> 225 GeV	$46.7 \pm 0.9 \pm 5.7 \pm 10.0$	$4.2 \pm 0.2 \pm 0.4 \pm 0.9$	$0.17 \pm 0.05 \pm 0.02 \pm 0.04$	$0.052 \pm 0.030 \pm 0.004 \pm 0.009$	
> 300 GeV	$13.1 \pm 0.4 \pm 1.7 \pm 2.9$	$1.1 \pm 0.1 \pm 0.1 \pm 0.2$	$0.028 \pm 0.015 \pm 0.003 \pm 0.006$	$0.052 \pm 0.030 \pm 0.004 \pm 0.009$	$71.6 \pm 1.1 \pm 6.1 \pm 12.4$

4.3 Results

In the following, the post-fit results of the Mono-Photon analysis are shown [8].

Table 4.4 shows the event yields in the SR with the lower E_T^{miss} threshold and all its CRs for every background source obtained from the simultaneous fit technique and from the data-driven methods for the real- γ and fake- γ backgrounds respectively.

Figure 4.4: Observed event yields compared to expected yields from SM backgrounds in the signal region SR with $E_T^{\text{miss}} > 150$ GeV and in its four CRs, as predicted from the simultaneous fit. The MC yields before the fit are also shown. The uncertainty includes both the statistical and systematic uncertainties. The uncertainty on the pre-fit background is the pre-fit uncertainty, while the uncertainties on the fitted background are post-fit uncertainties.

	SRI1	1muCR	2muCR	2eleCR	PhJetCR
Observed events	2400	1083	254	181	5064
Fitted Background	2600 ± 160	1083 ± 33	243 ± 13	193 ± 10	5064 ± 80
$Z(\rightarrow \nu\nu)\gamma$	1600 ± 110	1.7 ± 0.2	–	–	81 ± 6
$W(\rightarrow \ell\nu)\gamma$	390 ± 24	866 ± 40	1.1 ± 0.3	0.7 ± 0.1	163 ± 9
$Z(\rightarrow \ell\ell)\gamma$	35 ± 3	77 ± 5	233 ± 13	180 ± 10	13 ± 1
$\gamma + \text{jets}$	248 ± 80	33 ± 8	–	–	4451 ± 80
Fake photons from electrons	199 ± 40	17 ± 3	0.50 ± 0.13	0.09 ± 0.04	72 ± 14
Fake photons from jets	152 ± 22	88 ± 19	7.9 ± 3.8	12 ± 5	284 ± 28
Pre-fit background	2400 ± 200	1025 ± 72	218 ± 15	181 ± 13	4800 ± 1000

The event yield is compatible with the background-only hypothesis, as Fig. 4.5 shows.

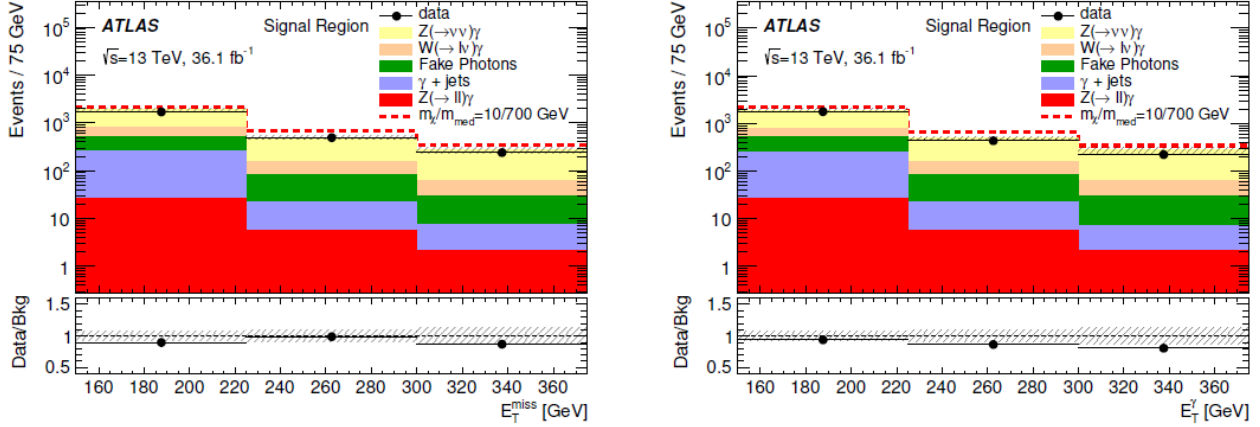


Figure 4.5: Distribution of E_T^{miss} (left) and E_T^γ (i.e. the transverse momentum of the leading photon) (right) in the three signal regions for data and for the expected total background yields. The expected yield of events from the simplified model with $m_\chi = 10$ GeV and a mediator of mass $m_{med} = 700$ GeV with $g_q = 0.25$ and $g_\chi = 1.0$ is stacked on top of the background prediction. The lower panel shows the ratio of data to expected background event yields.

4.4 Search for new physics

The results provided by the simultaneous fit are interpreted with a profile likelihood test statistics. The profile likelihood $\lambda(\mu)$ is defined as

$$\lambda(\mu) = \frac{\mathcal{L}(\mu, \hat{\vec{\theta}}(\mu))}{\mathcal{L}(\hat{\mu}, \hat{\vec{\theta}})}, \quad (4.2)$$

where $\hat{\vec{\theta}}(\mu)$ is the set of nuisance parameters (see Section 4.2) maximizing the likelihood function defined in Section 4.2.2 for a fixed μ , while the denominator is the unconditionally maximized likelihood. Of course $0 \leq \lambda(\mu) \leq 1$, and if $\lambda(\mu)$ approaches 1, the hypothesized value of μ is in good agreement with the measured data. Therefore, the profile likelihood can be used as test statistic. Usually a function t_μ depending from $\lambda(\mu)$ is defined conveniently for carrying out a determined statistical test. The Mono-Photon analysis searches for an excess of events with respect to the number of events expected from the background alone: therefore it is convenient to define a one-sided profile likelihood, i.e. a function t_μ where $\mu \geq 0$. The test statistics is defined as

$$t_\mu = \begin{cases} -2 \ln \frac{\mathcal{L}(\mu, \hat{\vec{\theta}}(\mu))}{\mathcal{L}(0, \hat{\vec{\theta}}(0))} & \hat{\mu} < 0 \\ -2 \ln \frac{\mathcal{L}(\mu, \hat{\vec{\theta}}(\mu))}{\mathcal{L}(\hat{\mu}, \hat{\vec{\theta}})} & \hat{\mu} \geq 0 \end{cases}. \quad (4.3)$$

This one-sided profile likelihood is defined in a way such that if the fit on collected data finds a negative value of $\hat{\mu}$, the best agreement between the data and the model (assuming $\mu \geq 0$) is, indeed, $\mu = 0$. Assuming a certain value of μ , its disagreement with data is quantified by the p-value p_μ :

$$p_\mu = \int_{t_{\mu,obs}}^{\infty} f(t_\mu | \mu) dt_\mu, \quad (4.4)$$

where $f(t_\mu | \mu)$ is the probability density function of t_μ for a given value of μ and $t_{\mu,obs}$ is the value of t_μ resulting from fitting to the collected data. The idea is that if p_μ is small, the probability of finding data with equal or higher incompatibility with the hypothesized μ is small, i.e. the collected

data are incompatible with the hypothesis of a signal strength μ and therefore the hypothesis needs to be rejected, and vice-versa if the computed value of p_μ is large. Finding a small enough p_0 ³ sets a discovery: it implies that the hypothesis of no signal ($\mu = 0$) needs to be rejected. On the other hand, finding a small value of p_μ with $\mu > 0$ sets exclusion limits, i.e. defines regions where the hypothesis of signal with strength μ is rejected⁴. For a thorough description of the likelihood-based approach see [11] and Section 9.5 in [17].

As shown in Table 4.4 and Fig. 4.5, the results of the simultaneous fit are compatible with the background-only hypothesis. Therefore, the profile likelihood based test statistics was employed to set exclusion limits.

Given that the number of selected events coming from a potential new physics process if cross section σ is $N_{new} = L \times \sigma \times A \times \epsilon$, where L is the integrated luminosity and $A \times \epsilon$ is the product of the acceptance and efficiency of the selection criteria, a quantity of interest when searching for new physics is the *visible cross section* $\sigma \times A \times \epsilon$. Table 4.6 shows 95% confidence level (CL) limits on the visible cross section; they were computed without making any hypothesis on the model of new physics.

Figure 4.6: The observed and expected limit at 95% confidence level on the visible cross-section $\sigma \times A \times \epsilon$. The expected limits at 1σ are also reported.

$\sigma \times A \times \epsilon$ limit [fb]	$E_T^{\text{miss}} > 150$ GeV	$E_T^{\text{miss}} > 225$ GeV	$E_T^{\text{miss}} > 300$ GeV
95% CL, observed	5.91	2.73	1.45
95% CL, expected ($\pm 1\sigma$)	8.87(12.18, 6.48)	3.31(4.56, 2.41)	1.95 (2.66, 1.44)

³In particle physics the upper value of p_0 for claiming a discovery is 2.87×10^{-7} .

⁴To be precise, a slightly different function is defined to set upper limits on the signal:

$$t_\mu = \begin{cases} -2 \ln \frac{\mathcal{L}(\mu, \hat{\theta}(\mu))}{\mathcal{L}(0, \hat{\theta}(0))} & \hat{\mu} < 0 \\ -2 \ln \frac{\mathcal{L}(\mu, \hat{\theta}(\mu))}{\mathcal{L}(\hat{\mu}, \hat{\theta})} & 0 \leq \hat{\mu} \leq \mu \\ 0 & \hat{\mu} > \mu \end{cases} \quad (4.5)$$

The reason behind setting $t_\mu = 0$ if $\hat{\mu} > \mu$ is that if the collected data result in a $\hat{\mu}$ larger than the hypothesized upper limit μ , then the collected data are not to be employed to set exclusion limits.

CHAPTER 5

Background from electron faking photons for the Mono-Photon analysis

The background from electrons faking photons is a fake- γ background source for the Mono-Photon analysis. The fraction of prompt electrons being mistakenly reconstructed and identified as photons is primarily due to detector imperfections or malfunctions, and it can only be estimated with a purely in-situ technique. To evaluate the number of such electron fakes, a two-step approach is employed. The first step is to measure the probability of electrons to be mistakenly reconstructed (and identified) as photons, known as the *electron-to-photon fake rate*. The second step consists in applying the electron-to-photon fake rate to retrieve the number of electrons faking photons in every region defined in the Mono-Photon analysis. The work presented in this thesis consists in applying a new method, developed and described in references [17] and [6], for measuring the electron-to-photon fake rate. The results were then used to provide a new estimation of the contribution from electrons faking photons to the SM background for every region defined in the Mono-Photon analysis.

5.1 The electron-to-photon fake rate

The most immediate definition of the electron-to-photon fake rate is the number of true electrons mistakenly reconstructed as photons over the total number of true electrons:

$$\rho = \frac{N_{e^{true} \rightarrow \gamma^{reco}}}{N_{e^{true}}}. \quad (5.1)$$

The latter, however, cannot be obtained when using data. Therefore, the electron-to-photon fake rate can be defined as the ratio of the probability to (wrongly) reconstruct a true electron as a photon to the probability to (correctly) reconstruct a true electron as an electron:

$$F_{e \rightarrow \gamma} \equiv \frac{\epsilon(e^{true} \rightarrow \gamma^{reco}) \epsilon_\gamma}{\epsilon(e^{true} \rightarrow e^{reco}) \epsilon_e}, \quad (5.2)$$

where $\epsilon(e^{true} \rightarrow \gamma^{reco}) = \frac{N_{e^{true} \rightarrow \gamma^{reco}}}{N_{e^{true}}}$ and $\epsilon(e^{true} \rightarrow e^{reco}) = \frac{N_{e^{true} \rightarrow e^{reco}}}{N_{e^{true}}}$, while ϵ_γ and ϵ_e are the identification efficiencies of photon and electrons respectively, used to correct the reconstruction efficiencies $\epsilon(e^{true} \rightarrow \gamma^{reco})$ and $\epsilon(e^{true} \rightarrow e^{reco})$ to yield the correct probability values. Therefore,

$$F_{e \rightarrow \gamma} \equiv \frac{N_{e^{true} \rightarrow \gamma^{reco}} \epsilon_\gamma}{N_{e^{true} \rightarrow e^{reco}} \epsilon_e} \equiv P(\gamma_{ID, \text{iso}} | e_{ID, \text{iso}}). \quad (5.3)$$

This definition of the fake rate is independent from the non-measurable quantity $N_{e^{true}}$ and it is related to ρ as

$$F_{e \rightarrow \gamma} = \frac{\rho}{1 - \rho} \frac{\epsilon_\gamma}{\epsilon_e}. \quad (5.4)$$

The challenge is then to select a physics process where it is possible to discriminate a fake photon, misreconstructed from a true electron, from a true photon and compare the number of fake photons with the number of correctly reconstructed electron. For the present measure, the electron-to-photon fake rate is determined from a pure sample of $Z \rightarrow ee$ events. The di-electron in the final state is clearly made up of true electrons, which can be reconstructed either as electrons or

as photons. In practice, the measure of the fake rate consists in selecting, for every event in the sample, a couple (ee or $e\gamma$) whose invariant mass (m_{ee} or $m_{e\gamma}$) is compatible with the mass of the Z boson (91.18 GeV), and comparing the Z boson mass spectra resulting from ee couples and $e\gamma$ couples. Background yields are subtracted from the invariant mass distributions, allowing to perform a comparison between true final states from Z decays. The fake rate is measured as a function of η in the range (-2.37, 2.37), and as a function of p_T in different $|\eta|$ intervals ($0 - 0.8 - 1.15 - 1.37, 1.52 - 1.81 - 2.01 - 2.37$), where the considered transverse momentum values were between 25 GeV and 300 GeV. The results are presented for two overlap removal procedures (a technique used in ATLAS to avoid ambiguities between objects reconstructed as two different particles), one favouring electrons over photons ("OR retaining e ") and one favouring photons over electrons ("OR retaining γ ").

5.1.1 Event selection

A selection on $Z \rightarrow ee$ events from the sample is performed.

The events are required to contain at least two electrons or an electron and a photon satisfying the preselection criteria of the Mono-Photon analysis. The overlap removal procedure is then applied on the preselected objects. If a preselected electron and a preselected photon fall within a cone of radius $\Delta R < 0.4$ from each other, the photon (electron) is removed when applying the overlap removal algorithm favouring electrons (photons).

After passing the preliminary requirements mentioned above, electrons and photons are retained if they satisfy the following criteria:

- Kinematic selection: the transverse momentum is required to be larger than 25 GeV and $|\eta| < 2.37$, excluding the crack region $1.52 < |\eta| < 2.37$ of the EM calorimeter.
- Electrons need to be selected by the likelihood-based medium identification working point, while photons are required to be selected by the tight identification working point (see Sections 3.1.2 and 3.2.2.).
- Both electrons and photons need to be isolated (see Sections 3.1.3 and 3.2.3). Electrons are required to be selected by the "loose" isolation working point, i.e. an efficiency-based operating point optimized to obtain an efficiency of $\sim 99\%$ on a sample of electrons of tight quality. Photons need to be selected by the "FixedCutTight" isolation working point.

If at least two electrons or one electron and a photon pass the previous requirements, the *best couple*, being either a ee couple or a $e\gamma$ couple, is the couple whose invariant mass is the closest to the mass of the Z boson. If the best couple is revealed to be ee couple, in addition, the two electrons need to have opposite signs.

5.1.2 Fake-rate estimation

Let's consider the measure of the fake rate as a function of η and p_T .

A two-dimensional histogram $H_{ee}(\eta^e, p_T^e)$ is defined, where η^e and p_T^e are the pseudorapidity and transverse momentum of reconstructed electrons in the final state. Every (η^e, p_T^e) bin is matched to a m_{ee} distribution, where m_{ee} is the invariant mass of a best ee couple, where pseudorapidity and the transverse momentum of at least one electron of the pair belong to the (η^e, p_T^e) bin. Similarly, a two dimensional histogram $H_{e\gamma}(\eta^\gamma, p_T^\gamma)$ is set up: η^γ and p_T^γ are the pseudorapidity and transverse momentum of reconstructed photons in the final state. Again, every $(\eta^\gamma, p_T^\gamma)$ bin is matched to a $m_{e\gamma}$ distribution, where $m_{e\gamma}$ is the invariant mass of a best $e\gamma$ couple, where the the pseudorapidity and the transverse momentum of the photon belong to the $(\eta^\gamma, p_T^\gamma)$ bin. The established invariant mass distributions correspond to mass spectra of the Z boson, labelled with a reconstructed final state ee (for m_{ee} distributions) or $e\gamma$ (for $m_{e\gamma}$ distributions). A secondary label provides a further

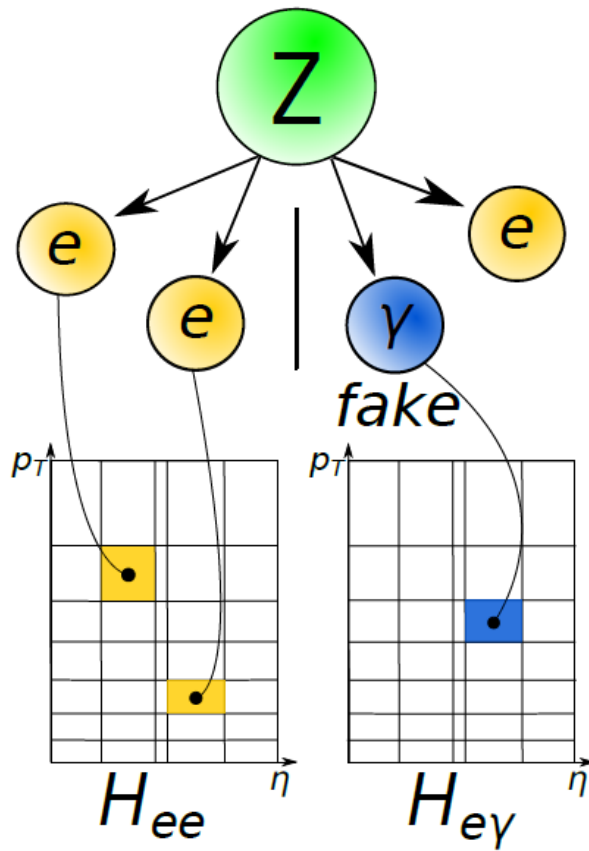


Figure 5.1: Graphical representation of the method of filling the invariant mass distributions. Each bin of the two histograms H_{ee} and $H_{e\gamma}$ corresponds to a m_{ee} or to a $m_{e\gamma}$ distribution. From [17].

classification on the distributions, based on the η and p_T intervals of the objects in the final state. The invariant mass distributions are filled as explained below.

- If the selected best couple of an event is a ee couple, the pseudorapidity and the transverse momentum of the first electron are matched to their (η^e, p_T^e) bin, and therefore to a m_{ee} distribution. The matching m_{ee} distribution is filled with the invariant mass of the ee couple. The same procedure is applied for the second electron. Therefore, if the best couple of an event is a ee couple, two m_{ee} distributions are filled with the same invariant mass. If, by chance, the pseudorapidity and the transverse momentum of both the electrons belong to the same (η^e, p_T^e) bin, the same m_{ee} distribution is filled twice with the same invariant mass.
- If the selected best couple of an event is a $e\gamma$ couple, the pseudorapidity and the transverse momentum of the photon are matched to their $(\eta^\gamma, p_T^\gamma)$ bin, and therefore to a $m_{e\gamma}$ distribution. The matching $m_{e\gamma}$ distribution is filled with the invariant mass of the $e\gamma$ couple. In this case, only one $m_{e\gamma}$ distribution is filled per event.

This procedure is summarized in Fig. 5.1. The fake rate as a function of η and p_T is computed as

$$F_{e \rightarrow \gamma}(\eta, p_T) = \frac{S_{e\gamma}(\eta^\gamma, p_T^\gamma)}{S_{ee}(\eta^e, p_T^e)}, \quad (5.5)$$

where S_{ee} and $S_{e\gamma}$ are the number of signal events extracted from the m_{ee} and $m_{e\gamma}$ distributions respectively. The motivation for this procedure can be understood as follows.

As a first approximation, let's neglect the effect of the background subtraction: let's assume

that the number of signal events used to compute the fake rate coincides with the total number of events extracted from the distributions, or, to put it in another way, let's assume that there is no background contamination in the invariant mass distributions. If this is the case, $S_{ee} = N_{ee}$ and $S_{e\gamma} = N_{e\gamma}$, where N_{ee} and $N_{e\gamma}$ are the total number of events in m_{ee} and $m_{e\gamma}$ distributions respectively. Secondly, let's assume there is no binning in η and p_T , i.e. there is a single m_{ee} distribution and a single $m_{e\gamma}$ distribution: this simplified case can be easily generalized to a situation in which a binning in η and p_T is applied.

Given the $Z \rightarrow ee$ event sample, being ϵ_γ and ϵ_e the identification efficiencies of photons and electrons respectively, and being ρ the true fake rate as defined in Eq. (5.1), the probability of finding a number of reconstructed ee , $e\gamma$, and $\gamma\gamma$ as final states is

$$\begin{aligned} N_{ee} &= \epsilon_e^2 (1 - \rho)^2 N_Z \\ N_{e\gamma} &= 2\epsilon_e \epsilon_\gamma \rho (1 - \rho) N_Z \\ N_{\gamma\gamma} &= \epsilon_\gamma^2 \rho^2 N_Z, \end{aligned}$$

where N_{ee} , $N_{e\gamma}$, $N_{\gamma\gamma}$ are the numbers of each reconstructed final state, N_Z is the number of true Z decays, and the factor 2 in the expression of $N_{e\gamma}$ is to take into account both the cases in which either the first electron is wrongly reconstructed as a photon ($ee \rightarrow \gamma^{fake} e$) or the second electron is wrongly reconstructed as a photon $ee \rightarrow e\gamma^{fake}$.

The fake rate, as defined in Eq. (5.3), can be expressed as

$$F_{e \rightarrow \gamma} = \frac{N_{e^{true} \rightarrow \gamma^{reco}} \epsilon_\gamma}{N_{e^{true} \rightarrow e^{reco}} \epsilon_e} = \frac{N_{e\gamma} + 2N_{\gamma\gamma}}{2N_{ee} + N_{e\gamma}}. \quad (5.6)$$

The second equivalence is explained as follows:

- being di-electrons the true final states of $Z \rightarrow ee$ events, the number of true electrons misreconstructed as photons is given by the number of reconstructed $e\gamma$ final states (where a single electron is misreconstructed as a photon) plus two times the number of $N_{\gamma\gamma}$ final states (where both the electrons are misreconstructed as photons);
- similarly, the number of true electrons correctly reconstructed as electrons is given by the sum of two times the number of reconstructed ee final states (where both the electrons are correctly reconstructed as electrons) and the number of reconstructed $e\gamma$ final states (where a single electron is correctly reconstructed as an electron).

The quantity $\frac{N_{e\gamma} + 2N_{\gamma\gamma}}{2N_{ee} + N_{e\gamma}}$ is equal to:

$$\begin{aligned} \frac{N_{e\gamma} + 2N_{\gamma\gamma}}{2N_{ee} + N_{e\gamma}} &= \frac{2\epsilon_e \epsilon_\gamma \rho (1 - \rho) N_Z + 2\epsilon_\gamma^2 \rho^2 N_Z}{2\epsilon_e^2 (1 - \rho)^2 N_Z + 2\epsilon_e \epsilon_\gamma \rho (1 - \rho) N_Z} \\ &= \frac{\epsilon_e \epsilon_\gamma \rho (1 - \rho) + \epsilon_\gamma^2 \rho^2}{\epsilon_e^2 (1 - \rho)^2 + \epsilon_e \epsilon_\gamma \rho (1 - \rho)} \\ &= \frac{\epsilon_\gamma \rho [\epsilon_e (1 - \rho) + \epsilon_\gamma \rho]}{\epsilon_e (1 - \rho) [\epsilon_e (1 - \rho) + \epsilon_\gamma \rho]} \\ &= \frac{\rho}{1 - \rho} \frac{\epsilon_\gamma}{\epsilon_e}. \end{aligned}$$

The same result is obtained expressing the quantity $\frac{N_{e\gamma}}{2N_{ee}}$ as a function of ρ , ϵ_γ and ϵ_e :

$$\begin{aligned} \frac{N_{e\gamma}}{2N_{ee}} &= \frac{2\epsilon_e \epsilon_\gamma \rho (1 - \rho) N_Z}{2\epsilon_e^2 (1 - \rho)^2 N_Z} \\ &= \frac{\rho}{1 - \rho} \frac{\epsilon_\gamma}{\epsilon_e}. \end{aligned}$$

Therefore, the fake rate can be computed as

$$F_{e \rightarrow \gamma} = \frac{N_{e\gamma}}{2N_{ee}}, \quad (5.7)$$

which is exactly what happens if the invariant mass distributions are filled as described above.

The fake rate is measured as a function of η in a range of $(-2.37, 2.37)$ using bins of fixed width equal to 0.1. The crack region $((-1.5, -1.4) \cup (1.4, 1.5))$ is excluded. A measure of the fake rate as a function of $|\eta|$ and p_T was also performed, where the binning of choice¹ was

- 6 bins in $|\eta|$: $0 - 0.8 - 1.15 - 1.37, 1.52 - 1.81 - 2.01 - 2.37$;
- 8 bins in p_T : $25 - 35 - 45 - 55 - 65 - 75 - 100 - 150 - 300$ GeV.

5.1.3 Background subtraction

As already mentioned before, the fake rate in a certain bin is measured as the ratio of $S_{e\gamma}$ to S_{ee} , where $S_{e\gamma}$ and S_{ee} are the signal events extracted from the m_{ee} and $m_{e\gamma}$ distributions matched to the selected bin. The discrimination of signal events from background events is provided by fitting the invariant mass distributions with a *signal + background* model. The model was defined differently for the two measurements of the fake rate, as a function of η and as a function of $|\eta|$ and p_T . In both cases the mass distributions show a narrow signal peak centered on the mass of the Z boson, spiring from a non-resonant background. In the case of the mass distributions labelled by $(|\eta|, p_T)$ bins, a secondary broad peak shows up, centered on the lower value of the transverse momentum in a determined bin multiplied by 2, whose presence is due to kinematic cuts on p_T . Therefore, while the background is modelled as an exponential of a second-degree polynomial in both cases, the signal distribution is modelled by:

- a double-sided Crystal Ball² for mass distributions labelled by η bins.
- the sum of a double-sided Crystal Ball (for the narrow Z -peak) and a gaussian distribution (for the broad peak) for mass distributions labelled by $(|\eta|, p_T)$ bins.

The free parameters of the fit are:

- the normalization factors N_S and N_B for the signal and background distributions respectively;
- the parameters describing the shape of the background distribution (a and b for the distribution e^{-ax-bx^2});
- the parameters describing the shape of double-Sided Crystal Ball distribution (σ_0 and m_0 as standard deviation and mean of the gaussian core, n_{Low} and n_{High} as the powers of the power-law tails on the left and on the right of the peak, and finally α_{Low} and α_{High} as the parameters describing the connection between the gaussian core and the tails on the left and on the right of the peak);
- the parameters describing the shape of the gaussian distribution, if it is included in the model, i.e. a standard deviation σ and a mean μ_0 .

¹As for the measure as a function of $|\eta|$ and p_T , the binning in the absolute value of pseudorapidity responds to two needs: firstly, the fake rate is found to increase with $|\eta|$ (see Section 5.1.4), therefore the $|\eta|$ intervals are chosen to include fake rate values as stable as possible as functions of $|\eta|$ only in their $|\eta|$ bin. Secondly, the mass spectra need to contain enough events to perform a reliable measurement; this second criterium also helped to select the binning in p_T .

²A double-sided Crystal Ball is a distribution with a gaussian core and two power-law tails.

Performing a fit on the mass distributions allows to select pure $Z \rightarrow ee$ final states by considering the sole signal distribution to extract $S_{e\gamma}$ and S_{ee} values. $S_{e\gamma}$ and S_{ee} are ultimately obtained by integrating the corresponding signal distributions (multiplied, of course, for their normalization factor N_S) in a determined *invariant mass window* centered around the Z -peak to exclude the distributions' tails, mainly filled with background events. For $m_{e\gamma}$ distributions, the window corresponds to $[\mu_0 - 3\sigma_{ee}, \mu_0 + 3\sigma_{ee}]$, where μ_0 is the peak position, recovered from the fit, while σ_{ee} is the standard deviation of the double-sided Crystal Ball recovered from fitting the inclusive m_{ee} distribution with the same signal+background model described above. The fitted m_{ee} distributions for both the overlap removal procedures are shown in Fig. 5.2. The window is defined similarly for m_{ee} distributions. The choice of an invariant mass window which is symmetric around the peak position was made to take into account the slight shift between $m_{e\gamma}$ and m_{ee} distributions. The calibration of the energy of the (fake) photon in the reconstructed $e\gamma$ final state is performed assuming that the reconstructed photon is, indeed, a photon. Therefore, the energy measured by the calibration algorithm is slightly different from the calibrated energy which would be attributed to the particle if the latter were correctly reconstructed as an electron. The observed slight shift between $m_{e\gamma}$ and m_{ee} distributions is a result of the effect on energy calibration caused by misreconstruction of electrons.

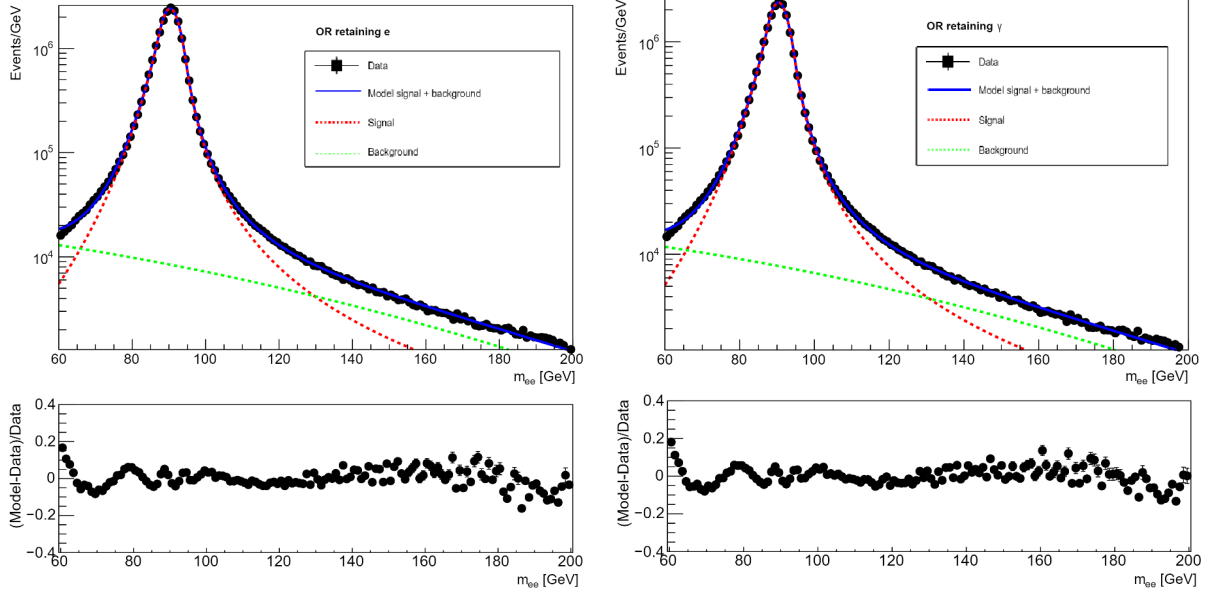


Figure 5.2: Signal+Background fit on the inclusive m_{ee} distributions, for the overlap removal favouring electrons (top) and photons (bottom).

5.1.4 Systematic uncertainties

Three main sources of systematic uncertainties related to the methodology used to perform the measurement have been identified:

- the invariant mass range used for selecting the signal events $S_{e\gamma}$ and S_{ee} .
- the effect of the background subtraction;
- the bias in the reconstructed electrons and photons energy distributions due to the fact that the energy calibration of reconstructed photon is performed as for true photons.

The contributions to the systematic uncertainty from the three sources listed above were evaluated: respectively, the measured relative contributions were approximately 2 – 3%, 5 – 6%, and 1 – 2% (10%) for the measure of the electron-to-photon fake rate as a function of η ($|\eta|$ and p_T) respectively.

These contributions were estimated by performing a new measurement of the fake rate, acting on the source of the uncertainty. The variation(s) thus obtained is then subtracted from the nominal value of the fake rate: the contribution to the systematic uncertainty from the considered source is evaluated as the absolute value of the computed difference. The variations of the fake rate for the three investigated sources are evaluated as follows.

- The signal events $S_{e\gamma}$ and S_{ee} are extracted from invariant mass windows of smaller and larger widths. The nominal window was changed from $[m_0 - 3\sigma, m_0 + 3\sigma]$ to $[m_0 - 2\sigma, m_0 + 2\sigma]$ and to $[m_0 - 4\sigma, m_0 + 4\sigma]$. The two variations of the fake rate are thus obtained from more and less pure samples of final states from Z boson decays.
- To evaluate the contribution to the systematic uncertainty of the background subtraction, a measure of the fake rate is performed without selecting exclusively signal events, i.e. integrating directly on the whole $m_{e\gamma}$ and m_{ee} distributions.
- Finally, the energy of the fake photons was increased and decreased of 1.5% before applying the selection criteria. The value of 1.5% was chosen after comparing the positions of the peak of m_{ee} and $m_{e\gamma}$ distributions. Let's consider a true final state e_1e_2 , where the second electron is mistakenly reconstructed as a photon. If the electron were correctly reconstructed as an electron, its calibrated energy would be E_{e2} . Instead, the calibrated energy of the (fake) photon is E_γ . A scale factor α_{fake} , depending of course from η and p_T of the fake photon, is assumed to be present between E_γ and E_{e2} . The invariant mass of a ee couple would then be

$$m_{ee} = \sqrt{2E_{e1}E_{e2}(1 - \cos \theta)} \quad (5.8)$$

while the invariant mass of a $e\gamma$ couple would be

$$m_{e\gamma} = \sqrt{2E_{e1}E_\gamma(1 - \cos \theta)} = \sqrt{2E_{e1}\alpha_{fake}E_{e2}(1 - \cos \theta)} \quad (5.9)$$

Therefore, the scale factor α_{fake} is estimated to coincide with $\left(\frac{m_{e\gamma}}{m_{ee}}\right)^2$.

5.1.5 Results

The measured values of the electron-to-photon fake rate as a function of η are reported in Tables 5.1 and 5.2 for the overlap removal procedure retaining electrons and photons respectively. The statistic uncertainty and the different contributions to the systematic uncertainty are also shown. The fake rate was found to increase with the absolute value of η : the lower values, found for η close to 0, are approximately 2%, reaching approximately 7.5% (12%) for the overlap removal algorithm favouring electrons (photons) for $\eta \sim \pm 2.4$. The total uncertainty, corresponding to the combination of statistic and systematic uncertainties, is approximately 8 – 10% of the fake rate values.

The above-mentioned measurements are summarized in Fig. 5.3. Both the systematic (yellow bands) and total (error bars) uncertainties are highlighted.

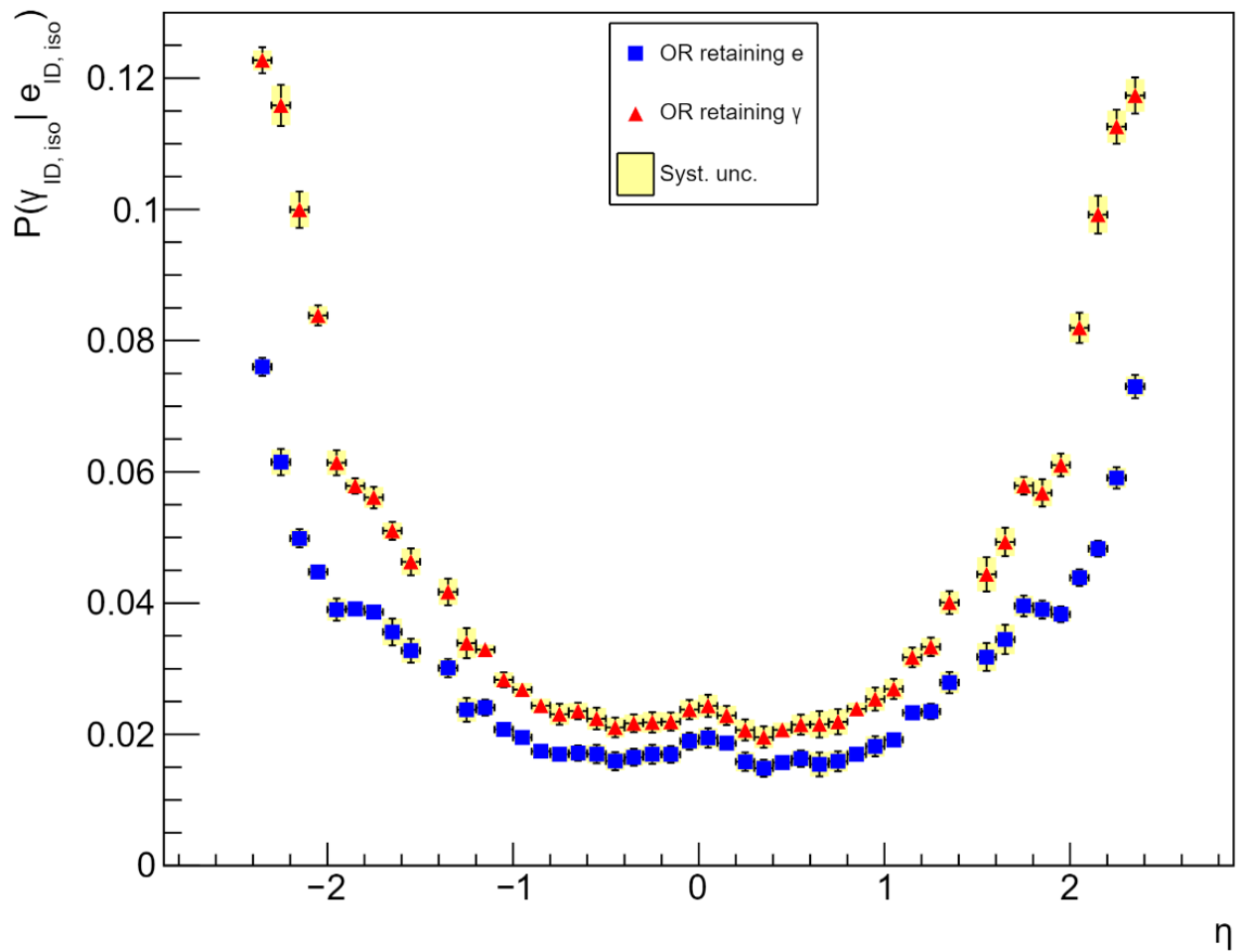


Figure 5.3: Fake rate as a function of η integrated over p_T for the overlap removal procedure retaining electrons (blue squares) and the overlap removal procedure retaining photons (red triangles). The error bars represent the total uncertainty, while the yellow bands represent the systematic uncertainty.

Table 5.1: Fake rates for each η bin in $-2.37 < \eta < 2.37$, evaluated from the events selected using the overlap algorithm favoring electrons. The table reports the central value, the statistical, the systematic and the total uncertainty. For the systematic errors also the contribution from the different sources is listed: the uncertainty due to the variation of the invariant mass selection range (*Window*), the variation of the background subtraction procedure (*Background subtraction*), and the variation of the energy scale of the fake photon (*Scale*).

η	$F_{e \rightarrow \gamma}$	Stat.	Syst.				Total unc.
			Window	Background subtraction	Scale	Total	
[-2.37, -2.30]	0.0760	0.0010	0.0004	0.0001	0.0008	0.0010	0.0014
[-2.30, -2.20]	0.0615	0.0007	0.0003	0.0018	0.0006	0.0019	0.0020
[-2.20, -2.10]	0.0499	0.0006	0.0001	0.0012	0.0005	0.0013	0.0014
[-2.10, -2.00]	0.0448	0.0005	0.0005	0.0001	0.0008	0.0009	0.0010
[-2.00, -1.90]	0.0390	0.0005	0.0001	0.0016	0.0004	0.0016	0.0017
[-1.90, -1.80]	0.0391	0.0005	0.0002	0.0007	0.0001	0.0007	0.0008
[-1.80, -1.70]	0.0386	0.0004	0.0002	0.0003	0.0005	0.0006	0.0008
[-1.70, -1.60]	0.0356	0.0004	0.0002	0.0020	0.0000	0.0020	0.0020
[-1.60, -1.50]	0.0328	0.0004	0.0003	0.0018	0.0002	0.0018	0.0019
[-1.40, -1.30]	0.0301	0.0004	0.0004	0.0012	0.0004	0.0013	0.0014
[-1.30, -1.20]	0.0237	0.0003	0.0004	0.0017	0.0001	0.0018	0.0018
[-1.20, -1.10]	0.0241	0.0003	0.0004	0.0011	0.0001	0.0012	0.0012
[-1.10, -1.00]	0.0207	0.0003	0.0006	0.0006	0.0004	0.0009	0.0010
[-1.00, -0.90]	0.0195	0.0002	0.0003	0.0007	0.0002	0.0008	0.0008
[-0.90, -0.80]	0.0174	0.0002	0.0003	0.0006	0.0000	0.0007	0.0007
[-0.80, -0.70]	0.0170	0.0002	0.0005	0.0010	0.0001	0.0011	0.0011
[-0.70, -0.60]	0.0171	0.0002	0.0004	0.0011	0.0002	0.0012	0.0012
[-0.60, -0.50]	0.0170	0.0002	0.0004	0.0013	0.0000	0.0014	0.0014
[-0.50, -0.40]	0.0159	0.0002	0.0004	0.0013	0.0001	0.0014	0.0014
[-0.40, -0.30]	0.0165	0.0002	0.0004	0.0012	0.0002	0.0013	0.0013
[-0.30, -0.20]	0.0170	0.0002	0.0005	0.0013	0.0001	0.0014	0.0014
[-0.20, -0.10]	0.0169	0.0002	0.0004	0.0012	0.0002	0.0013	0.0013
[-0.10, 0.00]	0.0190	0.0002	0.0005	0.0011	0.0003	0.0013	0.0013
[0.00, 0.10]	0.0195	0.0002	0.0004	0.0014	0.0001	0.0015	0.0015
[0.10, 0.20]	0.0187	0.0002	0.0006	0.0009	0.0003	0.0011	0.0011
[0.20, 0.30]	0.0158	0.0002	0.0005	0.0013	0.0003	0.0014	0.0014
[0.30, 0.40]	0.0148	0.0002	0.0005	0.0012	0.0000	0.0013	0.0013
[0.40, 0.50]	0.0157	0.0002	0.0004	0.0009	0.0002	0.0010	0.0010
[0.50, 0.60]	0.0163	0.0002	0.0004	0.0012	0.0001	0.0012	0.0013
[0.60, 0.70]	0.0154	0.0002	0.0003	0.0018	0.0000	0.0018	0.0018
[0.70, 0.80]	0.0159	0.0002	0.0003	0.0015	0.0001	0.0015	0.0015
[0.80, 0.90]	0.0170	0.0002	0.0004	0.0007	0.0003	0.0009	0.0009
[0.90, 1.00]	0.0182	0.0002	0.0003	0.0015	0.0001	0.0015	0.0015
[1.00, 1.10]	0.0192	0.0003	0.0003	0.0009	0.0002	0.0010	0.0010
[1.10, 1.20]	0.0233	0.0003	0.0004	0.0007	0.0002	0.0008	0.0009
[1.20, 1.30]	0.0235	0.0003	0.0003	0.0010	0.0004	0.0011	0.0012
[1.30, 1.40]	0.0279	0.0004	0.0001	0.0016	0.0001	0.0016	0.0016
[1.50, 1.60]	0.0318	0.0004	0.0001	0.0021	0.0001	0.0021	0.0021
[1.60, 1.70]	0.0345	0.0004	0.0001	0.0022	0.0002	0.0022	0.0022
[1.70, 1.80]	0.0396	0.0004	0.0001	0.0015	0.0004	0.0015	0.0016
[1.80, 1.90]	0.0390	0.0005	0.0001	0.0013	0.0001	0.0013	0.0014
[1.90, 2.00]	0.0383	0.0005	0.0002	0.0010	0.0004	0.0011	0.0012
[2.00, 2.10]	0.0439	0.0005	0.0003	0.0010	0.0006	0.0012	0.0013
[2.10, 2.20]	0.0483	0.0005	0.0003	0.0009	0.0004	0.0011	0.0012
[2.20, 2.30]	0.0591	0.0006	0.0003	0.0014	0.0006	0.0015	0.0016
[2.30, 2.37]	0.0730	0.0010	0.0004	0.0013	0.0006	0.0015	0.0018

Table 5.2: Fake rates for each η bin in $-2.37 < \eta < 2.37$, evaluated from the events selected using the overlap algorithm favoring photons. The table reports the central value, the statistical, the systematic and the total uncertainty. For the systematic errors also the contribution from the different sources is listed: the uncertainty due to the variation of the invariant mass selection range (*Window*), the variation of the background subtraction procedure (*Background subtraction*), and the variation of the energy scale of the fake photon (*Scale*).

η	$F_{e \rightarrow \gamma}$	Stat.	Syst.				Total unc.
			Window	Background subtraction	Scale	Total	
[-2.37, -2.30]	0.1227	0.0013	0.0008	0.0002	0.0012	0.0015	0.0020
[-2.30, -2.20]	0.1159	0.0010	0.0009	0.0028	0.0005	0.0030	0.0031
[-2.20, -2.10]	0.1000	0.0008	0.0003	0.0026	0.0002	0.0026	0.0028
[-2.10, -2.00]	0.0838	0.0007	0.0007	0.0002	0.0011	0.0014	0.0015
[-2.00, -1.90]	0.0614	0.0006	0.0001	0.0018	0.0000	0.0018	0.0019
[-1.90, -1.80]	0.0579	0.0006	0.0003	0.0010	0.0001	0.0010	0.0012
[-1.80, -1.70]	0.0561	0.0005	0.0002	0.0015	0.0000	0.0016	0.0016
[-1.70, -1.60]	0.0510	0.0005	0.0001	0.0012	0.0002	0.0013	0.0014
[-1.60, -1.50]	0.0463	0.0005	0.0002	0.0019	0.0003	0.0020	0.0021
[-1.40, -1.30]	0.0417	0.0005	0.0003	0.0018	0.0006	0.0020	0.0020
[-1.30, -1.20]	0.0339	0.0004	0.0004	0.0022	0.0001	0.0023	0.0023
[-1.20, -1.10]	0.0329	0.0003	0.0004	0.0005	0.0003	0.0007	0.0008
[-1.10, -1.00]	0.0283	0.0003	0.0007	0.0009	0.0001	0.0011	0.0011
[-1.00, -0.90]	0.0268	0.0003	0.0004	0.0009	0.0003	0.0010	0.0011
[-0.90, -0.80]	0.0244	0.0003	0.0004	0.0009	0.0003	0.0010	0.0010
[-0.80, -0.70]	0.0231	0.0003	0.0005	0.0015	0.0002	0.0016	0.0016
[-0.70, -0.60]	0.0235	0.0003	0.0004	0.0012	0.0001	0.0012	0.0013
[-0.60, -0.50]	0.0224	0.0003	0.0005	0.0016	0.0000	0.0016	0.0017
[-0.50, -0.40]	0.0211	0.0002	0.0004	0.0014	0.0000	0.0015	0.0015
[-0.40, -0.30]	0.0217	0.0003	0.0006	0.0012	0.0002	0.0013	0.0013
[-0.30, -0.20]	0.0218	0.0003	0.0005	0.0015	0.0002	0.0015	0.0016
[-0.20, -0.10]	0.0219	0.0003	0.0005	0.0013	0.0001	0.0014	0.0014
[-0.10, 0.00]	0.0238	0.0003	0.0005	0.0014	0.0002	0.0015	0.0015
[0.00, 0.10]	0.0243	0.0003	0.0004	0.0016	0.0000	0.0017	0.0017
[0.10, 0.20]	0.0229	0.0003	0.0006	0.0013	0.0002	0.0014	0.0015
[0.20, 0.30]	0.0207	0.0002	0.0006	0.0015	0.0003	0.0016	0.0016
[0.30, 0.40]	0.0196	0.0002	0.0005	0.0015	0.0001	0.0016	0.0016
[0.40, 0.50]	0.0207	0.0002	0.0005	0.0009	0.0003	0.0011	0.0011
[0.50, 0.60]	0.0215	0.0002	0.0005	0.0014	0.0000	0.0015	0.0015
[0.60, 0.70]	0.0215	0.0003	0.0004	0.0019	0.0001	0.0020	0.0020
[0.70, 0.80]	0.0219	0.0003	0.0004	0.0019	0.0001	0.0019	0.0019
[0.80, 0.90]	0.0239	0.0003	0.0006	0.0007	0.0003	0.0009	0.0010
[0.90, 1.00]	0.0254	0.0003	0.0003	0.0017	0.0001	0.0017	0.0018
[1.00, 1.10]	0.0269	0.0003	0.0005	0.0014	0.0003	0.0015	0.0015
[1.10, 1.20]	0.0317	0.0003	0.0005	0.0014	0.0002	0.0015	0.0015
[1.20, 1.30]	0.0333	0.0004	0.0004	0.0013	0.0003	0.0014	0.0014
[1.30, 1.40]	0.0401	0.0005	0.0002	0.0017	0.0001	0.0017	0.0017
[1.50, 1.60]	0.0444	0.0005	0.0002	0.0025	0.0001	0.0026	0.0026
[1.60, 1.70]	0.0493	0.0005	0.0001	0.0016	0.0013	0.0021	0.0022
[1.70, 1.80]	0.0579	0.0006	0.0002	0.0010	0.0008	0.0012	0.0014
[1.80, 1.90]	0.0568	0.0006	0.0002	0.0020	0.0000	0.0020	0.0021
[1.90, 2.00]	0.0611	0.0006	0.0002	0.0015	0.0006	0.0016	0.0017
[2.00, 2.10]	0.0819	0.0007	0.0002	0.0022	0.0000	0.0022	0.0023
[2.10, 2.20]	0.0992	0.0008	0.0010	0.0024	0.0008	0.0028	0.0029
[2.20, 2.30]	0.1126	0.0010	0.0007	0.0021	0.0009	0.0024	0.0026
[2.30, 2.37]	0.1174	0.0013	0.0005	0.0024	0.0003	0.0024	0.0028

In Tables from 5.3 to 5.8 the electron-to-photon fake rate values as a function of p_T in the $|\eta|$ intervals ($0 - 0.8 - 1.15 - 1.37, 1.52 - 1.81 - 2.01 - 2.37$) for the overlap removal procedure favouring electrons are presented, together with statistic, systematic, and total uncertainties. Tables from 5.9 to 5.14 show the same results for the overlap removal procedure favouring photons. The fake rate is found to be approximately constant as a function of p_T in every $|\eta|$ interval, with a slight tendency to decrease (increase) with increasing p_T for the overlap removal procedure retaining electrons (photons). The total uncertainty lies between 10% and 15% of the fake rate values. Fig. 5.4 shows the fake rate as a function of p_T in every $|\eta|$ interval, for both the overlap removal procedures. The total systematic uncertainty is highlighted by a yellow band, while the error bars represent the total uncertainty.

Table 5.3: Fake rates for $p_T \in [25 \text{ GeV}, 300 \text{ GeV}]$ and $0 \leq |\eta| < 0.8$, evaluated from the events selected using the overlap algorithm favoring electrons. The table reports the central value, the statistical, the systematic and the total uncertainty. For the systematic errors also the contribution from the different sources is listed: the uncertainty due to the variation of the invariant mass selection range (*Window*), the variation of the background subtraction procedure (*Background subtraction*), and the variation of the energy scale of the fake photon (*Scale*).

p_T [GeV]	$F_{e \rightarrow \gamma}$	Stat.	$0 \leq \eta < 0.8$					Total unc.	
			Window	Syst.		Scale	Total		
				Background subtraction	Scale				
[25, 35]	0.0181	0.0001	0.0009	0.0014	0.0016	0.0023	0.0023		
[35, 45]	0.0177	0.0001	0.0006	0.0003	0.0003	0.0007	0.0007		
[45, 55]	0.0170	0.0001	0.0005	0.0001	0.0017	0.0018	0.0018		
[55, 65]	0.0175	0.0002	0.0006	0.0009	0.0013	0.0017	0.0017		
[65, 75]	0.0181	0.0004	0.0007	0.0005	0.0022	0.0023	0.0024		
[75, 100]	0.0136	0.0004	0.0004	0.0027	0.0011	0.0030	0.0030		
[100, 150]	0.0122	0.0006	0.0010	0.0007	0.0004	0.0012	0.0014		
[150, 300]	0.0117	0.0010	0.0014	0.0004	0.0013	0.0019	0.0022		

Table 5.4: Fake rates for $p_T \in [25 \text{ GeV}, 300 \text{ GeV}]$ and $0.8 \leq |\eta| < 1.15$, evaluated from the events selected using the overlap algorithm favoring electrons. The table reports the central value, the statistical, the systematic and the total uncertainty. For the systematic errors also the contribution from the different sources is listed: the uncertainty due to the variation of the invariant mass selection range (*Window*), the variation of the background subtraction procedure (*Background subtraction*), and the variation of the energy scale of the fake photon (*Scale*).

p_T [GeV]	$F_{e \rightarrow \gamma}$	Stat.	$0.8 \leq \eta < 1.15$					Total unc.	
			Window	Syst.		Scale	Total		
				Background subtraction	Scale				
[25, 35]	0.0207	0.0002	0.0008	0.0018	0.0021	0.0029	0.0029		
[35, 45]	0.0202	0.0001	0.0005	0.0001	0.0002	0.0005	0.0005		
[45, 55]	0.0194	0.0002	0.0007	0.0002	0.0020	0.0021	0.0021		
[55, 65]	0.0195	0.0004	0.0008	0.0001	0.0017	0.0019	0.0019		
[65, 75]	0.0201	0.0007	0.0014	0.0001	0.0017	0.0022	0.0023		
[75, 100]	0.0175	0.0008	0.0009	0.0010	0.0010	0.0017	0.0019		
[100, 150]	0.0150	0.0010	0.0010	0.0001	0.0008	0.0013	0.0017		
[150, 300]	0.0106	0.0015	0.0009	0.0000	0.0011	0.0014	0.0021		

Table 5.5: Fake rates for $p_T \in [25 \text{ GeV}, 300 \text{ GeV}]$ and $1.15 \leq |\eta| < 1.37$, evaluated from the events selected using the overlap algorithm favoring electrons. The table reports the central value, the statistical, the systematic and the total uncertainty. For the systematic errors also the contribution from the different sources is listed: the uncertainty due to the variation of the invariant mass selection range (*Window*), the variation of the background subtraction procedure (*Background subtraction*), and the variation of the energy scale of the fake photon (*Scale*).

p_T [GeV]	$F_{e \rightarrow \gamma}$	Stat.	1.15 $\leq \eta < 1.37$				Total unc.
			Window	Background subtraction	Syst.	Scale	
[25, 35]	0.0279	0.0004	0.0006	0.0019	0.0027	0.0034	0.0034
[35, 45]	0.0271	0.0002	0.0004	0.0005	0.0003	0.0007	0.0007
[45, 55]	0.0250	0.0003	0.0006	0.0003	0.0027	0.0028	0.0028
[55, 65]	0.0262	0.0006	0.0010	0.0004	0.0027	0.0029	0.0030
[65, 75]	0.0221	0.0010	0.0008	0.0023	0.0017	0.0030	0.0031
[75, 100]	0.0244	0.0012	0.0014	0.0000	0.0014	0.0020	0.0023
[100, 150]	0.0178	0.0015	0.0012	0.0008	0.0007	0.0016	0.0022
[150, 300]	0.0168	0.0026	0.0010	0.0007	0.0010	0.0016	0.0030

Table 5.6: Fake rates for $p_T \in [25 \text{ GeV}, 300 \text{ GeV}]$ and $1.52 \leq |\eta| < 1.81$, evaluated from the events selected using the overlap algorithm favoring electrons. The table reports the central value, the statistical, the systematic and the total uncertainty. For the systematic errors also the contribution from the different sources is listed: the uncertainty due to the variation of the invariant mass selection range (*Window*), the variation of the background subtraction procedure (*Background subtraction*), and the variation of the energy scale of the fake photon (*Scale*).

p_T [GeV]	$F_{e \rightarrow \gamma}$	Stat.	1.52 $\leq \eta < 1.81$				Total unc.
			Window	Background subtraction	Syst.	Scale	
[25, 35]	0.0369	0.0004	0.0006	0.0028	0.0057	0.0063	0.0064
[35, 45]	0.0375	0.0003	0.0001	0.0009	0.0007	0.0011	0.0011
[45, 55]	0.0350	0.0004	0.0005	0.0001	0.0035	0.0036	0.0036
[55, 65]	0.0351	0.0007	0.0008	0.0005	0.0033	0.0034	0.0035
[65, 75]	0.0344	0.0012	0.0012	0.0002	0.0027	0.0029	0.0032
[75, 100]	0.0312	0.0013	0.0009	0.0007	0.0007	0.0013	0.0019
[100, 150]	0.0232	0.0017	0.0006	0.0000	0.0018	0.0019	0.0026
[150, 300]	0.0181	0.0027	0.0006	0.0068	0.0007	0.0069	0.0074

Table 5.7: Fake rates for $p_T \in [25 \text{ GeV}, 300 \text{ GeV}]$ and $1.81 \leq |\eta| < 2.01$, evaluated from the events selected using the overlap algorithm favoring electrons. The table reports the central value, the statistical, the systematic and the total uncertainty. For the systematic errors also the contribution from the different sources is listed: the uncertainty due to the variation of the invariant mass selection range (*Window*), the variation of the background subtraction procedure (*Background subtraction*), and the variation of the energy scale of the fake photon (*Scale*).

p_T [GeV]	$F_{e \rightarrow \gamma}$	Stat.	1.81 $\leq \eta < 2.01$				Total unc.
			Window	Background subtraction	Syst.	Scale	
[25, 35]	0.0397	0.0005	0.0003	0.0018	0.0031	0.0036	0.0037
[35, 45]	0.0409	0.0004	0.0003	0.0004	0.0004	0.0006	0.0007
[45, 55]	0.0392	0.0005	0.0006	0.0000	0.0043	0.0044	0.0044
[55, 65]	0.0398	0.0011	0.0008	0.0002	0.0035	0.0036	0.0037
[65, 75]	0.0369	0.0017	0.0007	0.0020	0.0041	0.0046	0.0049
[75, 100]	0.0359	0.0019	0.0006	0.0008	0.0034	0.0035	0.0040
[100, 150]	0.0308	0.0027	0.0005	0.0005	0.0027	0.0028	0.0039
[150, 300]	0.0225	0.0042	0.0010	0.0002	0.0002	0.0010	0.0043

Table 5.8: Fake rates for $p_T \in [25 \text{ GeV}, 300 \text{ GeV}]$ and $2.01 \leq |\eta| < 2.37$, evaluated from the events selected using the overlap algorithm favoring electrons. The table reports the central value, the statistical, the systematic and the total uncertainty. For the systematic errors also the contribution from the different sources is listed: the uncertainty due to the variation of the invariant mass selection range (*Window*), the variation of the background subtraction procedure (*Background subtraction*), and the variation of the energy scale of the fake photon (*Scale*).

p_T [GeV]	$F_{e \rightarrow \gamma}$	Stat.	2.01 $\leq \eta < 2.37$				Total unc.
			Window	Background subtraction	Syst.	Scale	
[25, 35]	0.0544	0.0005	0.0005	0.0011	0.0041	0.0043	0.0043
[35, 45]	0.0564	0.0003	0.0003	0.0001	0.0011	0.0011	0.0012
[45, 55]	0.0552	0.0005	0.0005	0.0004	0.0059	0.0059	0.0059
[55, 65]	0.0541	0.0010	0.0016	0.0006	0.0051	0.0054	0.0055
[65, 75]	0.0531	0.0017	0.0004	0.0019	0.0036	0.0041	0.0045
[75, 100]	0.0520	0.0019	0.0011	0.0012	0.0070	0.0071	0.0074
[100, 150]	0.0399	0.0027	0.0007	0.0001	0.0020	0.0021	0.0034
[150, 300]	0.0433	0.0055	0.0023	0.0012	0.0024	0.0035	0.0065

Table 5.9: Fake rates for $p_T \in [25 \text{ GeV}, 300 \text{ GeV}]$ and $0 \leq |\eta| < 0.8$, evaluated from the events selected using the overlap algorithm favoring photons. The table reports the central value, the statistical, the systematic and the total uncertainty. For the systematic errors also the contribution from the different sources is listed: the uncertainty due to the variation of the invariant mass selection range (*Window*), the variation of the background subtraction procedure (*Background subtraction*), and the variation of the energy scale of the fake photon (*Scale*).

p_T [GeV]	$F_{e \rightarrow \gamma}$	Stat.	0 $\leq \eta < 0.8$				Total unc.
			Window	Background subtraction	Syst.	Scale	
[25, 35]	0.0223	0.0001	0.0008	0.0017	0.0016	0.0025	0.0025
[35, 45]	0.0223	0.0001	0.0005	0.0005	0.0009	0.0011	0.0011
[45, 55]	0.0225	0.0001	0.0009	0.0000	0.0026	0.0028	0.0028
[55, 65]	0.0246	0.0003	0.0007	0.0010	0.0016	0.0020	0.0020
[65, 75]	0.0281	0.0005	0.0010	0.0002	0.0032	0.0033	0.0034
[75, 100]	0.0273	0.0006	0.0006	0.0028	0.0021	0.0035	0.0035
[100, 150]	0.0278	0.0009	0.0010	0.0003	0.0042	0.0043	0.0044
[150, 300]	0.0249	0.0015	0.0012	0.0016	0.0040	0.0045	0.0047

Table 5.10: Fake rates for $p_T \in [25 \text{ GeV}, 300 \text{ GeV}]$ and $0.8 \leq |\eta| < 1.15$, evaluated from the events selected using the overlap algorithm favoring photons. The table reports the central value, the statistical, the systematic and the total uncertainty. For the systematic errors also the contribution from the different sources is listed: the uncertainty due to the variation of the invariant mass selection range (*Window*), the variation of the background subtraction procedure (*Background subtraction*), and the variation of the energy scale of the fake photon (*Scale*).

p_T [GeV]	$F_{e \rightarrow \gamma}$	Stat.	0.8 $\leq \eta < 1.15$				Total unc.
			Window	Background subtraction	Syst.	Scale	
[25, 35]	0.0263	0.0003	0.0009	0.0017	0.0027	0.0033	0.0034
[35, 45]	0.0273	0.0002	0.0007	0.0000	0.0003	0.0007	0.0008
[45, 55]	0.0272	0.0002	0.0007	0.0003	0.0027	0.0028	0.0028
[55, 65]	0.0305	0.0005	0.0011	0.0002	0.0029	0.0031	0.0032
[65, 75]	0.0346	0.0009	0.0018	0.0004	0.0019	0.0027	0.0028
[75, 100]	0.0372	0.0011	0.0009	0.0009	0.0009	0.0016	0.0019
[100, 150]	0.0361	0.0017	0.0014	0.0007	0.0030	0.0034	0.0037
[150, 300]	0.0381	0.0030	0.0011	0.0002	0.0031	0.0033	0.0045

Table 5.11: Fake rates for $p_T \in [25 \text{ GeV}, 300 \text{ GeV}]$ and $1.15 \leq |\eta| < 1.37$, evaluated from the events selected using the overlap algorithm favoring photons. The table reports the central value, the statistical, the systematic and the total uncertainty. For the systematic errors also the contribution from the different sources is listed: the uncertainty due to the variation of the invariant mass selection range (*Window*), the variation of the background subtraction procedure (*Background subtraction*), and the variation of the energy scale of the fake photon (*Scale*).

p_T [GeV]	$F_{e \rightarrow \gamma}$	Stat.	1.15 $\leq \eta < 1.37$				Total unc.
			Window	Background subtraction	Syst.	Scale	
[25, 35]	0.0364	0.0004	0.0010	0.0018	0.0031	0.0037	0.0037
[35, 45]	0.0371	0.0003	0.0005	0.0003	0.0003	0.0007	0.0007
[45, 55]	0.0351	0.0004	0.0009	0.0002	0.0036	0.0037	0.0037
[55, 65]	0.0409	0.0008	0.0013	0.0005	0.0033	0.0036	0.0037
[65, 75]	0.0458	0.0015	0.0013	0.0002	0.0051	0.0053	0.0055
[75, 100]	0.0537	0.0019	0.0012	0.0002	0.0021	0.0024	0.0030
[100, 150]	0.0489	0.0026	0.0018	0.0001	0.0056	0.0059	0.0064
[150, 300]	0.0481	0.0046	0.0011	0.0026	0.0012	0.0031	0.0056

Table 5.12: Fake rates for $p_T \in [25 \text{ GeV}, 300 \text{ GeV}]$ and $1.52 \leq |\eta| < 1.81$, evaluated from the events selected using the overlap algorithm favoring photons. The table reports the central value, the statistical, the systematic and the total uncertainty. For the systematic errors also the contribution from the different sources is listed: the uncertainty due to the variation of the invariant mass selection range (*Window*), the variation of the background subtraction procedure (*Background subtraction*), and the variation of the energy scale of the fake photon (*Scale*).

p_T [GeV]	$F_{e \rightarrow \gamma}$	Stat.	1.52 $\leq \eta < 1.81$				Total unc.
			Window	Background subtraction	Syst.	Scale	
[25, 35]	0.0521	0.0005	0.0008	0.0005	0.0036	0.0037	0.0038
[35, 45]	0.0532	0.0003	0.0003	0.0003	0.0007	0.0008	0.0009
[45, 55]	0.0506	0.0004	0.0004	0.0007	0.0049	0.0050	0.0050
[55, 65]	0.0569	0.0010	0.0008	0.0004	0.0050	0.0051	0.0052
[65, 75]	0.0629	0.0017	0.0015	0.0005	0.0029	0.0033	0.0037
[75, 100]	0.0729	0.0022	0.0014	0.0012	0.0050	0.0053	0.0057
[100, 150]	0.0629	0.0031	0.0016	0.0011	0.0038	0.0043	0.0052
[150, 300]	0.0680	0.0056	0.0017	0.0092	0.0015	0.0095	0.0110

Table 5.13: Fake rates for $p_T \in [25 \text{ GeV}, 300 \text{ GeV}]$ and $1.81 \leq |\eta| < 2.01$, evaluated from the events selected using the overlap algorithm favoring photons. The table reports the central value, the statistical, the systematic and the total uncertainty. For the systematic errors also the contribution from the different sources is listed: the uncertainty due to the variation of the invariant mass selection range (*Window*), the variation of the background subtraction procedure (*Background subtraction*), and the variation of the energy scale of the fake photon (*Scale*).

p_T [GeV]	$F_{e \rightarrow \gamma}$	Stat.	1.81 $\leq \eta < 2.01$				Total unc.
			Window	Background subtraction	Syst.	Scale	
[25, 35]	0.0559	0.0006	0.0004	0.0018	0.0047	0.0051	0.0051
[35, 45]	0.0601	0.0004	0.0004	0.0000	0.0007	0.0008	0.0009
[45, 55]	0.0620	0.0006	0.0006	0.0004	0.0061	0.0061	0.0062
[55, 65]	0.0685	0.0014	0.0004	0.0019	0.0050	0.0054	0.0056
[65, 75]	0.0734	0.0025	0.0005	0.0015	0.0041	0.0044	0.0050
[75, 100]	0.0922	0.0033	0.0020	0.0010	0.0072	0.0076	0.0082
[100, 150]	0.0830	0.0048	0.0011	0.0015	0.0041	0.0045	0.0066
[150, 300]	0.0958	0.0096	0.0010	0.0008	0.0086	0.0087	0.0130

Table 5.14: Fake rates for $p_T \in [25 \text{ GeV}, 300 \text{ GeV}]$ and $2.01 \leq |\eta| < 2.37$, evaluated from the events selected using the overlap algorithm favoring photons. The table reports the central value, the statistical, the systematic and the total uncertainty. For the systematic errors also the contribution from the different sources is listed: the uncertainty due to the variation of the invariant mass selection range (*Window*), the variation of the background subtraction procedure (*Background subtraction*), and the variation of the energy scale of the fake photon (*Scale*).

p_T [GeV]	$F_{e \rightarrow \gamma}$	Stat.	2.01 $\leq \eta < 2.37$				Total unc.
			Window	Background subtraction	Syst.	Scale	
[25, 35]	0.0939	0.0006	0.0005	0.0015	0.0084	0.0085	0.0086
[35, 45]	0.1020	0.0005	0.0005	0.0005	0.0021	0.0022	0.0023
[45, 55]	0.1069	0.0007	0.0006	0.0011	0.0102	0.0103	0.0103
[55, 65]	0.1180	0.0016	0.0023	0.0004	0.0088	0.0091	0.0092
[65, 75]	0.1415	0.0030	0.0015	0.0009	0.0120	0.0122	0.0125
[75, 100]	0.1513	0.0037	0.0004	0.0047	0.0108	0.0118	0.0123
[100, 150]	0.1432	0.0058	0.0034	0.0019	0.0082	0.0091	0.0108
[150, 300]	0.1775	0.0128	0.0041	0.0013	0.0103	0.0112	0.0170

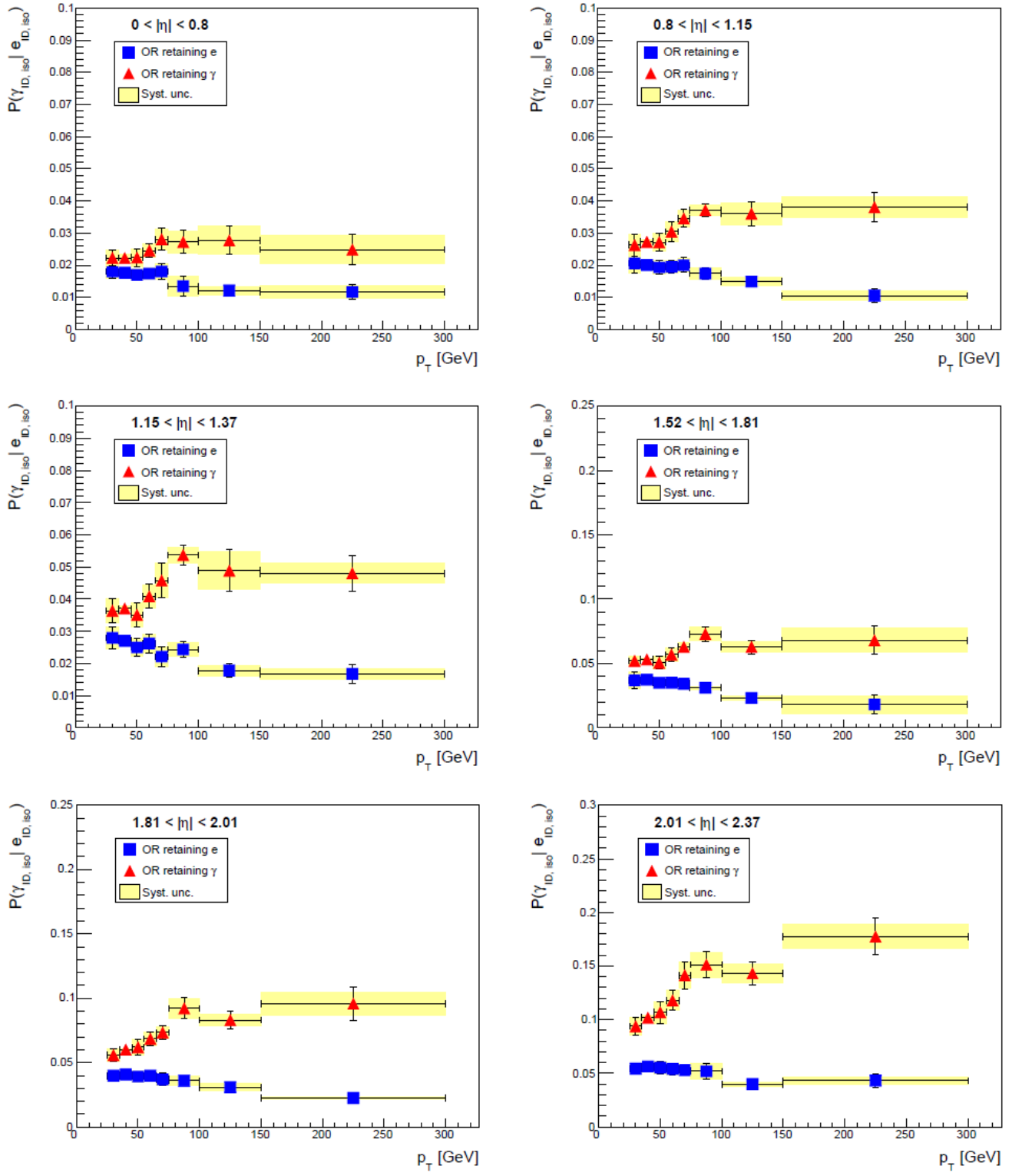


Figure 5.4: Fake rate measured as a function of p_T for electrons in the $|\eta|$ bins: $0 - 0.8$, and $0.8 - 1.15$, $1.15 - 1.37$, $1.52 - 1.81$, $1.81 - 2.01$, $2.01 - 2.37$. The results are reported for the overlap removal procedure retaining electrons (blue squares) and the overlap removal procedure retaining photons (red triangles). The error bars represent the total uncertainty, while the yellow bands represent the systematic uncertainty.

5.2 Background from electrons faking photons

After measuring the electron-to-photon fake rate, the number of electron fakes in each region of the analysis was estimated. An additional Control Region, called **Probe-electron Control Region**, is defined for each region of the analysis: the probe- e CR is built to be identical to the corresponding region of the analysis, except that the requirements for the leading photon are replaced with a request to have an electron. The electrons need to satisfy the same criteria requested for the selected electrons for the performed fake rate measurement (*probe electrons*): they need to meet the pre-selection classification of the Mono-Photon analysis (see Section 4.1.2); the transverse momentum is required to be larger than 25 GeV and $|\eta| < 1.37 \vee 1.52 < |\eta| < 2.37$; finally, they need to be isolated, i.e. electrons are required to be selected by the "loose" isolation working point and photons need to fit in the "FixedCutTight" isolation working point (see Section 5.1.1).

The event yield in each probe- e CR is then rescaled with the fake rate values, depending on $|\eta|$ and p_T of the selected probe electron. The result is the estimation of electrons faking photons in each region of the analysis.

The number of electron fakes was estimated using the electron-to-photon fake rate measurements described and provided in the previous Section (Tables from 5.3 to 5.8). The results for every region of the analysis for the three thresholds on E_T^{miss} (150 GeV, 225 GeV, and 300 GeV, see Chapter 4) are shown in Tables 5.15, 5.16, and 5.17. The nominal value of the background yields from electrons faking photons is reported, with its three-piece uncertainty. The first source of uncertainty for the number of electron fakes is the number of events selected in the probe- e CRs, while the second and the third are the statistic and systematic uncertainties related to the measurement of the electron-to-photon fake rate. The yields of electron fakes are consistently larger than the corresponding results obtained for the Mono-Photon analysis in 2016 [8]: however, the numbers are compatible within the error bars (see Fig. 5.5 and 5.6).

The total uncertainty on the electron fakes in every region lies between 10% and 20% of the nominal background yield. The major contribution to the total uncertainty in the three SRs is the systematic uncertainty related to the electron-to-photon fake rate. However, the contribution of the systematic uncertainty from the fake rate measurement is only slightly larger than its statistic counterpart.

Table 5.15: Number of electrons faking photons estimated in the SR and its CRs for the lower threshold of E_T^{miss} , i.e. $E_T^{\text{miss}} > 150$ GeV. The uncertainty is expressed in three terms: the first term is the statistical uncertainty related to the number of events found in the probe- e CR; the second and third terms are the statistical and systematic uncertainties related to the electron fake rate, respectively. The total uncertainty, calculated as the combination of the three uncertainties listed above, is also shown.

$E_T^{\text{miss}} > 150$ GeV					
	Electron fakes	Stat. for number of events in probe- e CR	Stat. for fake rate	Syst. for fake rate	Total unc.
SR	251	2.3	31.6	37.5	49.1
1 μ CR	21.1	0.6	2.6	3.2	4.2
2 μ CR	0.70	0.12	0.08	0.10	0.17
2 e CR	0.11	0.05	0.02	0.01	0.05
PhJet CR	93.0	1.4	11.7	13.9	18.2

Table 5.16: Number of electrons faking photons estimated in the SR and its CRs for the middle threshold of E_T^{miss} , i.e. $E_T^{miss} > 225$ GeV. The uncertainty is expressed in three terms: the first term is the statistical uncertainty related to the number of events found in the probe- e CR; the second and third terms are the statistical and systematic uncertainties related to the electron fake rate, respectively. The total uncertainty, calculated as the combination of the three uncertainties listed above, is also shown.

$E_T^{miss} > 225$ GeV					
	Electron fakes	Stat. for number of events in probe- e CR	Stat. for fake rate	Syst. for fake rate	Total unc.
SR	69.3	1.1	8.5	10.7	13.7
1 μ CR	5.95	0.33	0.71	0.92	1.21
2 μ CR	0.27	0.08	0.03	0.04	0.09
2 e CR	0.077	0.054	0.009	0.009	0.055
PhJet CR	93.0	1.4	11.7	13.9	18.2

Table 5.17: Number of electrons faking photons estimated in the SR and its CRs for the higher threshold of E_T^{miss} , i.e. $E_T^{miss} > 300$ GeV. The uncertainty is expressed in three terms: the first term is the statistical uncertainty related to the number of events found in the probe- e CR; the second and third terms are the statistical and systematic uncertainties related to the electron fake rate, respectively. The total uncertainty, calculated as the combination of the three uncertainties listed above, is also shown.

$E_T^{miss} > 300$ GeV					
	Electron fakes	Stat. for number of events in probe- e CR	Stat. for fake rate	Syst. for fake rate	Total unc.
SR	20.6	0.6	2.4	3.2	4.1
1 μ CR	1.58	0.16	0.18	0.26	0.35
2 μ CR	0.058	0.026	0.005	0.009	0.028
2 e CR	0.077	0.048	0.009	0.009	0.049
PhJet CR	93.0	1.4	11.7	13.9	18.2

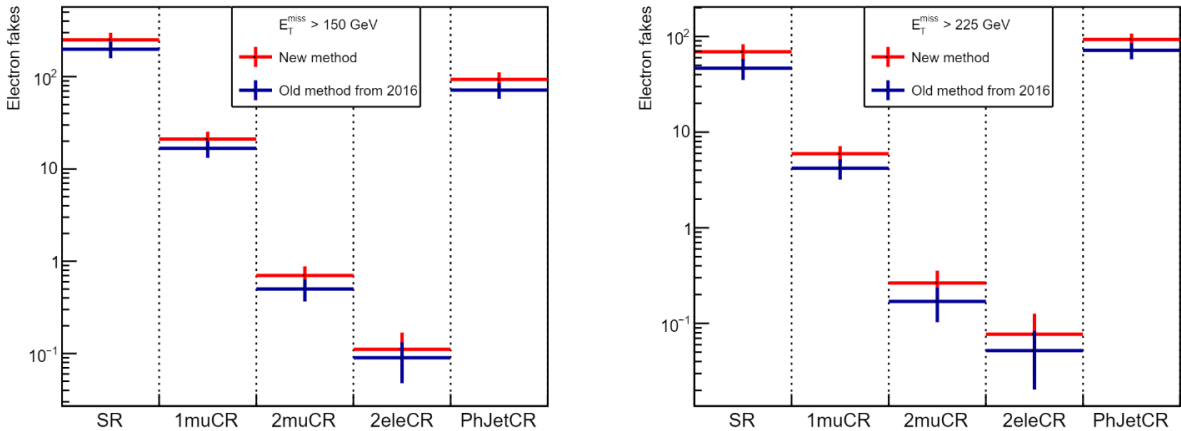


Figure 5.5: Background yields from electrons faking photons in the SR with the lower (left) and middle (right) thresholds on E_T^{miss} ($E_T^{miss} > 150$ GeV on the left and $E_T^{miss} > 225$ GeV) and its CR, as calculated in this thesis (red) and in the Mono-Photon analysis in 2016 (blue). The error bars represent the total errors on the electron fakes.

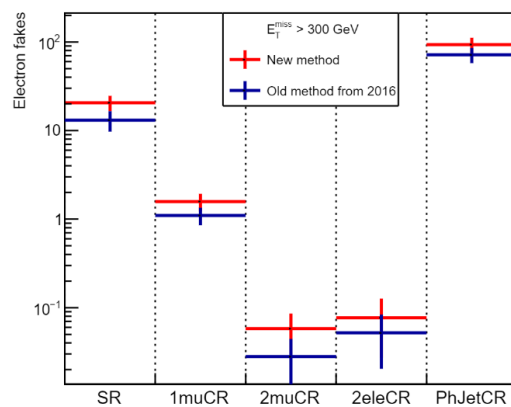


Figure 5.6: Background yields from electrons faking photons in the SR with the higher threshold on E_T^{miss} ($E_T^{miss} > 300$ GeV) and its CR, as calculated in this thesis (red) and in the Mono-Photon analysis in 2016 (blue). The error bars represent the total errors on the electron fakes.

CHAPTER 6

Conclusions

An estimation of the background yield from electrons faking photons for the Mono-Photon analysis was performed.

Evaluating the number of electron fakes in every region of the analysis required a measurement of the *electron-to-photon fake rate*, i.e. the probability that a prompt electron is reconstructed and identified as a photon.

The electron-to-photon fake rate was measured as a function of the pseudorapidity η in the range $(-2.37, 2.37)$ and as a function of p_T in different $|\eta|$ intervals $(0 - 0.8 - 1.15 - 1.37, 1.52 - 1.81 - 2.01 - 2.37)$, where the considered transverse momentum values were between 25 GeV and 300 GeV. The fake rate was determined from a $Z \rightarrow ee$ sample, where the final state can be reconstructed either as ee or $e\gamma$. The central value was obtained as a $e\gamma$ -to- ee ratio, where the yield of the reconstructed final states was extracted from Z boson mass spectra, after performing a background subtraction. The fake rate (as a function of η only) was found to increase with the absolute value of η : the lower values, found for η close to 0, are approximately 2%, reaching approximately 7.5% for $\eta \sim \pm 2.4$. On the other hand, the fake rate is approximately constant as a function of the transverse momentum for every $|\eta|$ interval, with a slight tendency to decrease with increasing p_T . Three main sources of systematic uncertainty on the measure of the electron-to-photon fake rate were identified, and their contribution to the total uncertainty was evaluated. The three identified sources were: the mass range used to select $e\gamma$ and ee yields from Z boson mass spectra; the background subtraction; the bias in the calibration of the energy of the fake photon in $e\gamma$ final states. The measured relative contributions were approximately 2 – 3%, 5 – 6%, and 1 – 2% (10%) for the measure of the electron-to-photon fake rate as a function of η ($|\eta|$ and p_T) respectively.

Finally, the electron-to-photon fake rate was used to compute the number of electron fakes for every region of the Mono-Photon analysis. The contribution from electrons faking photons for the Mono-Photon analysis is compatible (within the error bars) with the numbers obtained in the Mono-Photon analysis performed in 2016, despite it being consistently larger. The obtained number of electron fakes in the SR is 251 ± 49 , while the yield measured in 2016 was 199 ± 40 where 48 and 40 are the total uncertainties (statistic and systematic combined).

The new estimation of the contribution of the electron-to-photon fakes presented in this thesis exploits a more granular measurement of the fake rate and an improved background subtraction method. This ideally leads to a more precise estimation of the central value, even if the uncertainties are at the same level. For the new ongoing Mono-Photon analysis, data from 2017 and 2018 will be included, for a total integrated luminosity of $\sim 150 \text{ fb}^{-1}$. A larger integrated luminosity would reward the method employed in this thesis: the higher granularity would be useful to obtain a more reliable estimation of the electron-to-photon fakes, with a smaller statistic (and systematic) uncertainty.

Acknowledgments

I want to thank my supervisors, Leonardo Carminati, Stefano Manzoni, and Silvia Resconi: this thesis would not have even started without their help. Their door was always open for me, and I sincerely appreciate and value everything they taught me and every piece of advice they gave me during this work.

I would also like to thank my fellow students Luigi, Chiara, and Federica, for sharing with me both work and laughs: good luck with everything, ad maiora!

Bibliography

- [1] Jalal Abdallah et al. *Simplified models for Dark Matter searches at the LHC*. 2015. URL: <https://doi.org/10.1016/j.dark.2015.08.001>.
- [2] R. Bernabei et al. *The Dark Matter annual modulation results from DAMA/LIBRA*. 2014. DOI: 10.1051/epjconf/20147000043.
- [3] Gianfranco Bertone, Dan Hooper, and Joseph Silk. *Particle Dark Matter: Evidence, Candidates and Constraints*. 2004. URL: [arXiv:hep-ph/0404175](https://arxiv.org/abs/hep-ph/0404175).
- [4] Douglas Clowe, Marusa Bradac, Anthony H. Gonzalez, Maxim Markevitch, Scott W. Randall, Christine Jones, and Dennis Zaritsky. *A direct empirical proof of the existence of dark matter*. 2006. URL: [arXiv:astro-ph/0608407](https://arxiv.org/abs/astro-ph/0608407).
- [5] The ATLAS collaboration. *Electron efficiency measurements with the ATLAS detector using the 2015 LHC proton-proton collision data*. ATLAS, 2016. URL: <http://cds.cern.ch/record/2157687/files/ATLAS-CONF-2016-024.pdf?version=1>.
- [6] The ATLAS collaboration. *Measurement of the photon identification efficiencies with the ATLAS detector using LHC Run 2 data collected in 2015 and 2016*. ATLAS, 2018. URL: [arXiv:1810.05087](https://arxiv.org/abs/1810.05087).
- [7] The ATLAS collaboration. *Measurement of the photon identification efficiencies with the ATLAS detector using LHC Run-1 data*. ATLAS, 2016. URL: [arXiv:1606.01813v2](https://arxiv.org/abs/1606.01813v2).
- [8] The ATLAS collaboration. *Search for dark matter at $\sqrt{s} = 13$ TeV in final states containing an energetic photon and large missing transverse momentum with the ATLAS detector*. 2008. URL: [arXiv:1704.03848v2](https://arxiv.org/abs/1704.03848v2).
- [9] The ATLAS collaboration. *The ATLAS Experiment at the CERN Large Hadron Collider*. ATLAS, 2008. URL: [2008%20JINST%203%20S08003](https://cds.cern.ch/record/203%20S08003).
- [10] The ATLAS collaboration. *The ATLAS Inner Detector commissioning and calibration*. 2010. URL: [arXiv:1004.5293](https://arxiv.org/abs/1004.5293).
- [11] Glen Cowann, Kyle Cranmer, Eilam Gross, and Ofer Vitells. *Asymptotic formulae for likelihood-based tests of new physics*. 2013. URL: [arXiv:1007.1727v3](https://arxiv.org/abs/1007.1727v3).
- [12] Pieter van Dokkum et al. *A galaxy lacking dark matter*. 2018. URL: [arXiv:1803.10237](https://arxiv.org/abs/1803.10237).
- [13] Lyndon Evans and Philip Bryant. *LHC Machine*. JINST 3 (2008) S08001, 2008. URL: [10.1088/1748-0221/3/08/S08001](https://doi.org/10.1088/1748-0221/3/08/S08001).
- [14] Christian W. Fabjan and Fabiola Gianotti. *Calorimetry for Particle Physics*. 2003. URL: <https://doi.org/10.1103/RevModPhys.75.1243>.
- [15] W. Lampl, S. Laplace, D. Lelas, P. Loch, H. Ma, S. Menke, S. Rajagopalan, D. Rousseau, S. Snyder, and G. Unal. *Calorimeter Clustering Algorithms: Description and Performance*. 2008. URL: <http://cds.cern.ch/record/1099735/files/larg-pub-2008-002.pdf?version=1>.
- [16] Mariangela Lisanti. *Lectures on Dark Matter physics*. 2016. URL: [arXiv:1603.03797](https://arxiv.org/abs/1603.03797).
- [17] Stefano Manzoni. *Physics with photons with the ATLAS Run 2 data: calibration and identification, measurement of the Higgs boson mass and search for supersymmetry in di-photon final state*. Milano, 2017. URL: <https://cds.cern.ch/record/2303078/files/CERN-THESIS-2017-303.pdf>.

- [18] Mordehai Milgrom. *MOND theory*. 2014. URL: [arXiv:1404.7661](https://arxiv.org/abs/1404.7661).
- [19] Planck collaboration: P. A. R. Ade et al. *Planck 2013 results. I. Overview of products and scientific results*. 2014. URL: [arXiv:1303.5062](https://arxiv.org/abs/1303.5062).
- [20] Andreas Ringwald. *Exploring the role of axions and other WISPs in the dark universe*. 2012. URL: <https://doi.org/10.1016/j.dark.2012.10.008>.
- [21] Luminosity Public Results Run2. URL: https://twiki.cern.ch/twiki/bin/view/AtlasPublic/LuminosityPublicResultsRun2#Luminosity_summary_plots_for_AN3.
- [22] Trigger Operation Public Results Run2. URL: <https://twiki.cern.ch/twiki/bin/view/AtlasPublic/TriggerOperationPublicResults>.